https://lib.uliege.be https://matheo.uliege.be

Modelling PFAS leaching across the vadose zone under contrasting climatic conditions

Auteur : Wilmotte, Robin
Promoteur(s) : Brouyère, Serge
Faculté : Faculté des Sciences appliquées
Diplôme : Master en ingénieur civil des mines et géologue, à finalité spécialisée en géologie de l'ingénieur et de l'environnement
Année académique : 2024-2025
URI/URL : http://hdl.handle.net/2268.2/24550

Avertissement à l'attention des usagers :

Tous les documents placés en accès ouvert sur le site le site MatheO sont protégés par le droit d'auteur. Conformément aux principes énoncés par la "Budapest Open Access Initiative"(BOAI, 2002), l'utilisateur du site peut lire, télécharger, copier, transmettre, imprimer, chercher ou faire un lien vers le texte intégral de ces documents, les disséquer pour les indexer, s'en servir de données pour un logiciel, ou s'en servir à toute autre fin légale (ou prévue par la réglementation relative au droit d'auteur). Toute utilisation du document à des fins commerciales est strictement interdite.

Par ailleurs, l'utilisateur s'engage à respecter les droits moraux de l'auteur, principalement le droit à l'intégrité de l'oeuvre et le droit de paternité et ce dans toute utilisation que l'utilisateur entreprend. Ainsi, à titre d'exemple, lorsqu'il reproduira un document par extrait ou dans son intégralité, l'utilisateur citera de manière complète les sources telles que mentionnées ci-dessus. Toute utilisation non explicitement autorisée ci-avant (telle que par exemple, la modification du document ou son résumé) nécessite l'autorisation préalable et expresse des auteurs ou de leurs ayants droit.

UNIVERSITE DE LIEGE
FACULTE DES SCIENCES APPLIQUEES

Modelling PFAS leaching across the vadose zone under contrasting climatic conditions

---

WILMOTTE Robin

Thesis presented to obtain the degree of :
Master of Science in Geological and Mining Engineering
specialising in environmental and geological engineering

Thesis supervisor:		Other jury members:	
BROUYÈRE Serge	Liège University	COSME Frédéric	Geosyntec Consultants
		LAMBERT Stephanie	Liège University
		WALLIS Ilka	Flinders University

Academic year: **2024 - 2025**

Acknowledgments

I would like to express my sincere appreciation and thanks to Serge Brouyère for his support as my main supervisor. Thank you for your guidance, your patience, and for each piece of feedback you provided.

I would also like to thank Ilka Wallis, who welcomed me and especially helped me to familiarise myself with LEACHM, and patiently guided me through its use during and after my stay in Australia. Thank you also for your support at that time in organising my stay, and later, every time I reached out for help with this project.

Many thanks as well to Frédéric Cosme for welcoming me to his office at the Geosyntec office in Melbourne and for all the advice you shared, especially based on your own experiences with your final year project.

I have learned a great deal about PFAS, through my many discussions with each of you. The interest I have in this subject today stems from the experiences and conversations I have had thanks to our exchanges. It has been a pleasure working with you and undertaking this project, which would not have come to life without you.

This work would also not have been possible without the daily support of those around me. I would like to thank Hugh and Ruthie McEvoy for their interest in my project and, above all, for introducing me to their country during my internship in Australia, through which I was fortunate to build a wonderful friendship with them. I would also like to thank my fellow geology Master's students, without whom completing these years of engineering studies would very likely have been less enjoyable and more difficult. Finally, I am deeply grateful to my parents for their unwavering support throughout this project, and especially during the entirety of these years of study, marked by both highs and lows.

Summary

Concern over per- and polyfluoroalkyl substances (PFAS) has grown steadily as this large family of compounds has become better studied. While widely used for their unique physico-chemical properties, PFAS are now detected across the environment at a global scale. The most significant releases originate from firefighting foams applied on industrial and airport sites, leading to widespread soil and groundwater contamination. The vadose zone, located between the polluted surface and underlying groundwater, is the first zone affected and plays an important role in regulating PFAS migration. Its position makes it a particularly sensitive zone, where retention and transport processes directly determine the concentrations reaching aquifers.

The overall objective of this thesis is to gain a better understanding of the transport processes governing PFAS contamination in the vadose zone. Specifically, the extent to which retention in the vadose zone can significantly reduce the concentrations reaching groundwater is assessed. To achieve this, the work is primarily based on the study by Wallis et al. (2022), which highlights several factors influencing PFAS transport in the unsaturated zone under dry Australian climatic conditions. It was therefore decided to investigate whether these parameters remain equally important in a meteorological context representative of Belgium, i.e., a more temperate environment.

Results obtained under both Mediterranean (Australian) and temperate (Belgian) climatic conditions highlight that physical processes such as precipitation and evapotranspiration exert a strong control on PFAS migration through the vadose zone. In the Australian case, evapotranspiration contributes to retaining most of the PFAS mass within the first two metres of soil for decades, whereas under Belgian temperate conditions it plays a smaller, though still significant, role. At this silty-clayey site, the air-water interface has comparatively greater influence under Belgian conditions, whereas under Australian conditions evapotranspiration dominates PFAS retention. When evapotranspiration is excluded, however, the differences between the two climates largely disappear, confirming its central role. In both settings, PFAS retention occurs mainly in clay-rich horizons, likely due to the larger air-water interfacial area. Finally, interannual climatic variability significantly affects PFAS leaching, underscoring the need for representative climatic records when modelling PFAS transport from the source zone to groundwater.

Contents

1 Introduction **1**
1.1 Context . . . 1
1.2 Objectives of the Master's Thesis . . . 2
1.3 Structure of the Master's Thesis . . . 2

I State of the art: PFAS **3**

2 Introduction to PFAS **4**
2.1 Definitions and classification . . . 4
2.2 Sources, occurrence and regulations . . . 7

3 Physical and chemical properties of PFAS **10**
3.1 Physical state of PFAS . . . 10
3.2 Solubility and critical micelle concentration . . . 10
3.3 Surfactant properties of PFAS and partitioning to fluid-fluid interfaces . . . 11
3.4 Ionic states of PFAS . . . 12
3.5 Density . . . 14
3.6 Vapour pressures and volatility . . . 14
3.7 Henry's law constant K_h . . . 14
3.8 Octanol/water partition coefficient K_{ow} . . . 15
3.9 Organic carbon/water partition coefficient K_{oc} . . . 15
3.10 Persistence of PFAS . . . 15

4 PFAS behaviour in the subsurface **16**
4.1 Precursor transformation . . . 16
4.2 Partitioning at the solid-water interface . . . 19
4.3 Partitioning at the air-water interface . . . 24
4.4 Climate-driven physical flow processes . . . 28
4.5 Mobility and distribution of PFAS in the vadose zone . . . 29
4.6 Mobility and distribution of PFAS in the saturated zone . . . 30

II Modelling PFAS leaching under contrasting climatic conditions **31**

5 Modelling PFAS transport in the subsurface **33**
5.1 Introduction to LEACHM . . . 33
5.2 Water flow equations in unsaturated soil . . . 33
5.3 Solute transport equations . . . 34
5.4 Input parameters . . . 36
5.5 Model-specific limitations for PFAS applications . . . 37

6 Modelling of PFAS leaching under Mediterranean conditions 39
6.1 Conceptual model 39
6.2 Comparison with Wallis (2022) meteorological conditions 44
6.3 Comparison with Wallis (2022) PFAS leaching 48
6.4 Conclusion of the chapter 52

7 Study of PFAS leaching in temperate conditions 53
7.1 Climatic Adjustment for Belgian Conditions 53
7.2 Comparison between Australian and Belgian conditions 54
7.3 Evaluation of changes in PFAS leaching 58
7.4 Influence of evapotranspiration and AWI on PFAS transport 62
7.5 Conclusion of the chapter 68

III Conclusion and perspectives 69

8 Conclusion and perspectives 70
8.1 Conclusion 70
8.2 Perspectives 71

A History of PFAS 72
A.1 Evolution of PFAS Manufacturing Processes 72
A.2 Evolution of PFAS detection and scientific awareness 73

B Regulatory thresholds for PFAS in Belgium and Australia 75
B.1 Current PFAS thresholds in groundwater, soil and surface water in Wallonia, Belgium 75
B.2 Groundwater, soil and surface water current PFAS thresholds in Australia 77

C Water retention curve: Campbell, Hutson-Cass function 79

D RMI: Gridded observational data 81

E K_D dataset 82

Bibliography 84

List of Figures

2.1 PFAS family tree. Molecular structures of typical PFAS compounds (in red) are highlighted (Lyu et al., 2022). 5

2.2 Main sources of PFAS in commercial and industrial applications (Defence, 2019) 7

2.3 Release of firefighting foam (from J. Hale, Kleinfelder, cited and adapted by ITRC,2023). 8

3.1 Illustration of the formation of PFAS micelles, hemi-micelles, and bilayers. Also shown is an example of aggregation at a positively charged surface. Note that the opposite effect (electrostatic repulsion of PFAS) can occur if the surface is negatively charged (D. Adamson, GSI cited by ITRC, 2023). 11

3.2 Amphiphilic structures of PFOA and PFOS (We et al., 2023). 12

3.3 Chemical structures of PFAS compounds. Ionic states (Hatton et al., 2018). 13

4.1 PFAS-precursor transformation into PFCAs in shallow soil (Fabregat-Palau et al., 2025) 17

4.2 Illustration of precursor transformation resulting in the formation of PFAAs (ITRC,2023). 18

4.3 Schematic illustrating retention mechanisms of per- and polyfluoroalkyl substances (PFAS) to soils or sediments in which mineral phase and organic matter dominate. Perfluorooctanoic acid with the carboxylic functional group (-COO-) and perfluorooctanesulfonic acid with the sulfonate functional group (-SO3-) are shown as typical PFAS compounds (Lyu et al., 2022). 19

4.4 Organic carbon-normalised partitioning coefficients, $\log K_{OC}$ (mL/g $_{OC}$), for PFOS and PFOA across all soils (data from Campos-Pereira et al., 2022, cited by Campos-Pereira et al., 2023). 21

4.5 Box plots of logarithm (base 10) transformed Kd values for 29 PFAS in up to 10 soils as a function of perfluorinated carbon-chain length for PFCAs, PFSAs, FTSs, and FASAs (coloured), together with other PFAS and zwitterions (grey). Boxes show medians; whiskers show minima-maxima; $n = 3$ for C11 PFCA, $n = 2$ for 9Cl-PF$_3$ONS, $n = 9$ for zwitterions, and $n = 10$ for remaining compounds; n is the number of soils (Nguyen et al., 2020). 22

4.6 Effects of increasing metal-cation concentrations on distribution coefficients of anionic PFAS (Higgins & Luthy, 2006). 22

4.7 Relationship between peer-reviewed literature Kd values for PFOS and organic carbon (R2 =0.05, n=178) (Y. Li, Oliver, & Kookana, 2018). 23

4.8 (a) Sorption of PFAS at the air-water interface of bubbles(modified from We et al., 2023). 24

4.9 Impact of water saturation on PFOS retardation factors for solid-phase adsorption, air-water interface adsorption, and the sum of the two (total) Brusseau, 2018). 25

4.10 Relevant physical transport processes influencing the subsurface and surface such as the wind, solar radiation, rainfall events, evaporative water loss and exchange fluxes at interface between subsurface and surface (Jambhekar et al., 2015). 28

6.1 (a) Model Set-up; (b) Lithological profile of soil column from 0 to 7 m and organic matter content at field site based on analysis of drilling core. FIGURE modified after Selker and Or (2019). 40

6.2 Daily infiltrating rainfall [mm/d] and surface runoff [mm/d] for (A) the Wallis et al. (2022) model and (B) for the reproduced model 44

6.3 (A) Temperature [°C] from Wallis et al. (2022), used as a model input from the weather station located at the field site, and matric potential [kPa] at 50 mm depth as a model output. (B) Same parameters for the reproduced model, but with temperature measured at the RAAF Base Edinburgh in Adelaide. 45

6.4 (A) Groundwater recharge [mm/d] from Wallis et al. (2022), as a model output. The long-term average groundwater recharge is 9.8 mm/y, representing $\sim 5\%$ of the recorded rainfall during the simulation period, based on the weather data, soil characteristics, and plant cover. Recharge is slightly higher from 1970 to 1995, when fire-fighting training provided additional infiltration to the soil profile. (B) Reproduced model showing the same parameter, with a long-term average groundwater recharge of 46.08 mm/y, corresponding to $\sim 9\%$ of the recorded rainfall during the simulation period. 46

6.5 (Left) Profiles from Wallis et al. (2022): (1)soil lithology and organic-matter content, and (2) measured PFOS, PFHxS, and total PFAS [mg/kg], as well as simulated and calibrated total PFAS (blue bars) at 31/12/2019 [mg/kg]. For comparison, the theoretical distribution of a simulated tracer is also shown (grey bars). (Right) Simulated and calibrated total PFAS (blue bars) at 31/12/2019 [mg/kg] from the reproduced model. For comparison, the theoretical distribution of a simulated tracer is also shown (grey bars). 48

6.6 (A) From Wallis et al. (2022), porewater concentrations [mg/L] and mass [mg/m²] from 0 to 100 mm depth for a tracer (Koc = 0; light grey) and total PFAS. The latter is simulated with sorption (black line) and without sorption (grey line) to the air-water interface (AWI) to illustrate its effect. A selected PFAS depth profile for April 2003 (start of simulation period) is shown for the calibrated model (sediment and AWI sorption; black bars), for a model scenario with sediment sorption but without AWI retention (dark grey bars), for a tracer (light blue bars), and against a theoretical depth profile if evapotranspiration was not considered (sediment and AWI sorption; no ET; blue bars). (B) Reproduced model showing the same parameters. 49

6.7 (A) From Wallis et al. (2022), cumulative flux of PFAS mass moving beyond the shallow soil horizon (across 2 m depth) as a % of total applied PFAS. Model scenarios are compared to the mass over time of a tracer, moving at the rate of the infiltrating water (R = 1, light grey line). Time-integrated retardation coefficients are calculated on the basis of the differing mass between PFAS and tracer (R'= $\text{mass}_{\text{tracer}}/\text{mass}_{\text{PFAS}}$). These are plotted at the end of the 3M Light Water$^{\text{TM}}$ application period (1995) and 50 years thereafter (2045), together with the depth of the 50% tile of PFAS mass. (B) Reproduced model showing the same parameters. In this simulation, the model run time was extended to 100 years by duplicating the climatic record and applying it from 01/01/2024 to 31/12/2067. 50

7.1 Daily infiltrating rainfall and surface runoff [mm/d] in the reproduced model under Australian (A) and Belgian (B) weather conditions. The long-term average infiltrating rainfall is 415.0 mm/y in Australia and 780.2 mm/y in Belgium, with corresponding long-term average runoff values of 18.07 mm/y and 30.12 mm/y, respectively. 54

7.2 Temperatures used as model inputs from the weather stations located at RAAF Base Edinburgh in Adelaide (A) and at Bierset Airport in Liège (B). The matric potentials [kPa] are simulated for the top 50 mm of the soil profile, with average matric potential values of -376 kPa in Australia and -184 kPa in Belgium. 55

7.3 Groundwater recharge [mm/d] as model output from the reproduced simulation. The green curve represents the model run under Australian weather conditions, with a long-term average groundwater recharge of 46.08 mm/y, corresponding to only $\sim 9\%$ of the recorded rainfall during the simulation period. The blue curve corresponds to the simulation using Belgian weather data, with a long-term average of 264.93 mm/y, representing $\sim 30\%$ of the recorded rainfall. Recharge is fractionally higher from 1970 to 1995, when fire-fighting training provided additional infiltration to the soil profile. 56

7.4 Soil lithology and organic-matter content profiles from Wallis et al. (2022), shown alongside simulated **tracer** (chloride) porewater concentrations and mass distributions with depth at three times (1980, 2000, 2020) from the reproduced model under Australian and Belgian weather conditions. 58

7.5 Soil lithology and organic-matter content profiles from Wallis et al. (2022), shown alongside simulated **PFAS** porewater concentrations and cumulative mass distributions with depth at three times (1980, 2000, 2020) from the reproduced model under Australian and Belgian weather conditions. 59

7.6 Simulated chloride and PFAS leaching following the first AFFF release at the soil surface. For each case, the temporal evolution is shown for the cumulative mass in the top two metres and in the entire profile (7 m), together with PFAS porewater concentrations at the base of the profile. The total amount of PFAS and chloride injected at the soil surface by the end of 1995 is 24.960 g/m^2. Results are presented for (A) Australian and (B) Belgian weather conditions. In this simulation, the model run time is extended to 100 years by duplicating the climatic record and applying it from 01/01/2024 to 31/12/2067. 60

7.7 (A) Mass [mg/m²] from 0 to 100 mm depths for a tracer (Koc = 0; light grey) and total PFAS under Australian (A) and Belgian (B) weather conditions. The latter is simulated with sorption (black line) and without sorption (grey line) to the air-water-interface (AWI) to illustrate its effect. Periods of decreasing PFAS concentration and mass coincide with rain events and downward flux. Evapotranspiration allows for substantial periods of upward flow. 63

7.8 Simulated dissolved porewater concentrations of PFAS [mg/L] within the upper 100 mm of the soil profile under Australian (A) and Belgian (B) weather conditions. Concentrations are shown for the calibrated model (Koc = 90; AWI) (black line) as well as theoretical PFAS concentrations if air-water interface (AWI) sorption was negligible (grey line). For comparison, theoretical PFAS concentrations are also shown if evapotranspiration was negligible (light blue line). Rapid changes in concentration are caused by evapo-concentration during periods of ET > rain (summer), while dilution occurs during periods of rain > ET (winter). In this simulation, the model run time was extended to 100 years by duplicating the climatic record and applying it from 01/01/2024 to 31/12/2067. 64

7.9 Cumulative flux of PFAS mass moving beyond the shallow soil horizon (across 2 m depth) as a % of total applied PFAS. Model scenarios are compared to the mass over time of a tracer, moving at the rate of the infiltrating water (R = 1, light grey line). Time-integrated retardation coefficients are calculated on the basis of the differing mass between PFAS and tracer (R'= $\text{mass}_{\text{tracer}}/\text{mass}_{\text{PFAS}}$). Plotted at the end of the 3M Light Water$^{\text{TM}}$ thereafter (2045), together with the depth of the 50% tile of PFAS mass. The time-integrated retardation factors cannot be compared between the Australian (A) and Belgian conditions because the tracer reference curves differ between the 2 models. 65

7.10 Simulation with AFFF foams applied from 1970 to 1995; profiles shown 5-25 years after cessation. Under 'normal' conditions (black), Belgium shows deeper, more dispersed PFAS mass than Australia, where mass remains largely near-surface. The tracer (light blue) penetrates faster in Belgium, indicating higher water infiltration. Removing evapotranspiration (blue) produces much deeper migration, especially in Australia. Removing AWI (grey) increases mobility in both settings, with the greatest deepening in Belgium. 66

A.1 Emerging awareness and emphasis on PFAS occurrence in the environment (from J. Hale, Kleinfelder and modified from ITRC,2023). 73

D.1 Map showing the 5x5 km observational data grid of the RMI and the Bierset airport location. . . 81

E.1 Bibliography used to create the dataset 82

E.2 Dataset containing the K_D values of reference soils and soils treated using remediation techniques 83

List of Tables

2.1 List of 29 regulated PFAS in Wallonia (groundwater and surface water). 6
2.2 Short-chain and long-chain PFCA and PFSA (ITRC, 2023). 6

6.1 Summary of the parameters used in the simulations. 42

A.1 Discovery and manufacturing history of select PFAS (ITRC, 2023). 72

B.1 PFAS soil threshold values for industrial use (Type V), from SPW ARNE (2025). 76
B.2 PFAS groundwater thresholds (VL_{nappe}) used for VL_N calculation in Wallonia (SPW ARNE, 2025). 77

Chapter 1

Introduction

1.1 Context

1.1.1 PFAS: major contaminants

Whether in Belgium, Australia, or many other parts of the world, the public is increasingly concerned about the issues posed by per- and polyfluoroalkyl substances (PFAS). Ubiquitous in both households and industry due to their unique physico-chemical properties and widespread use in everyday products, PFAS are now detected throughout the environment on a global scale.

Often referred to as eternal pollutants, PFAS are known for their extreme persistence, high mobility, and potential for bioaccumulation, which make them major environmental contaminants. A growing scientific interest has emerged over the last decades and has led to numerous studies highlighting their potentially harmful effects on both human health and the environment. Consequently, the topic has received sustained media attention, and multiple controversies have made headlines, often triggered by the detection of elevated PFAS concentrations in groundwater or drinking water sources.

Over the past decade, governments have increasingly recognised the need to phase out the most hazardous PFAS compounds and to establish appropriate regulatory limits. As a result, understanding the transport and fate of PFAS in the environment has become a critical research priority, essential for both effective PFAS monitoring and the design of remediation strategies.

1.1.2 Background of the study and internship activities

The beginning of this study took place during a nine-week internship in Australia. For eight weeks, I worked at Flinders University in Adelaide under the supervision of Dr. Ilka Wallis, where I also had the opportunity to collaborate with members of the National Centre for Groundwater Research and Training (NCGRT). The main objective of the internship at Flinders was to investigate how soil remediation techniques influence PFAS transport in the vadose zone. More specifically, the aim was to model, using LeachM, the impact of chemical stabilisation or solidification of a one-dimensional soil profile, and observe how PFAS leaching would respond under these modified conditions.

To achieve this, a literature-based dataset was developed to describe how soil parameters, particularly the distribution coefficient (K_D), are affected by various additives used in stabilisation and solidification techniques. These remediation methods aim to immobilise PFAS in the vadose zone by enhancing their sorption to the soil matrix.

I also travelled to Melbourne for one week to collaborate with Geosyntec Consultants, where I worked alongside Mr. Frédéric Cosme and his team. The focus of this collaboration was to analyse publicly available data from the Australian Department of Defence in order to investigate the PFAS transport parameters at the Swartz Barracks military site in Queensland. A total of 42 PFAS concentration profiles were extracted from environmental investigations and analysed in collaboration with Frédéric Cosme. The analysis included interpretation of the site's lithology, moisture content, and total organic carbon (TOC) to better understand PFAS distribution patterns and transport behaviour.

The findings and experience gained during this internship provided a solid foundation for this master's thesis. They contributed significantly to a broader understanding of PFAS contamination in both theoretical and applied contexts. These skills, from mastering LeachM to analysing data and assessing remediation strategies, have proven essential for the successful completion of this project.

1.2 Objectives of the Master's Thesis

The overall objective of this thesis is to gain a better understanding of the transport processes governing PFAS contamination in the vadose zone. Specifically, the extent to which retention in the vadose zone can significantly reduce the concentrations reaching groundwater is assessed. To achieve this, the work is primarily based on the study by Wallis et al. (2022), which highlights several factors influencing PFAS transport in the unsaturated zone under dry Australian climatic conditions. It was therefore decided to investigate whether these parameters remain equally important in a meteorological context representative of Belgium, i.e., a more temperate environment.

1.3 Structure of the Master's Thesis

To achieve the objectives outlined in the previous section, it is essential to define the structure and sequence of the work. This study is organised into two main parts:

1. A literature review on PFAS, beginning with general background information, followed by a presentation of their physico-chemical properties, their behaviour in the vadose zone (with a brief mention of the saturated zone), and finally, an overview of the current approaches to modelling PFAS transport in the subsurface.
2. The experimental section, where the model developed by Wallis et al. (2022) was reproduced using the information available in the article and implemented in the LeachM software. While some questions were addressed to the first author, Ilka Wallis, regarding the best choices for uncertain parameters, the original model and confidential site data were not accessible. Therefore, the model was calibrated to achieve the best possible match. Afterwards, PFAS leaching under wetter conditions was investigated by adapting the climatic inputs to those of Belgium.

Finally, a concluding section discusses the results obtained and presents hypothesis regarding PFAS transport, developed from the insights gained during this work and addressing initial gaps in understanding formulated at the beginning of the thesis.

Part I

State of the art: PFAS

Chapter 2

Introduction to PFAS

2.1 Definitions and classification

PFAS is the acronym for perfluoroalkyl and polyfluoroalkyl substances. The definition of PFAS continues to evolve to reflect the continued study of these compounds and takes different forms depending on the regulatory body, the operational criteria used, and the intended scope and application of the included list of chemicals. There is no universally accepted definition of PFAS (ITRC, 2023). Among these definitions, the general definition of Buck et al. (2011) is still considered exact (ITRC, 2023):

- PFAS are highly fluorinated aliphatic substances that contain 1 or more C atoms on which all the H substituents present in the non-fluorinated analogues from which they are notionally derived have been replaced by F atoms, in such a manner that they contain the perfluoroalkyl moiety C_nF_{2n+1}-R (Buck et al., 2011).

This definition has been complemented by some information since then.

- Glüge et al. (2020) considered the definition of PFAS to include: substances in which a perfluorocarbon chain is connected with functional groups on both ends; aromatic substances that have perfluoroalkyl moieties on the side chains; fluorinated cycloaliphatic substances.
- OECD (2021) added that PFAS contain a perfluoroalkyl moiety with three or more carbons or a perfluoroalkylether moiety with two or more carbons.
- OECD (2021) also included chemicals that contain the R-C_nF_{2n}-R moiety in addition to the C_nF_{2n+1}-R moiety.

Perfluoroalkyl substances are fully fluorinated, and polyfluoroalkyl substances are only partially fluorinated. These second types of substances have the potential to be transformed abiotically or biotically into perfluoroalkyl substances.

Per- and polyfluoroalkyl substances (PFAS) constitute a large family of anthropogenic chemicals that includes several thousands of compounds. The PFAS family tree can be divided into 2 major classes: nonpolymers and polymers. Each class contains many subclasses, groups, and subgroups. The nonpolymers class can be divided between 2 subclasses[1]: perfluoroalkyl acids (PFAAs) and PFAAs precursors. Indeed, all other PFAS groups are potential precursors of PFAAs, including polymeric PFAS (Lyu et al., 2022; ITRC, (2023)). It should be noted that the PFAS family tree shown in FIGURE 2.1 is incomplete, as numerous compound groups exist within the different subclasses. Only the most environmentally relevant PFAS are typically represented. For instance, the PFAA subclass includes perfluoroalkyl phosphonic acids (PFPAs), perfluoroalkyl phosphinic acids (PFPiAs),

---

[1] Another way to see the PFAS family tree, according to ITRC (2023), is to divide the nonpolymers class into per- and polyfluoroalkyl substances.

and perfluoroether carboxylic and sulfonic acids (PFECAs and PFESAs), as well as the more widely studied perfluoroalkyl carboxylic acids (PFCAs, e.g., PFHxA and PFOA) and perfluoroalkyl sulfonic acids (PFSAs, e.g., PFHxS and PFOS) (ITRC, 2023; Lyu et al., 2022).

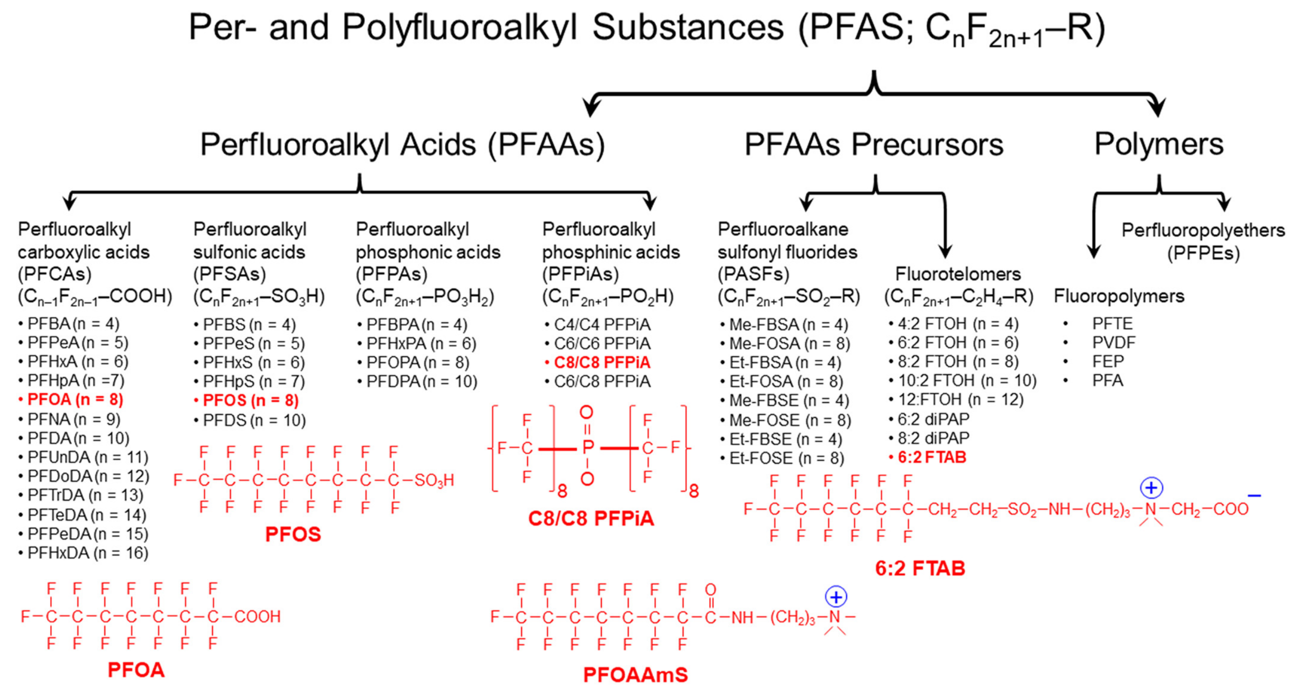

FIGURE 2.1: PFAS family tree. Molecular structures of typical PFAS compounds (in red) are highlighted (Lyu et al., 2022).

Considering the fluorotelomer-based substances, it should be noted that, in the "X:Y" designation, for example, 8:2 fluorotelomer alcohol (8:2 FTOH), X is the number of perfluorinated C atoms and Y is the number of non-fluorinated C atoms that originate from commercial synthesis (Buck et al., 2011).

Table 2.1 presents 29 PFAS of particular environmental concern that form the basis of current regulatory monitoring in Wallonia and are derived from EU requirements. As discussed in SECTION B.1, a subset is already covered by the European Union Drinking Water Directive (EU 2020/2184; “PFAS(20)”), while the remainder corresponds to the group envisaged for a forthcoming EU surface-water standard (“PFAS(24)”). Pending finalisation of that standard, Wallonia recommends analysing PFAS(24) (SPW ARNE, 2025).

As shown in the Table 2.1, PFAS are classified according to the CAS number (Chemical Abstracts Service number). It is a unique numerical identifier assigned to every distinct chemical substance by the Chemical Abstracts Service, a division of the American Chemical Society. This identifier is independent of naming conventions and is used internationally to ensure unambiguous reference to chemical substances across regulatory frameworks, databases, and scientific literature (Chemical Abstracts Service, n.d.). Each CAS number corresponds to a specific molecular structure, which includes its ionisation state or salt form when relevant.

TABLE 2.1: List of 29 regulated PFAS in Wallonia (groundwater and surface water).

Acronym	**Chemical formula**	**Name**	**CAS number**	**Family**	**Regulation**
TFA*	CF_3COOH	Trifluoroacetic acid	76-05-1	PFCA	–
PFBA	C_3F_7COOH	Perfluorobutanoic acid	375-22-4	PFCA	20 & 24
PFPeA	C_4F_9COOH	Perfluoropentanoic acid	2706-90-3	PFCA	20 & 24
PFHxA	$C_5F_{11}COOH$	Perfluorohexanoic acid	307-24-4	PFCA	20 & 24
PFHpA	$C_6F_{13}COOH$	Perfluoroheptanoic acid	375-85-9	PFCA	20 & 24
PFOA	$C_7F_{15}COOH$	Perfluorooctanoic acid	335-67-1	PFCA	20 & 24
PFNA	$C_8F_{17}COOH$	Perfluorononanoic acid	375-95-1	PFCA	20 & 24
PFDA	$C_9F_{19}COOH$	Perfluorodecanoic acid	335-76-2	PFCA	20 & 24
PFUnDA	$C_{10}F_{21}COOH$	Perfluoroundecanoic acid	2058-94-8	PFCA	20 & 24
PFDoDA	$C_{11}F_{23}COOH$	Perfluorododecanoic acid	307-55-1	PFCA	20 & 24
PFTrDA	$C_{12}F_{25}COOH$	Perfluorotridecanoic acid	72629-94-8	PFCA	20 & 24
PFTeDA	$C_{13}F_{27}COOH$	Perfluorotetradecanoic acid	376-06-7	PFCA	24
PFHxDA	$C_{15}F_{31}COOH$	Perfluorohexadecanoic acid	67905-19-5	PFCA	24
PFODA	$C_{17}F_{35}COOH$	Perfluorooctadecanoic acid	16517-11-6	PFCA	24
PFBS	$C_4F_9SO_3H$	Perfluorobutanesulfonic acid	375-73-5	PFSA	20 & 24
PFPeS	$C_5F_{11}SO_3H$	Perfluoropentanesulfonic acid	2706-91-4	PFSA	20 & 24
PFHxS	$C_6F_{13}SO_3H$	Perfluorohexanesulfonic acid	355-46-4	PFSA	20 & 24
PFHpS	$C_7F_{15}SO_3H$	Perfluoroheptanesulfonic acid	375-92-8	PFSA	20 & 24
PFOS	$C_8F_{17}SO_3H$	Perfluorooctanesulfonic acid	1763-23-1	PFSA	20 & 24
PFDS	$C_{10}F_{21}SO_3H$	Perfluorodecanesulfonic acid	335-77-3	PFSA	20 & 24
PFNS	$C_9F_{19}SO_3H$	Perfluorononanesulfonic acid	68259-12-1	PFSA	20
PFUnDS	$C_{11}F_{23}SO_3H$	Perfluoroundecanesulfonic acid	749786-16-1	PFSA	20
PFDoDS	$C_{12}F_{25}SO_3H$	Perfluorododecanesulfonic acid	79780-39-5	PFSA	20
PFTrDS	$C_{13}F_{27}SO_3H$	Perfluorotridecanesulfonic acid	791563-89-8	PFSA	20
HFPO-DA	$C_6HF_{11}O_3$	Hexafluoropropylene oxide dimer acid (GenX)	13252-13-6	PFECA	24
ADONA	$C_6HF_{11}O_2$	Ammonium 4,8-dioxa-3H-perfluorononanoate	958445-44-8	PFECA	24
C6O4	$C_6F_{10}O_4$	Difluoro(dioxo)perfluorohexane sulfonate	1190931-27-1	PFECA	24
6:2 FTOH	$C_6F_{13}CH_2CH_2OH$	6:2 Fluorotelomer alcohol	647-42-7	FTOH	24
8:2 FTOH	$C_8F_{17}CH_2CH_2OH$	8:2 Fluorotelomer alcohol	678-39-7	FTOH	24

Information in this table comes from the documents by SPW ARNE (2025) and European Parliament and Council (2020), as well as from the USEPA (2022) website.

* As no strict definition of PFAS exists, this compound is often grouped under the PFAS umbrella, although it does not meet the OECD (2021) definition (see SECTION 2.1), which requires at least a three-carbon perfluoroalkyl chain.

According to ITRC (2023), PFAA two main groups can be classified based on their carbon chain length, as shown in the TABLE 2.2. PFOS and PFOA are the 2 "long-chain" perfluoroalkyl acids most often reported and discussed in the scientific literature.

TABLE 2.2: Short-chain and long-chain PFCA and PFSA (ITRC, 2023).

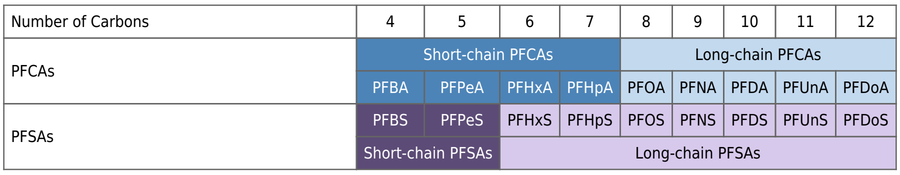

Number of Carbons	4	5	6	7	8	9	10	11	12
PFCAs	Short-chain PFCAs				Long-chain PFCAs				
	PFBA	PFPeA	PFHxA	PFHpA	PFOA	PFNA	PFDA	PFUnA	PFDoA
PFSAs	PFBS	PFPeS	PFHxS	PFHpS	PFOS	PFNS	PFDS	PFUnS	PFDoS
	Short-chain PFSAs		Long-chain PFSAs						

2.2 Sources, occurrence and regulations

2.2.1 Sources of PFAS in products and material

PFAS have been produced on a commercial scale since the 1950s, and production continues today. The number of PFAS and their uses have expanded over the years. The PFAS family has been estimated that may include more than 14,500 chemical substances (USEPA, 2022). A 2021 inventory of PFAS identified more than 4,700 PFAS with Chemical Abstracts Service (CAS) Registry Numbers that could have been, or may be, on the global market, although the uses of each of these PFAS may not be known (OECD, 2021).

The unique physical and chemical properties of PFAS confer oil, water, stain and soil repellency, chemical and temperature resistance, reduced friction, and surfactant behaviour to a wide range of products, some of which are considered essential to health, safety, and modern life (Glüge et al., 2020). Glüge et al. (2020) categorised PFAS by uses according to industry application and practical use and identified more than 200 uses for more than 1,400 individual PFAS.

Figure 2.2 presents a selection of consumer and industrial products identified as common PFAS sources (Defence, 2019; Glüge et al., 2020; ITRC, 2023). For example, among the 2,000 PFAS identified in a 2015 study, only about half had an associated listed use (KEMI, 2015 cited by ITRC, (2023)).

Figure 2.2: Main sources of PFAS in commercial and industrial applications (Defence, 2019)

2.2.2 Major sources of PFAS contamination

As a consequence of their diverse sources, PFAS have been detected across a wide array of environmental compartments and biological systems. They have been found in water, soil, sediments, and even in the blood of humans and animals, with increasing concentrations reported in wildlife such as invertebrates, fish, amphibians, reptiles, birds, and mammals (Lyu et al., 2022).

While PFAS may not be as acutely toxic as some pollutants, their extreme resistance to degradation, long-term environmental persistence, and high mobility raise serious concerns. Combined with decades of widespread use in industrial processes, firefighting foams, and consumer products, these properties have led to their trace-level presence in nearly all environmental media (ITRC, 2023).

However, certain PFAS releases have a greater potential for significant environmental impact, depending on the type and magnitude of the discharge, as well as the specific PFAS compounds and their concentrations. The following sources are sites where PFAS could be, or are known to have been, released to the environment, even if the site is not the location where PFAS were generated or used. In the absence of high-quality testing data, PFAS contamination may be assumed at these major sources (ITRC, 2023).

1. The most environmentally significant sources, particularly in terms of large-scale soil and groundwater contamination are the areas where aqueous film-forming foams (AFFF) are or were stored, used, or released (ITRC, 2023). AFFF are commonly used in firefighting training areas at airports, military bases, petrochemical sites, and fire stations (ITRC, 2023).

   Aqueous Film-Forming Foam (AFFF) is the most widely used type of Class B firefighting foam, designed to extinguish flammable liquid fires. Class B foams are generally divided into two main categories: fluorinated foams, which contain PFAS, and fluorine-free foams (F3), which do not. Other types of fluorinated foams also exist such as fluoroprotein foams (FP) and film-forming fluoroprotein foams (FFFP). Today, F3 foams are increasingly produced due to their PFAS-free composition (ITRC, 2023).

   Three types of AFFF exist: historical PFOS-based formulations, long-chain fluorotelomer-based foams, and more recent short-chain variants. Prior to the production phase-outs and regulatory changes of the 2000s and 2010s, the first two types were widely used (see Appendix A). Today, short-chain fluorotelomer-based formulations[2] are predominantly used in AFFF (ITRC, 2023; Rasmusson and Fagerlund, 2024).

   PFAS mixed with water are used in these foams (Figure 2.3) to reduce surface tension at phase boundaries and form an aqueous film that spreads across the surface of a hydrocarbon fuel. This enables to suppress fires by creating a vapour barrier that limits oxygen supply to the fuel (ITRC, 2023; Rasmusson and Fagerlund, 2024). Thanks to their surfactant properties, PFAS can effectively adsorb at air-water interfaces (e.g. air bubbles in water), facilitating foam formation (We et al., 2023). PFAS also exhibit high chemical stability, which makes them resistant to heat and chemical degradation. This stability is essential for maintaining their effectiveness under the extreme conditions of a fire (H. Li et al., 2023;ITRC, 2023; Rasmusson and Fagerlund, 2024).

   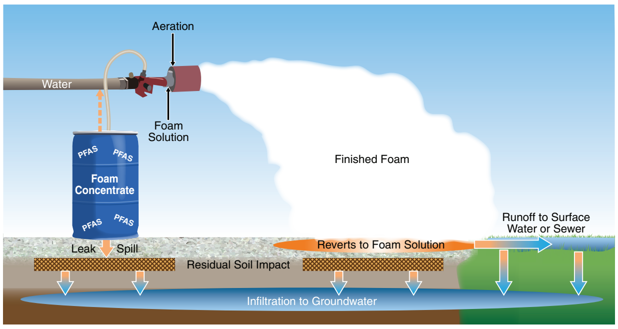

   Figure 2.3: Release of firefighting foam (from J. Hale, Kleinfelder, cited and adapted by ITRC,2023).

   A significant issue with this type of contamination is that records of AFFF application are often incomplete, making it difficult to quantify the source (ITRC, 2023).

2. In addition, industrial facilities that produce or process PFAS, or facilities that use PFAS chemicals or products in manufacturing or other activities may also represent a big source of PFAS contamination. Furthermore, these facilities may also contain areas where fire training or fire response using AFFF has occurred, AFFF storage areas, and AFFF fire suppression systems inside buildings (ITRC, 2023).

---

[2] Such as 6:2 fluorotelomer sulfonic acid (6:2 FTSA) (Rasmusson & Fagerlund, 2024).

3. Finally, waste management facilities (landfills) and wastewater treatment plants (WWTPs) represent a major source of PFAS in the environment, as they serve as the final destination and treatment point for PFAS-contaminated industrial waste and influent (ITRC, 2023).

   Moreover, biosolids are produced by separating liquids from solids in wastewater treatment systems, followed by further physico-chemical treatments to produce nutrient-rich materials. When applied to land or used in composting, these biosolids can therefore contain varying levels of PFAS (ITRC, 2023).

   It can be noted that the type and concentration of PFAS vary greatly among landfills and WWTPs, due to variations in the waste streams. As PFAS manufacturing processes change with time, the resulting type and composition of waste streams also change (ITRC, 2023).

Finally, another consideration regarding environmental impacts is the issue of anthropogenic ambient or anthropogenic "background" levels of PFAS. The long duration of PFAS use and their release from many types of sources may have resulted in low-level contamination of environmental media worldwide. The implications of ambient levels of PFAS should be considered in evaluating exposures and risk levels, establishing site action levels and cleanup goals, and identifying PFAS sources (ITRC, 2023).

2.2.3 Regulatory actions and industry phase-outs

Scientific, regulatory, and public concerns have emerged about the potential health and environmental impacts associated with the production, use, and disposal of PFAS-containing products and wastes. These concerns have led to efforts to reduce or replace certain PFAS, especially long-chain perfluoroalkyl carboxylates, long-chain perfluoroalkane sulfonates, and their precursors, including two of the most widely produced, commonly encountered, and extensively studied compounds: perfluorooctane sulfonic acid (PFOS) and perfluorooctanoic acid (PFOA) (ITRC, 2023).

APPENDIX A provides an overview of the industrial emergence of PFAS, including the introduction of the two main manufacturing processes and the progressive phase-out of selected long-chain substances. It also outlines the progression of scientific awareness and explains why compounds such as PFOA and PFOS have received significantly more attention than other PFAS.

APPENDIX B describes the regulatory thresholds currently in place in Wallonia (Belgium) and Australia for the protection of soil, surface water, and groundwater.

Chapter 3

Physical and chemical properties of PFAS

Currently, experimentally measured data for the different properties of PFAS are only available for a limited number of well-studied compounds. This restricted availability should be taken into account when relying on PFAS property data. For example, most values listed on the ITRC website are based on modelling approaches, and the input parameters used for these calculations may themselves be estimates. It is therefore important to assess the reliability of each value and understand how it was obtained before using it.

3.1 Physical state of PFAS

Most PFAS are solids at room temperature, commonly found in crystalline or powder form, but can be dissolved in water to a limited degree. However, several short-chain compounds, such as the acid forms of PFCAs and PFSAs with a 4- to 6-carbon perfluorinated tail, as well as fluorotelomer sulfonates (FTSs) and fluorotelomer alcohols (FTOHs), tend to be liquids under ambient conditions (ITRC, 2023; Lyu et al., 2022). Indeed, the available data from ITRC (2023) indicate that the melting and boiling points of PFAS tend to decrease as the length of the fluorinated chain decreases. For example, the melting point of PFBA ($C_n = 4$) is $-17.5°C$ while the melting point of PFTeDA ($C_n = 14$) is around $135°C$.

3.2 Solubility and critical micelle concentration

PFAS in general are considered moderately to highly soluble (Rasmusson and Fagerlund, 2024; HEPA, 2025; Y. Li et al., 2022). Appleman et al. (2014) emphasise that, unlike most other persistent and bioaccumulative contaminants (e.g. dioxins or polychlorinated biphenyls), PFAS are water-soluble.

However, the review conducted by Rasmusson and Fagerlund (2024) revealed a wide range of reported solubility values for individual PFAS. Indeed, the solubility of individual PFAS (especially the acid forms of PFAAs) may vary significantly depending on the method used for measurement, the form of the analyte (acid or salt), pH, salinity, the type of functional group, and whether the value is based on empirical data or modelling (ITRC,2023).

For example, according to Rasmusson and Fagerlund (2024) and Hellsing et al. (2016), when the functional group remains the same, PFAS exhibit decreasing solubility with increasing carbon-chain length. Furthermore, there are also differences in solubility between PFAS families. Perfluorocarboxylic acids (PFCAs), which contain a carboxyl group, generally have higher solubility than perfluorosulfonic acids (PFSAs) of comparable chain length (Ahrens et al., 2010).

In addition, some PFAS can form different types of supramolecular assemblies, such as micelles or hemimicelles. Given the contrasting behaviour of the hydrophilic head and hydrophobic tail, surfactants tend to aggregate into micelles (FIGURE 3.1) when their concentration in water exceeds a certain threshold. They can also form other supramolecular assemblies, such as hemi-micelles or mixed micelles (micelles composed of a mixture of surfactant-type molecules), either independently in solution or at boundaries occurring between phases. The microdispersions of these supramolecular assemblies may affect the reported water solubilities in addition to the truly solubilised molecules (ITRC, 2023).

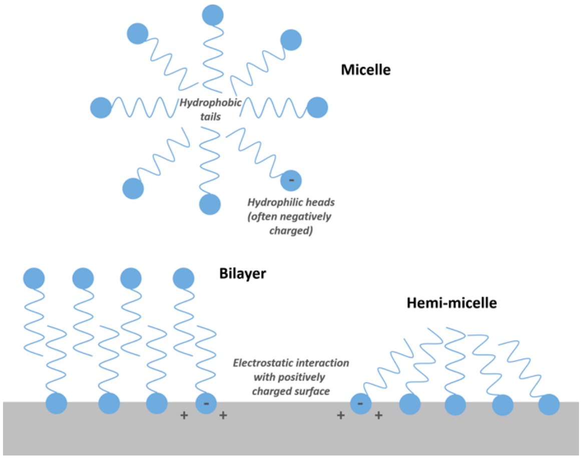

FIGURE 3.1: Illustration of the formation of PFAS micelles, hemi-micelles, and bilayers. Also shown is an example of aggregation at a positively charged surface. Note that the opposite effect (electrostatic repulsion of PFAS) can occur if the surface is negatively charged (D. Adamson, GSI cited by ITRC, 2023).

The theoretical threshold concentration at which surfactants begin to aggregate into micelles is referred to as the critical micelle concentration (CMC). The more hydrophobic PFAS have a lower CMC, which means that long-chain PFAS can form micelles or bilayer structures more easily than short-chain PFAS (H. Li et al., 2023). However, some reported behaviours of PFAS do not align with the conventional understanding of micelle formation. In particular, discrepancies have been observed between reported CMC values and known solubility limits, with some CMCs exceeding the solubility of the compound in question (López-Fontán et al., 2005; Yu et al., 2009; Sørli et al., 2020; Bhhatarai and Gramatica, 2011; all cited by ITRC, 2023).

However, according to Brusseau (2018), micelle formation in aqueous solution would not be a significant factor for subsurface conditions.

3.3 Surfactant properties of PFAS and partitioning to fluid-fluid interfaces

PFAS are characterised by their amphiphilic nature, combining a hydrophobic fluorinated tail with a hydrophilic functional group (FIGURE 3.2). They are therefore classified as fluorinated surfactants. These compounds are typically more surface-active than hydrocarbon surfactants with similar chain lengths (Brusseau, 2018; Lyu et al., 2022). This enhanced surface activity is related to the unique nature of the "tail" portion of the molecule. Like conventional hydrocarbon surfactants, the fluorinated tail is hydrophobic due to its nonpolar, fully saturated structure. However, unlike hydrocarbon tails, fluorinated tails are also lipophobic, due to the low polarisability of the carbon-fluorine bond (Brusseau, 2018; Lyu et al., 2022). This dual repellent property drives their accumulation at phase interfaces and surfaces (Brusseau, 2018; Guo et al., 2020; Hatton et al., 2018; Lyu et al., 2022), thus enabling them to significantly reduce the surface tension of liquids, as well as the interfacial tension between two liquids or between a liquid and a solid (Buck et al., 2011).

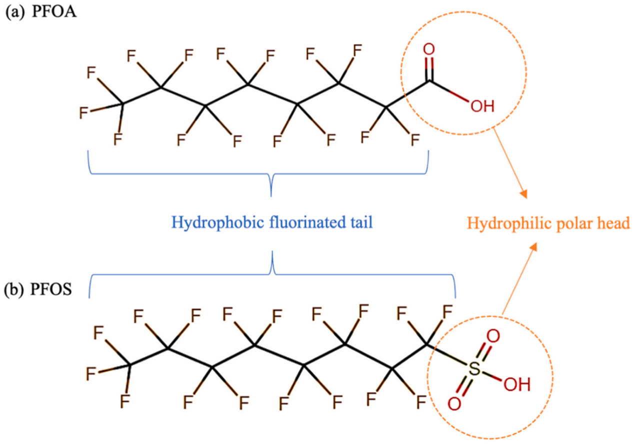

FIGURE 3.2: Amphiphilic structures of PFOA and PFOS (We et al., 2023).

The degree of affinity that perfluoroalkyl acids (PFAAs) exhibit for interfaces is related to the change in surface tension that occurs between the fluids when the compound is introduced to the system (ITRC, 2023). Generally, the surface tension and affinity for the interface decrease as the amount of PFAA increases in the system, although the relationship is not linear (ITRC, 2023; Brusseau and Van Glubt, 2019; Lyu et al., 2022). As described in SECTION 4, the tendency of PFAS to accumulate at interfaces, particularly at the air-water and solid-water interfaces, governs their transport in the subsurface and contributes to their complex behaviour.

A known effect associated with the presence of surfactants in the subsurface is the emergence of surfactant-driven flow. This refers to changes in capillary pressure head and in the soil water retention curve caused by surface-active compounds such as PFAS (Guo et al., 2020; Sauleda et al., 2022). As surfactants accumulate at the fluid-fluid or solid-fluid interfaces, they generate surface tension gradients that reduce the surface tension of water (Brusseau, 2018; Buck et al., 2011; Hatton et al., 2018). In the subsurface zone, surfactants can therefore alter the water flow, modifying its distribution and velocity. This can lead to enhanced spreading or the development of irregular wetting fronts (Sauleda et al., 2022). For example, a lower water content may be observed in areas with higher PFAS concentrations, possibly due to increased drainage induced by a stronger reduction in surface tension (Guo et al., 2020). These interactive processes result in a system where variably saturated flow, PFAS transport, and sorption are fully coupled (Guo et al., 2020). However, Guo et al. (2020) showed that PFOS-induced flow has a relatively minor effect on PFOS transport and migration, especially before reaching the groundwater. In addition, when PFOS reaches the more saturated zone near the groundwater table, its presence as a surfactant has a more noticeable, though still limited, influence on transport. Guo et al. (2020) also reported that surfactant-induced flow may have a greater impact in fine-textured porous media, where water saturation is higher.

3.4 Ionic states of PFAS

Chemical compounds within the PFAS family can exist in various ionic forms (FIGURE 3.3), which significantly influence their chemical and physical properties, including solubility, volatility, and bioaccumulation potential (ITRC, 2023). PFAS can be classified into four groups based on the ionic charge of their functional group:

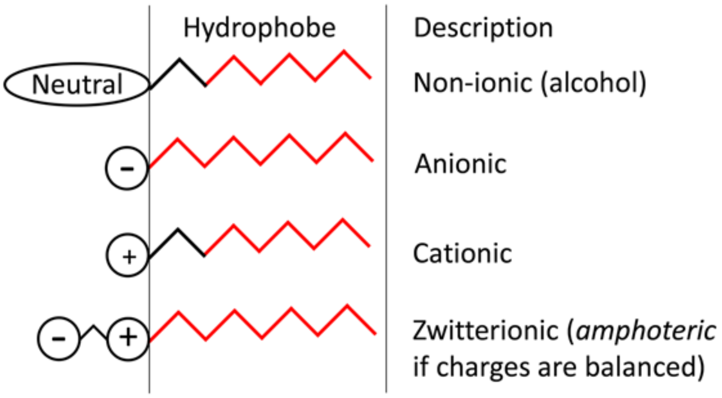

FIGURE 3.3: Chemical structures of PFAS compounds. Ionic states (Hatton et al., 2018).

According to Lyu et al. (2022), the ionic state of a PFAS depends on its pK_a and environmental pH conditions. Depending on their acid strength (pKa value), PFAS will dissociate to a greater or lesser extent to their corresponding anions in aqueous environmental media, soils, or sediments (Buck et al., 2011).

- When the pH is lower than the pK_a, the compound remains largely protonated, and may exist in a neutral (acidic) or cationic form depending on its functional groups.
- When the pH is higher than the pK_a, the compound tends to be deprotonated and typically exists in its anionic form.
- The functional group of zwitterionic PFAS has a molecular structure that carry both positive and negative charges simultaneously (Lyu et al., 2022). According to Lyu et al. (2022), zwitterionic PFAS compounds present characteristics that are highly influenced by ambient pH as they have different pKa values and thus multiple chemical speciation states (e.g., anionic, neutral, or cationic speciation).

Most perfluoroalkyl acids (PFAAs), such as PFOA and PFOS, are strong acids (Rasmusson and Fagerlund, 2024) and have very low pK_a values (typically below 1-3[1]). They are therefore present almost exclusively in their anionic form under environmental pH conditions (typical pH of 4-9) (H. Li et al., 2023). In contrast, some precursor PFAS may present different ionic forms (e.g., neutral, cationic, or zwitterionic) depending on the pH. (Buck et al., 2011; ITRC, 2023).

It is very important to distinguish between the acid form and the anionic form when reporting the physical and chemical properties. Inconsistent naming conventions in laboratory reports have led to confusion regarding exactly which form of PFAS the laboratories are measuring (ITRC, 2023). In the case of PFAAs, many available properties are based on their acid form, which is not present in the environment except at low pH (ITRC, 2023). Furthermore, some ionic states of PFAS are still being discovered. According to Lyu et al. (2022), numerous cationic and zwitterionic PFAS compounds have recently been identified.

To illustrate that differences in physicochemical properties between protonated and anionic forms, the perfluorooctanoate anion is highly water-soluble and has negligible vapour pressure, whereas perfluorooctanoic acid (PFOA) has very low water solubility and sufficient vapour pressure to partition from water into air (Buck et al., 2011). In addition, negatively charged PFAS are more mobile in soils than neutral and positively charged PFAS (Lyu et al., 2022).

---

[1] PFCAs pka < 1.6; PFSAs pka < 0.3 (H. Li et al., 2023); PFOA pKa = 2.8 (Lyu et al., 2022); PFOA, PFOS and PFBS pKa < 0.1 (Milinovic et al., 2015); PFOA pKa generally <3 and likely close to 0 (Brusseau, 2018);...

3.5 Density

It is possible that PFAS act as dense nonaqueous phase liquid (DNAPL), if the density of the liquid PFAS is greater than that of water (e.g. 4:2 FTOH) and if it is released into the environment as a pure product. However, if the PFAS is dissolved in water, the change in density of the solution relative to water is unlikely to result in a separate layer (ITRC, 2023).

In opposite, floating separate-phase liquid layers have been observed on the surface of aqueous PFOA and PFOS solutions at high concentrations. However, the formation of these layers appears to be driven by the tendency of PFAAs to accumulate and aggregate at air-water interfaces, and not by density (ITRC, 2023).

3.6 Vapour pressures and volatility

Vapour pressure is an indicator of a substance's tendency to partition into the gas phase and is therefore a direct measure of its volatility. In general, perfluoroalkyl acids (PFAAs), such as PFOA and PFOS, exhibit low vapour pressure (INERIS, 2024; ITRC, 2023). These substances are more likely to remain solid or liquid (ITRC, 2023).

However, several PFAS precursors, including fluorotelomer alcohols (FTOHs), fluorotelomer olefins as well as some perfluoroalkane sulfonamido derivatives[2], are known to be volatile (Brusseau, 2018; Buck et al., 2011). These substances have significantly higher vapour pressures than the stable end-products they can degrade into (ITRC, 2023; Buck et al., 2011).

3.7 Henry's law constant K_h

The Henry's law constant (K_h) quantifies the partitioning of a substance between the gaseous phase (air) and the aqueous phase (water) at equilibrium. Therefore, it provides an indication of the propensity of a chemical to remain dissolved in water rather than volatilising into the gas phase. K_H can be expressed as:

$$K_h^* = \frac{C_g}{C_{eq}} \; [-] \qquad K_h = \frac{P_v}{C_{eq}} \; [Pa \cdot m^3 \cdot mol^{-1}]$$

where C_g and C_{eq} are respectively the concentrations in the gaseous and aqueous phases, and P_v is the vapour pressure.

Considering the previous SECTION 3.6, the Henry's law constants, as define above, are therefore low for PFAAs[3]. This indicates that partitioning into the soil atmosphere in the vadose zone is unlikely to be a significant retention process for these compounds. In addition, the Henry's law constants for PFAS compounds such as FTOHs, fluorotelomer olefins and some perfluoroalkane sulfonamido derivatives are quite large[3]. According to Brusseau (2018), the atmospheric transport of the fluorotelomers has been identified as the probable cause of their observed widespread distributions in the environment.

K_h displays non-linear temperature dependence and is typically reported at $25°C$, which is higher than most ambient environmental conditions (Interstate Technology & Regulatory Council (ITRC), 2023).Furthermore, K_h values are generally determined for the protonated form of PFAAs. However, as discussed in SECTION 3.4, PFAS are more likely to exist in their anionic form under most environmental conditions. Their effective K_h values are therefore probably even lower (Brusseau, 2018). In addition, for PFAS that can dissociate into anionic or cationic forms, the Henry's law constants available in online datasets, such as that of ITRC (2023), may not be valid, as K_h is pH-dependent.

---

[2] FOSA, MeFOSA, EtFOSA, MeFOSE, and EtFOSE (Buck et al., 2011)

[3] K_h PFOA/PFOS $\approx 10^{-3}$ [-]; K_h FTOH $\approx$ 0.05-4 [-] and K_h fluorotelomer olefins $\approx$ 100-10,000 [-] (Brusseau, 2018)

3.8 Octanol/water partition coefficient K_{ow}

K_{ow} is defined as "the ratio of a chemical's concentration in the octanol phase to its concentration in the aqueous phase of a two-phase system" (USEPA, 2015). It is a useful descriptor of the tendency of a compound to associate with hydrophobic or hydrophilic substances. Direct measurement of the K_{ow} of PFAAs has proven difficult because they tend to aggregate at the interface between octanol and water (ITRC, 2023).

K_{ow} values are often used as surrogates for other properties, such as estimating K_{oc}, the soil organic carbon/water partition coefficient; bioaccumulation; uptake in biological systems; and ecotoxicity. However, in the case of PFAS, the use of their K_{ow} values as surrogates is generally not appropriate because PFAS do not behave like other well-researched nonionic polar chemicals (ITRC, 2023).

3.9 Organic carbon/water partition coefficient K_{oc}

K_{oc} is commonly used to quantify the potential of a given dissolved compound to associate with, or sorb to, organic matter occurring in soil. Although short- and long-chain PFAAs both exhibit high potential mobility in water, sorption on the solid matrix is still a significant retention factor in the subsurface (Dalahmeh et al., 2018; H. Li et al., 2023). Relative to commonly researched PFAS like PFOA and PFOS, several studies have suggested that K_{oc} can be appropriately defined as a distribution coefficient (K_d) normalized to organic carbon content, such as:

$$K_d = f_{OC} \cdot \frac{K_{oc}}{100}.$$

Where f_{OC} is the fraction of organic carbon [$\%$] and K_d is the distribution of a substance between the solid phase and water phase at equilibrium, normalized with the fraction of organic carbon in the soil (Campos-Pereira et al., 2023; Rasmusson and Fagerlund, 2024). This definition implies that K_{oc} specifically represents the singular process of hydrophobic interaction (Milinovic et al., 2015).

Numerous reviews highlight the complexity and variability of processes that may contribute to the sorption of PFAS and significant differences between laboratory and field-scale results (Y. Li, Oliver, and Kookana, 2018). Some of these reviews are used in the SECTION 4.2 to better understand these processes.

3.10 Persistence of PFAS

PFAS are synthetic compounds specifically designed for durability. Their chemical structure gives them exceptional resilience, particularly due to the carbon-fluorine bond (C-F), which is one of the strongest in chemistry. Consequently, unlike hydrocarbons or conventional pollutants that degrade over time, no natural chemical or biological degradation pathways are known to occur for PFAS under typical environmental conditions. Some may undergo transformation, but in general, PFAS remain intact (Lyu et al., 2022; ITRC, 2023; H. Li et al., 2023;Rasmusson and Fagerlund, 2024). This persistence has led to their common designation as "eternal chemicals" (Lyu et al., 2022). According to Buck et al. (2011), the chemical and thermal stability of the perfluoroalkyl moiety, combined with its hydrophobic and lipophobic character, results in highly useful and enduring properties in the surfactants and polymers into which it is incorporated.

PFCAs and PFSAs are known to be highly persistent substances (Buck et al., 2011). They are among the most thermally stable fluorinated surfactants. Although reports vary, it appears that temperatures exceeding $1,000°$C may be required to effectively destroy PFAS in soil (Colgan et al., 2018; Winchell et al., 2021; cited by ITRC, 2023).

Chapter 4

PFAS behaviour in the subsurface

Once released on the soil surface, PFAS may either run off or infiltrate into the soil. As they infiltrate, they migrate down through the vadose zone toward the saturated zone. Understanding PFAS transport through the subsurface is one of the main challenges in PFAS-related environmental risk assessment.

To date, there is no consensus in the literature regarding the main factors controlling PFAS transport in the subsurface (INERIS, 2024). However, four parameters appear to be particularly relevant to me, based on the experience I gained during my internship and the papers I reviewed::

1. Precursor transformation,
2. Partitioning at the air-water interface (AWI),
3. Partitioning at the solid-liquid interface,
4. climate-driven physical flow processes.

This chapter mainly focuses on PFAS transport in the vadose zone, as it is the central focus of this study. The final section, however, briefly addresses PFAS behaviour in the saturated zone in order to clarify the risks associated with these compounds.

4.1 Precursor transformation

Although PFAS are often referred to as "eternal pollutants", some of them can degrade and transform in the environment. As mentioned in SECTION 2.1, all non-PFAA PFAS are classified as potential perfluoroalkyl acid (PFAA) precursors. Lyu et al. (2022) explain this classification based on the chemical structure of polyfluoroalkyl substances.

PFAAs are fully fluorinated molecules with carbon-fluorine bonds throughout their carbon chain, making them highly resistant to degradation. They are therefore considered terminal degradation products under environmental conditions. In contrast, polyfluoroalkyl substances contain at least one carbon atom not fully fluorinated, allowing for degradation via the remaining carbon-hydrogen bonds. This partial fluorination enables their transformation into stable PFAAs (Lyu et al., 2022; INERIS, 2024; Fabregat-Palau et al., 2025).

Furthermore, fluorinated polymers, the second class of the PFAS family tree (FIGURE 2.1), according to Lyu et al. (2022), can also act as environmental sources of PFAS. Although they are not classified as direct PFAA precursors, they may release polyfluoroalkyl substances upon degradation, which can then transform into PFAAs (Buck et al., 2011; Lyu et al., 2022):

- In general, most fluoropolymer PFAS are likely to pose less environmental or health risk than non-polymer PFAS (ITRC, 2023). In fact, their degradation occurs over very long timescales (e.g., >1000 years), with only a small fraction ultimately converting to terminal perfluoroalkyl acids (PFAAs) (Buck et al., 2011; ITRC, 2023). For instance, PTFE did not exhibit significant transformation under specific incineration conditions (Aleksandrov et al., 2019, cited by ITRC, 2023).
- In contrast, according to Y. Li, Fletcher, et al. (2018), some polymers such as side-chain fluorinated polymers are less stable and are likely to break down into non-polymer PFAS over time. In particular, commercial side-chain fluorinated polymers have been shown to undergo biotransformation under environmental conditions (Washington et al., 2015, cited by ITRC, 2023) and abiotic degradation via hydrolysis during both environmental exposure and typical consumer use (Washington and Jenkins, 2015, cited by ITRC, 2023).

As a result, the PFAA precursors of interest are primarily composed of non-polymer polyfluorinated PFAS, which are more commonly detected in the environment. According to (Buck et al., 2011), the transformation PFAA precursors, larger functional and polymeric derivatives that contain a perfluoroalkyl moiety, occurs by abiotic or biotic degradation. According to Buck et al. (2011), the transformation of PFAA precursors, larger functional and polymeric derivatives containing a perfluoroalkyl moiety, occurs through abiotic or biotic degradation. For example, FIGURE 4.1 shows an 8:2 fluorotelomer phosphate diester (8:2 diPAP) being progressively transformed into PFHxA, a perfluoroalkyl carboxylic acid (PFCA) belonging to the broader PFAS family of perfluoroalkyl acids (PFAAs). This transformation occurs through a combination of microbial activity, enzymatic processes, and environmental factors such as soil composition, pH, moisture, temperature, and precursor bioavailability.

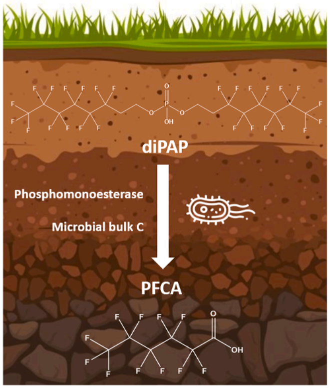

FIGURE 4.1: PFAS-precursor transformation into PFCAs in shallow soil (Fabregat-Palau et al., 2025)

In the vadose zone, PFAS precursor transformation is typically extremely slow and depends on environmental conditions such as redox potential and microbial activity (Fabregat-Palau et al., 2025; Hatton et al., 2018). In addition, these compounds often exhibit strong sorption to the soil matrix, further limiting their mobility. Hatton et al. (2018) says that "*Precursor compounds [...] presumably accumulate in the soil and aquifer matrix near the point of release, forming significant source zones.*" As a result, they can contribute to the long-term persistence of PFAS within the vadose zone (Brusseau, 2018; Hatton et al., 2018; Rasmusson & Fagerlund, 2024). Understanding the dynamics of precursor transformation is therefore essential, as it may explain the presence of persistent PFAS plumes near the surface that deviate from expected migration patterns. For example, when stable concentrations of terminal PFAS (such as PFOS and PFOA) are observed at the top of the unsaturated zone over extended periods, the presence of a slow-release secondary source can be suspected Fabregat-Palau et al., 2025. Such a source could be attributed to the gradual degradation of unstable precursor compounds, sustaining contamination decades after the initial release (Rasmusson and Fagerlund, 2024) (see FIGURE 4.2).

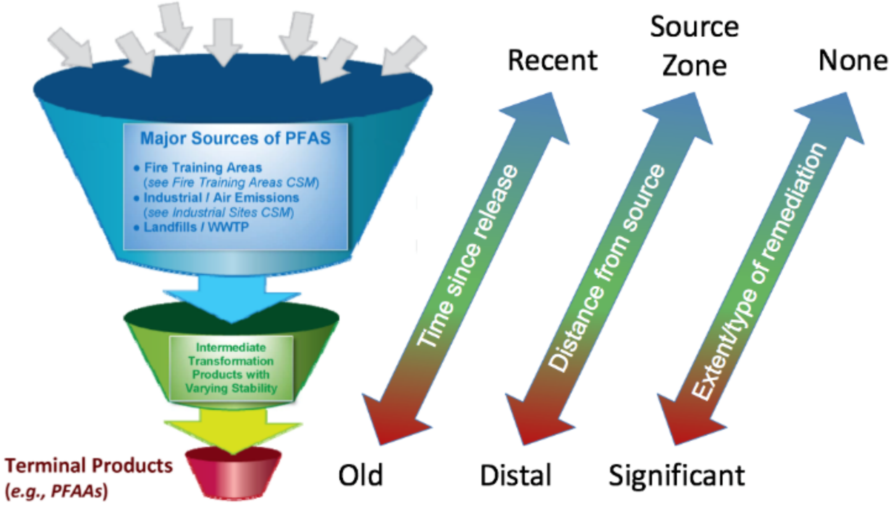

FIGURE 4.2: Illustration of precursor transformation resulting in the formation of PFAAs (ITRC,2023).

PFAAs precursors are commonly found in AFFF formulations and various industrial products Buck et al., 2011; Hatton et al., 2018. Given the existence of more than 12,000 PFAS-related substances (USEPA, 2022), and the fact that the detection of these compounds is often incomplete and difficult, even with recent improvements in analytical techniques such as high-resolution mass spectrometry, accurately tracing the origin of PFAS contamination remains particularly challenging (Fabregat-Palau et al., 2025; Lyu et al., 2022). For instance, PFOA may result from the biotransformation of 8:2 fluorotelomer alcohol (FTOH) (Buck et al., 2011), highlighting that PFOS, PFOA, and similar terminal compounds may arise not only from direct industrial discharge, but also from the degradation of precursors or impurities in consumer products.

Because of this analytical gap, precursors are often neglected in modelling efforts. However, this topic remains an active area of research. As transformation pathways and degradation rates become better understood, it may become possible to incorporate them into predictive models (Guo et al., 2020; INERIS, 2024).

The Total Oxidisable Precursor (TOP) assay is a method used for evaluating the presence of PFAS precursors in environmental samples. The technique works by breaking down PFAS precursors into perfluoroalkyl acids (PFAAs) through an oxidative process, thereby enabling their detection and quantification using standard analytical techniques. It provides an estimate of the total PFAS “reservoir”, that is, the quantity of precursors capable of being transformed into PFAAs. The method can also be used to investigate and better understand PFAS oxidative degradation pathways (Fabregat-Palau et al., 2025; Hatton et al., 2018).

In parallel, extractable organic fluorine (EOF) serves as an indirect indicator of the total amount of PFAS in a sample when non-PFAS fluorinated organic compounds are expected to be minimal. It enables the quantification of PFAS precursors that are unidentified or overlooked by conventional targeted analysis (Fabregat-Palau et al., 2025; We et al., 2023).

TOP assay results sometimes show no detectable transformation of PFAS precursors at certain sites, suggesting that the terminal PFAS concentrations observed are attributable solely to historical releases, typically from AFFF applications. This appears to be the case at the Swartz Barracks site in Queensland, where environmental investigations concluded that the majority of the PFAS contamination detected originated from direct AFFF discharges rather than ongoing precursor degradation (Defence, 2017).

4.2 Partitioning at the solid-water interface

4.2.1 PFAS sorption mechanisms at the solid-water interface

PFAS are found at the solid-water interface and interact with the solid phase of the soil through multiple sorption processes. As shown in FIGURE 4.3, PFAS sorption in the subsurface is governed by several mechanisms, including electrostatic and hydrophobic interactions, hydrogen bonding, and ligand exchange H. Li et al., 2023; Lyu et al., 2022.

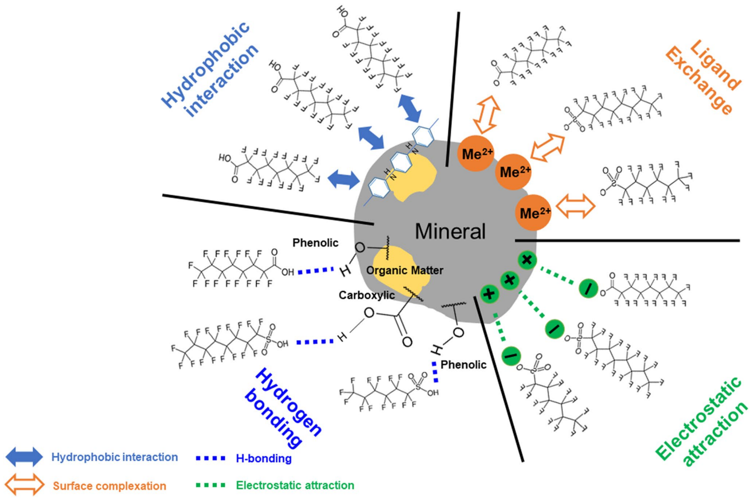

FIGURE 4.3: Schematic illustrating retention mechanisms of per- and polyfluoroalkyl substances (PFAS) to soils or sediments in which mineral phase and organic matter dominate. Perfluorooctanoic acid with the carboxylic functional group (-COO-) and perfluorooctanesulfonic acid with the sulfonate functional group (-SO3-) are shown as typical PFAS compounds (Lyu et al., 2022).

- **Electrostatic interaction** is often considered as one of the major dominant process influencing PFAS retention and transport. As the functional groups may carry positive, negative, or neutral charges, PFAS can have various type of electrostatic interaction with the solid matrix of the subsurface. Electrostatic effects tend to retard transport when attractive and to reduce retention when repulsive, thereby promoting mobility (H. Li et al., 2023; Lyu et al., 2022).
  - Direct interaction between charged grain surfaces and PFAS. Positively charged surfaces attract anionic PFAS and repel cationic species, while negatively charged surfaces exhibit the opposite behaviour (H. Li et al., 2023; Lyu et al., 2022).
  - Interaction between adsorbed substances on grain surfaces and PFAS molecules. Adsorbed substances can alter surface electrical property of the grain surfaces, and changed electrostatic interactions toward PFAS (H. Li et al., 2023; Lyu et al., 2022).
    - The sorption of humic acids or nano-TiO_2 carrying negative charges will likely initiate negative charges on the grain surface impart negative charges, enhancing repulsion of anionic PFAS and promoting their mobility (H. Li et al., 2023; Lyu et al., 2022).
    - Divalent cations such (e.g. Ca^{2+}, Mg^{2+}, Mn^{2+}) can neutralise surface charges, reducing electrostatic repulsion and increasing anionic PFAS sorption (Lyu et al., 2022).
    - PFAS already bound to surfaces may also hinder further sorption, facilitating the migration of excess PFAS. This is one of the reasons why increasing PFAS concentration in the soil induce more PFAS leaching (Lyu et al., 2022).
  - Cation bridging: divalent cations can bridge between negatively charged media and anionic PFAS, enhancing adsorption and retardation (H. Li et al., 2023).

  - Short-chain PFAS may engage more readily in electrostatic interactions than long-chain analogues due to their shorter molecular extension. On positively charged media, they can be strongly adsorbed, and sorption may induce surface aggregation (aggregates or hemi-micelles), which further enhances retention (H. Li et al., 2023).
  - Polar functionalities on the media (e.g. -NH, -OH) can participate in ion-dipole interactions with the carboxylic or sulfonic acid groups of PFAS (H. Li et al., 2023).

- **Hydrophobic attraction** occurs when both interacting surfaces are hydrophobic, linking PFAS to hydrophobic substances in the subsurface, such as organic carbon and organic contaminants (e.g., chlorinated solvents) (H. Li et al., 2023; Lyu et al., 2022; Nguyen et al., 2020).
  - The sorption of PFAS on grain surfaces generally increases with hydrophobicity. Accordingly, retention and retardation increase with chain length, consistent with hydrophobicity being a significant driving force for sorption and transport.
  - However, for short-chain PFAAs and certain emerging or less-characterised PFAS (e.g., cationic or zwitterionic species), hydrophobicity alone is not a reliable predictor of sorption behaviour in soils.

  As mentioned in the previous section, the air-water interface (AWI) is strongly hydrophobic, which explains why certain PFAS are strongly retained by forming films (H. Li et al., 2023; Lyu et al., 2022; Nguyen et al., 2020).

- **Hydrogen bonding** is an electrostatic interaction between a hydrogen atom covalently bound to an electronegative atom and another electronegative atom carrying a lone electron pair. The hydrophilic oxygen-bearing functional groups of PFAS (e.g., -OH, -COOH, sulfonates) can form hydrogen bonds with oxygen-bearing groups on adsorbent surfaces.
  - Sulfonic group of PFOS can form such bonds with various metal oxide nanoparticles[1], and water molecules can compete with PFOS for these binding sites (Lyu et al., 2022).
  - Hydrogen bonds may also form at water-oxide interfaces (e.g. aluminium and iron oxides), further stabilising interfacial association. (H. Li et al., 2023).
  - Amino functionalities on the media can engage in H-bonding with PFCA carboxyl groups, providing additional binding motifs. (H. Li et al., 2023).
  - Hydrophobic C-F tail of PFAS limits hydrogen bond formation with oxygen atoms on mineral surfaces (Lyu et al., 2022).
  - Soils with greater anion-exchange capacity retain more short-chain PFCAs (PFBA, PFPeA, PFHxA, PFHpA) due to hydrogen bonding (H. Li et al., 2023)

- **Ligand exchange** is a surface reaction in which a pre-existing ligand (typically hydroxyl or water) is replaced by the hydrophilic head group of a PFAS, forming inner-sphere complexes (H. Li et al., 2023; Lyu et al., 2022).
  - Ligand-exchangeable metallic minerals (e.g. iron and aluminium oxides) present abundant surface hydroxyls that can be substituted by PFAS head groups, yielding inner-sphere complexes (H. Li et al., 2023).
  - PFOA can form Fe-carboxylate inner-sphere complexes on iron oxides via ligand exchange (H. Li et al., 2023; Lyu et al., 2022). By contrast, PFOS adsorption on hematite occurs mainly via hydrogen bonding and electrostatic interactions, forming outer-sphere complexes (Lyu et al., 2022).
  - In metallic mineral-rich media, ligand exchange and related surface complexation strengthen retention and reduce PFAS mobility (H. Li et al., 2023).

---

[1] Al_2O_3, Fe_2O_3, SiO_2, and TiO_2

4.2.2 Influence of the soil and wtaer properties and PFAS characteristics

The intensity of the sorption mechanisms depends on the properties of the soil and the porewater in the subsurface, as well as on the specific physicochemical characteristics of the PFAS.

- **Organic matter**
  Organic matter (OM) generally enhances the retention of long-chain PFAS, while shorter-chain PFAS remain more mobile and pose a higher transport risk (H. Li et al., 2023). Long-chain PFAS tend to remain in the condensed zones of the humin fraction, whereas short-chain species preferentially adsorb on humic and fulvic acids, likely due to differences in head-group charge. Negatively charged OM may also promote electrostatic repulsion when coating mineral surfaces, and even low OM contents can compete for sorption sites, with a stronger effect observed for short-chain PFAS (H. Li et al., 2023).

- **pH**
  For PFAAs and other low-pK_a PFAS, pH has little effect on PFAS speciation. The dominant effect is via sorbent charge: decreasing pH makes sorbent surfaces more positively charged and generally increases sorption of anionic PFAS, whereas increasing pH renders surfaces more negative and reduces sorption (Higgins & Luthy, 2006; Nguyen et al., 2020). This pH-dependent variation in sorption is illustrated for PFOS and PFOA, two representative PFAAs, in FIGURE 4.4. As highlighted in SECTION 3.9, the organic carbon-water partition coefficient (K_{OC}) provides a useful descriptor of PFAS sorption onto the solid matrix. Furthermore, Hydrogen bonding is also pH dependent: at higher pH, surface hydroxyls can form H-bonds with anionic PFAS head groups, influencing interfacial association (H. Li et al., 2023). In addition, for PFAS with titratable functional groups within the environmental pH range (e.g., FOSA), changes in protonation state can significantly influence their binding, leaching, and overall fate (Campos-Pereira et al., 2023). According to Campos-Pereira et al. (2023), the sorption of long-chain PFAS has a stronger pH dependence.

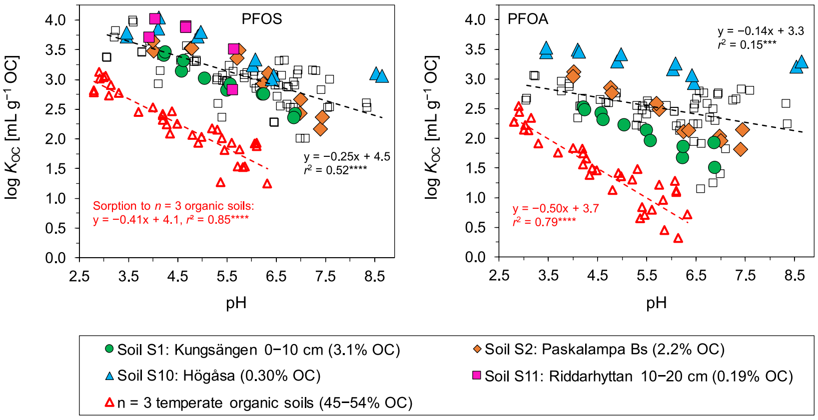

FIGURE 4.4: Organic carbon-normalised partitioning coefficients, log K_{OC} (mL/g$_{OC}$), for PFOS and PFOA across all soils (data from Campos-Pereira et al., 2022, cited by Campos-Pereira et al., 2023).

- **Organic immiscible liquid (OIL) co-contamination**
  At some sites, OIL (e.g. LNAPL/DNAPL) alters PFAS retention by modifying solid-phase adsorption and providing OIL-water interfacial area where PFAS accumulate owing to their amphiphilicity. The net effect is typically enhanced retention and reduced mobility, contingent on OIL saturation, composition, and interfacial area (Brusseau, 2018, 2020; Brusseau & Van Glubt, 2019). It is important to note that if PFAS contamination from AFFF use is found on-site, OIL was likely released previously, and residuals may still influence PFAS retention near the surface.

- **Molecular structure (chain length and head group)**
  Sorption generally increases with perfluorocarbon chain length (FIGURE 4.5): long-chain PFAAs sorb more strongly and partition to sediments more than short-chain analogues, although both remain mobile in water (Dalahmeh et al., 2018). This trend points to hydrophobic partitioning to soil organic matter as a principal driver (Nguyen et al., 2020), with additional contributions from stronger binding of long-chain PFAS to Fe/Al (hydr)oxides via electrostatic interactions (Campos-Pereira et al., 2023).

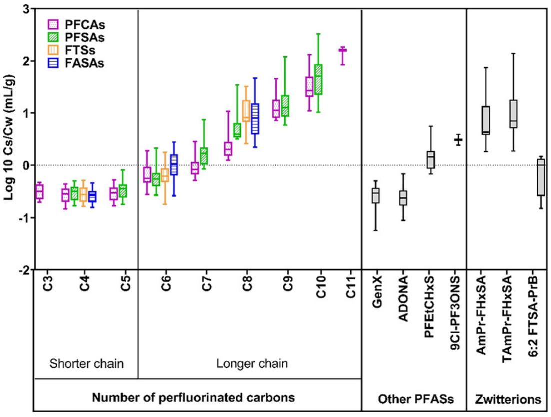

FIGURE 4.5: Box plots of logarithm (base 10) transformed Kd values for 29 PFAS in up to 10 soils as a function of perfluorinated carbon-chain length for PFCAs, PFSAs, FTSs, and FASAs (coloured), together with other PFAS and zwitterions (grey). Boxes show medians; whiskers show minima-maxima; $n = 3$ for C11 PFCA, $n = 2$ for 9Cl-PF$_3$ONS, $n = 9$ for zwitterions, and $n = 10$ for remaining compounds; n is the number of soils (Nguyen et al., 2020).

- **Metal cations and mineral surfaces**
  Mineral (hydr)oxides (Fe/Al) enhance PFAS sorption via inner-/ outer-sphere complexation and ligand exchange. For example, higher oxide contents increase PFOS/PFOA retention (INERIS, 2024). Cations (Na^+, K^+, Mg^{2+}, Ca^{2+}) modulate electrostatics and ionic strength: as shown in FIGURE 4.6, increasing cation concentration generally increases adsorption of anionic PFAS on negatively charged surfaces but can decrease it on positively charged surfaces (Lyu et al., 2022).

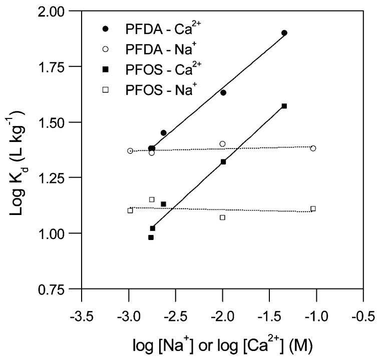

FIGURE 4.6: Effects of increasing metal-cation concentrations on distribution coefficients of anionic PFAS (Higgins & Luthy, 2006).

There actually is no consensus on the dominant soil properties controlling sorption (Lyu et al., 2022; Campos-Pereira et al., 2023; INERIS, 2024).

4.2.3 Solid-water distribution coefficient (K_d)

The sorption process is commonly characterised by the solid-water distribution coefficient (K_d), which reflects the affinity of PFAS for the solid phase. A higher K_d value indicates a greater extent of sorption to the solid phase. As described in SECTION 3.9, K_d is often estimated from the organic carbon-water partition coefficient (K_{OC}) and the fraction of organic carbon (f_{OC}).

A second way to define it, is as the ratio between the mass of PFAS adsorbed per unit mass of solid and the equilibrium concentration in the aqueous phase (Milinovic et al., 2015):

$$K_d = \frac{C_s}{C_{eq}} \quad [L/kg]$$

where C_s is the PFAS concentration sorbed onto the soil (ng·kg^{-1}), and C_{eq} is the PFAS concentration in the water at equilibrium (ng·L^{-1}).

Therefore, K_d is used for linear sorption, meaning the sorbed concentration (C_S) is directly proportional to the dissolved concentration (C_{eq}). However, this is not fully representative of real conditions, where non-linear sorption can occur. In such situations, using the Freundlich isotherm constant, K_f, provides a more realistic representation of sorption behaviour. At equilibrium, the mathematical formulation of the Freundlich isotherm, as described in Guo et al. (2020) and Milinovic et al. (2015), is as follows:

$$K_f = \frac{C_s}{C_{eq}^N} \quad [^*]$$

where N is a dimensionless exponent controlling non-linearity. Hence, for $0 < N < 1$, K_f decreases with increasing C_{eq} (diminishing sorption strength); for $N > 1$, K_f increases with C_{eq} (increasing sorption strength). When $N \approx 1$, the Freundlich model reduces to a linear isotherm and $K_f \approx K_d$.
* The units of K_f depend on N.

Furthermore, according to Brusseau (2020) and Y. Li, Oliver, and Kookana (2018), the relationship between K_{OC} and f_{OC} is often non-linear, as K_{OC} is not a universal constant for a given PFAS (Figure 4.7). Indeed, the formula $K_d = f_{\text{OC}} K_{\text{OC}}$ is based on the simplified assumption that sorption is mainly governed by hydrophobic interactions with soil organic matter (Brusseau, 2018; Campos-Pereira et al., 2023; Milinovic et al., 2015). However, organic carbon (OC) alone is often a weak predictor of PFAS sorption. The variability of K_{OC} reflects the contribution of multiple sorption mechanisms beyond hydrophobic partitioning, including electrostatic interactions, ion exchange, surface complexation, and hydrogen bonding (Lyu et al., 2022; H. Li et al., 2023; INERIS, 2024).

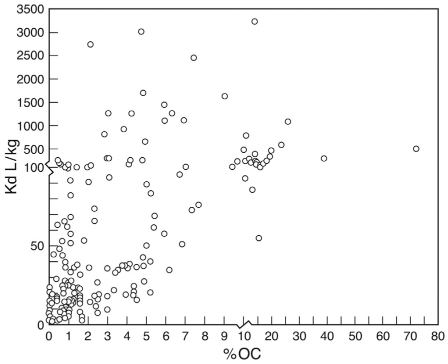

FIGURE 4.7: Relationship between peer-reviewed literature Kd values for PFOS and organic carbon (R2 =0.05, n=178) (Y. Li, Oliver, & Kookana, 2018).

4.3 Partitioning at the air-water interface

4.3.1 Role of the AWI in PFAS retention

As noted in SECTION 2.1, PFAS, being surface-active, have a strong affinity for interfaces. The air-water interface (AWI) in the vadose zone is strongly hydrophobic, and consequently PFAS tend to be retained as interfacial films. Given their amphiphilic nature, they orient at the interface, with the hydrophobic fluorinated tail in the air phase and the hydrophilic head in the aqueous phase, as shown in FIGURE 4.8 (Lyu et al., 2022).

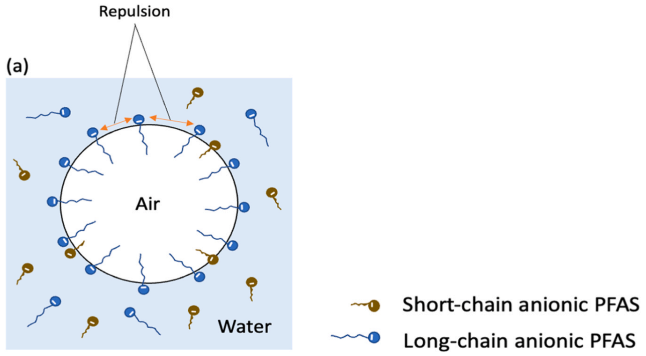

FIGURE 4.8: (a) Sorption of PFAS at the air-water interface of bubbles(modified from We et al., 2023).

Studies have shown that PFAAs can be enriched at the air-water interface by up to eight times their bulk water concentrations in the vadose zone, with enrichment factors increasing alongside alkyl chain length (Silva et al., 2019; ITRC, 2023). As PFAS tend to accumulate at the air-water interface, a growing number of field investigations have indicated that the vadose zone serves as a substantial reservoir for PFAS and that they may remain there for extended periods before migrating to groundwater (Lyu et al., 2022; Silva et al., 2019). Yet not well understood, the degree of retention within the vadose zone has important implications for both risk assessment and remediation strategies (Guo et al., 2020).

The AWI is a major retention mechanism for PFAS in the vadose zone (Brusseau, 2020; Lyu et al., 2022). Neglecting the AWI can lead to substantial underestimation of their mass and persistence in the vadose zone (Guo et al., 2020). For example, Brusseau (2018) reported that PFAS adsorption at the AWI can account for approximately 50% of the total mass retained in unsaturated porous media. FIGURE 4.9 from Brusseau (2018) illustrates a comparison between retention at the air-water interface and the solid-water interface in the vadose zone.

It should also be noted that a similar process occurs for PFAAs at **NAPL-water interfaces**. Although the magnitude of accumulation there appears to be much lower than at the air-water interface at environmentally relevant concentrations, sorption to NAPL-water interfaces and partitioning into bulk NAPL have been shown to contribute significantly to PFAS retention (Brusseau, 2018; Silva et al., 2019; Brusseau, 2020; ITRC, 2023). According to Brusseau (2018), NAPL partitioning was the predominant source of retention for FTOH, accounting for approximately 98% of the total.

The relative importance of each retention process depends on the properties and conditions of the system (e.g., PFAS constituent and concentration, porous medium, aqueous chemistry, fluid saturations, co-contaminants). When AWI or NAPL-water retention is significant, PFAS retardation in source areas is likely to exceed estimates based solely on solid-phase adsorption Brusseau, 2018.

However, the influence of partitioning at the air-water interface on PFAS transport can vary significantly. AWI-induced retardation within the soil profile is a transient property, as illustrated for PFOS in FIGURE 4.9, because it depends directly on the moisture content. Lower water saturation increases the AWI surface area, thereby improving PFAS accumulation and potentially delaying their downward migration, and vice versa. PFAS leaching may therefore be strongly influenced by weather conditions. During and after rainfall events, downward water flow can occur, while at the same time effective retardation due to the AWI decreases to near zero as soil saturation increases (Wallis et al., 2022). However, weather does not always have such a direct impact on saturation; it also depends on surface conditions and lithology.

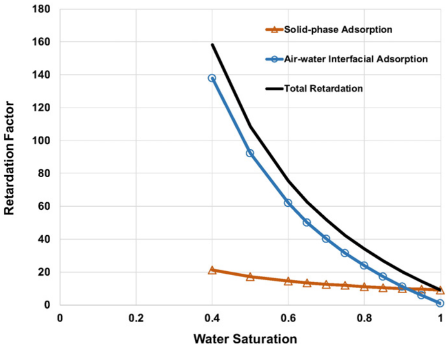

FIGURE 4.9: Impact of water saturation on PFOS retardation factors for solid-phase adsorption, air-water interface adsorption, and the sum of the two (total) Brusseau, 2018).

The AWI plays a far less significant role in the saturated zone, as there is almost no air. For instance, Brusseau (2018) reported that PFOS and PFOA exhibit low retardation (R < 10) when soils are fully saturated. However, the air-water interface present at the top of the groundwater table can still accumulate substantial amounts of PFAS.

The amount of PFAS retained at the air-water interface (AWI) depends on both the interfacial adsorption coefficient K_{aw}, which captures the interfacial affinity of a compound, and on the current AWI area A_{aw}.

4.3.2 AWI sorption coefficient K_{aw}

The air-water interfacial (AWI) sorption coefficient, denoted K_{aw}, quantifies the tendency of surface-active substances, such as PFAS, to accumulate at the air-water interface rather than remain dissolved in the aqueous phase. This property, also referred to as interfacial activity, reflects their capacity to modify interface properties, notably by lowering surface tension (Guo et al., 2020).

The value of K_{aw} is obtained from the surface excess concentration Γ described by the Gibbs adsorption equation (Brusseau & Van Glubt, 2019):

$$\Gamma = -\frac{1}{RT}\frac{\partial \sigma}{\partial \ln C_{\text{eq}}} \qquad [\text{mol/m}^2]$$

where σ is the surface tension (N·m^{-1}), C_{eq} is the equilibrium aqueous concentration of the solute (mol·m^{-3}), R is the universal gas constant (J·K^{-1}·mol^{-1}), and T is the absolute temperature (K). A decrease in σ with increasing C_{eq} indicates an accumulation of solute molecules at the interface, which forms the physical basis for calculating K_{aw} (Brusseau, 2018).

σ is described using the Szyszkowski equation, which relates surface tension to aqueous concentration (Guo et al., 2020):

$$\sigma = \sigma_0 \left[1 - b\ln\left(1 + \frac{C_{eq}}{a}\right)\right] \qquad [N/m]$$

where σ_0 is the surface tension of pure water, and a (mol/m^3) and b (-) are empirical fitting parameters obtained from surface tension isotherms.

By combining the Szyszkowski equation with the Gibbs adsorption equation, the AWI sorption coefficient is obtained as (Guo et al., 2020):

$$K_{\text{aw}} = \frac{\Gamma}{C_{eq}} = \frac{\sigma_0}{RT} \cdot \frac{b}{a + C_{eq}} \qquad [\mathrm{m}^3/\mathrm{m}^2]$$

where K_{aw} decreases with increasing C_{eq}, reflecting the non-linear nature of AWI sorption: retention is strongest at low PFAS concentrations and progressively weakens as the interface becomes saturated.

According to (Guo et al., 2020), this formulation is particularly important for modelling PFAS transport in unsaturated porous media, as it allows K_{aw} to vary dynamically with concentration in numerical simulations, capturing changes in retention under transient hydrological conditions.

4.3.3 AWI area A_{aw}

The maximum air-water interfacial area, A_{max}, is assumed to correspond to the total surface area of dry soil particles. This is calculated from the geometric mean particle diameter, which is derived from soil particle size distribution data. The latter is typically determined from sedimentation analysis, with textural class boundaries defined by particle size: in the Australian classification, the clay fraction has an upper size limit of 0.002 mm, the silt fraction of 0.02 mm, and the sand fraction of 2 mm (Wallis et al., 2022).

The geometric mean particle diameter, d_g, is computed as:

$$d_g = \sum_i m_i \ln d_i \qquad [\mathrm{mm}]$$

where m_i is the mass fraction of particle size class i and d_i is its arithmetic mean diameter (mm) (Wallis et al., 2022).

The specific surface area of the dry bulk soil (A_{max}) is then estimated from d_g, the soil bulk density σ_b (kg·dm^{-3}), and the particle density σ_s (kg·dm^{-3}) using:

$$A_{\text{max}} = \frac{600\,\sigma_b}{d_g\,\sigma_s} \qquad [\mathrm{dm}^2/\mathrm{dm}^3]$$

According to Wallis et al. (2022), the air-water interfacial area per unit soil volume (A_{aw}) is assumed to vary linearly with water saturation (S), ranging from zero at full saturation ($S = 1$) to A_{max} when the soil is dry ($S = 0$):

$$A_{\text{aw}} = A_{\text{max}}\,(1 - S) \qquad [\mathrm{dm}^2/\mathrm{dm}^3]$$

4.3.4 Controlling factors of the AWI retention

The evaluation of AWI retention processes remains an active area of study. Indeed, AWI retention depends on both the interfacial adsorption coefficient (K_{aw}) and the current AWI area (A_{aw}), which are influenced in different ways by various factors, sometimes showing non-proportional or even opposite trends.

- **Lithology**: According to Wallis et al. (2022), fine-textured soils (e.g., clay, silt) have a larger particle surface area, leading to larger A_{aw} at the same saturation and thus potentially higher AWI adsorption capacity. However, Guo et al. (2020) notes that sandy soils, due to greater drainage and weaker capillary forces, often have more air-filled pores and lower water content. This increases A_{aw} and can result in higher AWI retention. In contrast, silt and clay retain more water, which reduces available AWI in the vadose zone. Therefore, water content must be considered when assessing the influence of grain size distribution on AWI retention.

- **PFAS properties**:
    - **PFAS concentration**: At very low concentrations, a small increase in PFAS concentration produces a proportionally greater increase in surface excess, resulting in a higher K_{aw} value (Silva et al., 2019). However, as the total PFAS concentration in solution rises, available adsorption sites at the air-water interface progressively become saturated (Brusseau & Van Glubt, 2019). Beyond this point, adding more PFAS leads to a faster increase in aqueous concentration than in surface excess, causing K_{aw} to decline (Silva et al., 2019). Being surfactants, PFAS also reduce water surface tension (Γ), but this reduction becomes less pronounced per unit concentration increase once the interface is largely covered (Wallis et al., 2022). Consequently, at high PFAS concentrations, the contribution of AWI sorption to retardation in unsaturated porous media diminishes, potentially allowing PFAS to migrate more rapidly (Guo et al., 2020; Lyu et al., 2022; Wallis et al., 2022).
    - **Carbon chain length**: Longer-chain PFAS have greater hydrophobicity and are more surface-active, which provides a stronger driving force for interfacial adsorption. As a result, they generally exhibit higher K_{aw} values (H. Li et al., 2023; Lyu et al., 2022).
    - **Functional group (polar head)**: The type and charge of the functional group (e.g., carboxylate vs. sulfonate; anionic, cationic, zwitterionic, or non-ionic) strongly influence AWI adsorption. PFSAs generally have higher AWI sorption than PFCAs (Lyu et al., 2022; We et al., 2023).
    - **Isomer type**: Individual PFAS isomers, whether linear or branched, have different molecular structures, leading to variations in their physicochemical properties (Buck et al., 2011) and, consequently, differences in their K_{aw} values.
- **Solution chemistry**:
    - **Ionic strength**: Higher ionic strength (e.g., NaCl or $CaCl_2$) enhances PFAS accumulation at the AWI by reducing electrostatic repulsion between polar heads at the interface.
    - **Ionic composition / cation type**: Divalent cations (e.g., Ca^{2+}) generally have a stronger enhancing effect on AWI adsorption than monovalent cations (Brusseau & Van Glubt, 2019; Lyu et al., 2022; Silva et al., 2019).
    - **pH**: Changes in pH can alter the surface charge of the adsorbing phase and affect AWI adsorption (Brusseau & Van Glubt, 2019; Lyu et al., 2022).
    - **Presence of co-solutes**: Compounds such as ethanol, humic acids, or trichloroethylene generally have minor effects on PFAS interfacial adsorption at environmentally relevant concentrations (Brusseau & Van Glubt, 2019).
    - **Temperature**: While A_{aw} is not directly temperature-dependent, temperature can indirectly influence it via changes in soil water content caused by evapotranspiration Wallis et al., 2022. Higher temperatures typically reduce K_{aw} due to their effect on surface tension (Γ) (Guo et al., 2020).

4.4 Climate-driven physical flow processes

Often overlooked when studying PFAS transport in the subsurface, climate-driven physical flow processes have a big impact on PFAS mobility. As discussed in the SECTION 4.3, PFAS are mainly mobile when water is available to carry them. Rainfall, evaporation, and soil water content strongly influence downward movement and drainage.

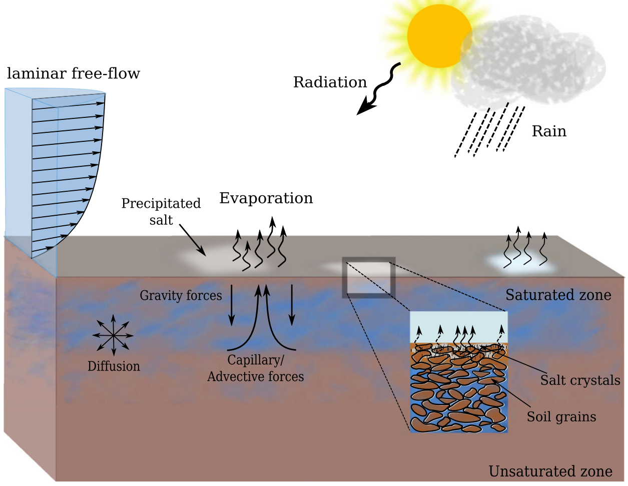

FIGURE 4.10: Relevant physical transport processes influencing the subsurface and surface such as the wind, solar radiation, rainfall events, evaporative water loss and exchange fluxes at interface between subsurface and surface (Jambhekar et al., 2015).

In dry climates like Australia, evapotranspiration can cause upward fluxes, retaining PFAS within the shallow soil horizons during summer. In contrast, during wetter periods with rain events and downward flux, PFAS become mobilised and PFAS concentration and mass decrease. For example, over a 10-day period with three rain events, surface soil saturation may rise from 50-60% to nearly 100%, temporarily eliminating the air-water interface and allowing PFAS to desorb into pore water (Wallis et al., 2022).

Guo et al. (2020) highlight the central role of rainfall-driven saturation dynamics and AWI storage in controlling PFAS retention and pulse release in the vadose zone. In addition, they hypothesise that groundwater table dynamics could play an important role in PFAS retention. Fluctuations in the water table may influence soil water saturation and thus the extent of air-water interfaces, particularly when the vadose zone is relatively shallow. They note that "*[...], not including the groundwater table dynamics will likely overestimate the retention of PFAS in the vadose zone*". However, based on my personal experience studying a site in the Netherlands, a rising groundwater table following an extreme rainfall event could lead to increased PFAS concentrations near the surface. This would occur due to the subsequent release of PFAS retained at the air-water interface above the water table as it subsides.

When evaluating PFAS environmental risk, secondary sources may also be forgotten. However, these arise from surface runoff, atmospheric deposition of airborne foam, or floodwaters redistributing contaminants. It is then important to consider the different climate-driven physical flow processes that could happen when PFAS were realised on surface as AFFF for example. These potential secondary sources of PFAS can reside in very shallow horizons and be mobilised by fluids later (Buck et al., 2011; ITRC, 2023).

4.5 Mobility and distribution of PFAS in the vadose zone

As demonstrated throughout this chapter, the four parameters discussed above strongly influence the distribution and mobility of PFAS in the vadose zone. The presence of PFAS precursors can lead to greater retention within the vadose zone and delayed release. In addition, the lithological properties of the soil, together with the chemistry of infiltrating rainfall, may significantly affect PFAS retention on both the solid matrix and the air-water interface. Finally, climate-driven physical flow processes also play a major role in the mobility of PFAS compounds.

Based on Guo et al. (2020), Institut national de l'environnement industriel et des risques (INERIS) (2024), Lyu et al. (2022), Rasmusson and Fagerlund (2024), and Wallis et al. (2022), PFAS concentrations in soil can be considerably higher in the vadose zone than in groundwater under specific conditions. For example, Guo et al. (2020) report that an analysis of 324 Air Force sites across the continental United States impacted by AFFF showed that in the vast majority of cases (87%), higher PFAS concentrations were observed in soil within the vadose zone.

As our study is primarily based on the comparison between a temperate climate and a Mediterranean one, a review of the main factors influencing PFAS retention under these two conditions was carried out.

- The conditions examined by Wallis et al. (2022) correspond to Mediterranean settings with clayey soils, whereas Guo et al. (2020) investigated semi-arid conditions with sandy soils. Their findings under hot climatic conditions show that PFAS tend to be retained within the upper 2 m of the soil profile, with the vadose zone acting as a long-term reservoir. Evapotranspiration concentrates contaminants in the shallow horizons, while extensive adsorption at air-water interfaces under low water contents strongly delays downward migration. In contrast, downward PFAS transport occurs mainly during rainfall events, when soils approach saturation and AWI retention is temporarily reduced.
- Under temperate and humid environmental conditions, the mobility and distribution of PFAS in the vadose zone differ significantly from those in drier climates, primarily due to contrasting hydrological regimes. PFAS are generally more mobile and migrate more rapidly because of higher water fluxes and enhanced leaching towards the groundwater (Guo et al., 2020). Retardation factors for PFOS are overall lower under humid conditions compared to semi-arid ones, indicating that PFAS can reach groundwater within only a few decades (Guo et al., 2020). These environments also maintain a higher average soil water content, which reduces the air-water interfacial area available for sorption (Guo et al., 2020). Although AWI adsorption remains a main retention mechanism in unsaturated soils, its role is strongly diminished under high saturation (Guo et al., 2020; Lyu et al., 2022). In addition, water flow processes (advection, infiltration) exert greater control over PFAS fate, while higher infiltration rates shorten residence times in the vadose zone (Wallis et al., 2022).

It is, however, important to nuance these findings, as PFAS leaching varies between sites. For example, results would differ greatly in organic-rich soils or where preferential flow occurs, as highlighted by Wallis et al. (2022). This underscores the need to evaluate vadose zone processes when assessing source-zone risks.

4.6 Mobility and distribution of PFAS in the saturated zone

The mobility of PFAS under saturated conditions is high, not only because of their strong solubility but also due to their persistence, as they do not degrade in the environment except into smaller PFAS. Once PFAS reach groundwater, they remain mobile. With the air-water interface absent and Kd typically low, PFAS and their precursors migrate readily (Hatton et al., 2018; H. Li et al., 2023). Their movement is highly influenced by subsurface heterogeneity and lithology (H. Li et al., 2023; Lyu et al., 2022). They can therefore travel significant distances from their source, even at low but relevant concentrations. Compared to hydrocarbon plumes, which typically extend a few hundred metres, PFAS plumes can span several kilometres (Newell & Connor, 1998; Rasmusson & Fagerlund, 2024).

It is still important to note that compare to other pollutant such as hydrocarbons, PFAS have unique properties but also very low regulatory thresholds (see SECTION B), which contribute to the apparent extent of contamination .

Historically, PFAS source zones have involved widespread AFFF use, particularly on flat terrains with drainage channels, such as military bases and airports. Understanding the mass balance of PFAS at these sites is complex: how much remains in the soil, how much is lost to drainage, and how PFAS partition between soil, groundwater, and surface water remain open questions (Interstate Technology & Regulatory Council (ITRC), 2023). Large plumes may result from primary contamination, but also from infiltration over large areas and secondary sources (Lyu et al., 2022; Rasmusson & Fagerlund, 2024).

Unlike degradable or highly sorbing pollutants, PFAS plumes reflect geological heterogeneity (Rasmusson & Fagerlund, 2024). It is then not appropriate to use the convection-dispersion equation (CDE) mainly representative for homogeneous settings (Hutson, 2003; Lyu et al., 2022; Rasmusson & Fagerlund, 2024). In PFAS-contaminated areas, scattered hotspots are often observed, sometimes isolated in otherwise clean zones. Conventional models may underestimate early arrival due to heterogeneity (H. Li et al., 2023; Lyu et al., 2022). The main uncertainties remain in the runoff partitioning, precursor transformation, and rainfall-driven inputs. Secondary sources, such as flooding and drainage, further complicate predictions, making PFAS mobility highly site-specific.

Part II

Modelling PFAS leaching under contrasting climatic conditions

Organisation of the Modelling Section

1. CHAPTER 5 - Presents the transport equations used to represent PFAS leaching in the vadose zone, and an overview of modelling tools.
2. CHAPTER 6 - Explains how the Australian model from Wallis et al. (2022) was reproduced, step-by-step solely on the information provided in the article.
3. CHAPTER 7 - Describes how the model was adapted to Belgian climatic conditions to assess meteorological impacts.

Chapter 5

Modelling PFAS transport in the subsurface

5.1 Introduction to LEACHM

Several numerical tools exist to simulate flow and contaminant transport in unsaturated soils. However, LEACHM is among the few that have been applied to PFAS studies. It is a one-dimensional modelling package developed at Cornell University (USA) by John L. Hutson and R. J. Wagenet (Hutson, 2003).

LEACHM (Leaching Estimation And Chemistry Model) is designed to simulate water and solute movement, plant uptake, and chemical reactions in the vadose zone. It has several variants sharing a common framework, including LEACHN (nitrogen and phosphorus), LEACHP (pesticides), and LEACHC (inorganic ions). Its source code, written in Fortran, is available for review and modification, and the model has been widely compared with similar tools (e.g., HYDRUS) for water flow and solute transport. Over time, LEACHM has evolved in response to research needs and user feedback, with some changes introduced without prior announcement (Hutson, 2003). This study uses LEACHP, originally developed for pesticides and later adapted to include sorption of PFAS compounds to the air-water interface (AWI), following largely the approach of Guo et al. (2020).

To run LEACHM, input files are prepared in Excel workbooks with macros, and a separate utility is available to convert daily meteorological data into the required format. The main output files include (Hutson, 2003):

- `.out`: mass-balance summaries and depth-specific data for each segment;
- `.sum`: time series recorded at print intervals for predefined depth macro-segments;
- `.btc`: breakthrough curves showing cumulative water and chemical fluxes at the lower boundary;
- `.grd`: depth by time grids for variables such as water, temperature, and chemical concentrations.

LEACHM is a process-based model that employs a finite difference approximation of the Richards equation to simulate water flow, and the convection-dispersion equation to model solute transport in variably saturated soils. Water and solute movement through the unsaturated zone is computed in response to time-varying precipitation, evaporation, transpiration, temperature, and runoff (Wallis et al., 2022). As this study relies on LEACHM, the following sections present its mathematical formulations, required input parameters, and a discussion of its main limitations.

5.2 Water flow equations in unsaturated soil

In unsaturated soils, water flow is described by the Darcy-Buckingham law, which extends Darcy's law by making hydraulic conductivity (K) dependent on volumetric water content (θ) or pressure head (h). As θ decreases during soil drying, $K(\theta)$ also declines, slowing the movement of water and solutes. This variability in hydraulic properties makes modelling flow in the vadose zone more complex than in saturated systems. The Darcy-Buckingham law is expressed as (Guo et al., 2020):

$$q = -K(\theta) \cdot \left[\frac{dh}{dz} - 1 \right] \qquad [mm/d]$$

where q is the volumetric flow of wate or Darcy flow (positive downwards), K is hydraulic conductivity (mm/d), $\theta = \phi' S$ is the volumetric water content (mm^3/mm^3), $\frac{dh}{dz}$ is the matric potential (-), h is the soil water pressure head (mm), z is depth (mm) (positive downwards). The parameter ϕ' is the porosity of the porous medium (mm^3/mm^3) and S the water saturation (-) (Guo et al., 2020).

The Richards equation extends Darcy-Buckingham by combining it with the principle of mass conservation, allowing transient flow simulation in variably saturated soils (Xiong, 2014). In its one-dimensional mixed form, as used in LEACHM, it is written as (Hutson, 2003):

$$\frac{\partial \theta}{\partial t} = \frac{\partial}{\partial z} \left[K(\theta) \left(\frac{\partial H}{\partial z} \right) \right] - U(z,t)$$

where t is time (d), H = h - z is the hydraulic head (mm) and U is a sink term representing water lost per unit time by transpiration (plant water uptake) (d$^-$1).

5.3 Solute transport equations

Once water fluxes are calculated using the Richards equation, chemical fluxes are derived from a numerical solution of the convection-diffusion equation (CDE), accounting for sorption as well as solute sources and sinks (Hutson, 2003). In LEACHM, the transport of a chemical through soil can occur via four distinct processes (Hutson, 2003):

- Diffusion in the liquid phase: Movement of the chemical in response to an aqueous concentration gradient.
- Diffusion in the gas phase: For volatile chemicals, movement in response to a gradient in gas concentration.
- Convection in the liquid phase: Mass flow of the chemical resulting from the movement of water in which it is dissolved.
- Convection in the vapour phase: Transport with moving air, driven by barometric pressure fluctuations, wetting and drying cycles, and variations in water table depth.

The convection-dispersion equation (CDE) provides the mathematical framework for this type of solute modelling, in which dispersion is explicitly represented. More specifically, the dispersion coefficient ($D(\theta, q)$) in the CDE accounts for both mechanical dispersion (arising from local variations in velocity and flow paths within soil pores) and molecular diffusion in the aqueous and gaseous phases (Hutson, 2003).

As the user manual in my possession had not yet been updated to include the recent modifications to LEACHM, the CDE presented in Hutson (2003) does not contain any term representing air-water interfacial adsorption. Based on the work of Guo et al. (2020) and Wallis et al. (2022), it has been attempted to determine the CDE currently implemented in LEACHM for one-dimensional solute transport in variably saturated soils.

$$\frac{\partial C_T}{\partial t} = \frac{\partial}{\partial z} \left[\theta D(\theta, q) \frac{\partial C_{eq}}{\partial z} - (q C_{eq}) \right] \pm \phi$$

where C_T is the total solute concentration per unit bulk-soil volume ($\mu mol/mm^3$), $D(\theta, q)$ is the apparent dispersion coefficient (mm^2/s), C_{eq} is the equilibrium aqueous concentration (μ mol/mm^3), q is Darcy flow (mm/d) and ϕ represents as yet unspecified sources or sinks of solute. The sink terms can represent the net effects of chemical transformations, degradation, and plant uptake.

- According to Hutson (2003), the total solute concentration in a soil control volume is the sum of its quantities in all simulated phases (solution, sorbed and gas phases). Based on Guo et al. (2020), it has been assumed that it also comprises the concentration sorbed at the AWI (C_{aw} [μmol/mm^3]):

  $$C_T = \theta\, C_{eq} + \rho_b\, C_s + \varepsilon\, C_g + C_{aw} \qquad [\mu\text{mol}/\text{mm}^3]$$

  where C_s is the solid-phase sorbed concentration (μmol/g), ρ_b is the bulk density (g/mm^3), C_g is the gas-phase concentration (μmol/mm^3), and ε is the air-filled porosity (-). The latter represents the difference between the volumetric water content at saturation (θ_s) and the actual volumetric water content (θ).

  When C_{eq} exceeds the solubility limit, the excess is allocated to a precipitated pool, considered a separate phase (not included in C_s) and generally assumed inert while in the precipitated state (Hutson, 2003). In model outputs, "solution" fields ($\text{mg}\,\text{L}^{-1}$) report only the dissolved phase at equilibrium ($\text{C}_e q$), whereas "total" outputs include all phases present, expressed in user-selected units before the simulation [$\mu\text{g}\,\text{kg}^{-1}$ (1), $\text{mg}\,\text{m}^{-2}$ per segment depth (2), $\text{mg}\,\text{kg}^{-1}$ (3), $\text{g}\,\text{m}^{-2}$ (4), $\text{kg}\,\text{ha}^{-1}$ (5), $\text{ng}\,\text{kg}^{-1}$ (6)].

  To model PFAS leaching in the vadose zone with LEACHM, at the time of the project, sorbed concentrations on the different phases were based solely on equilibrium isotherm formulations and assumed to follow linear sorption. Consequently, it is only possible to use the linear distribution coefficient K_d for solid-phase sorption, but not the Freundlich coefficient K_f (see SECTION 4.2). In addition, partitioning of a substance into the gas phase is described using the equilibrium Henry's constant K_H^* (see SECTION 3.7). Finally, the concentration sorbed at the air-water interface, C_{aw}, has the following form according to Guo et al. (2020):

  $$C_{aw} = A_{aw}\Gamma = C_{eq}A_{aw}K_{aw} \qquad [\mu\text{mol}/\text{mm}^3]$$

  where A_{aw} is the AWI area (cm^2/cm^3), Γ is the surface excess at the air-water interface (μmol/cm^2) and K_{aw} is the AWI sorption coefficient (cm^3/cm^2).(see SECTION 4.3).

  The total concentration C_T can therefore be expressed in terms of aqueous concentration C_L and phase-partitioning coefficients such as:

  $$C_T = C_{eq}\left(\theta + \rho_b K_d + \varepsilon K_H^* + A_{aw}K_{aw}\right) \qquad [\mu\text{mol}/\text{mm}^3]$$

  Given that PFAS are only slightly, if at all, volatile, K_H can generally be neglected.

- $D(\theta, q)$ is the apparent dispersion coefficient (mm^2/d), which accounts for the combined effects of mechanical dispersion, aqueous-phase molecular diffusion, and gas-phase molecular diffusion on solute transport. It is expressed as

  $$D(\theta, q) = \frac{D_p(\theta)}{\theta} + D_M(q) + \frac{D_{OG}K_H^*}{\theta}$$

  where:

  - $D_p(\theta)$ is the effective aqueous-phase diffusion coefficient (mm^2/d), dependent on the volumetric water content θ. It is derived from the diffusion coefficient in pure water and adjusted using empirical constants, as described in LEACHM (Hutson, 2003).
  - $D_M(q)$ is the mechanical dispersion coefficient (mm^2/d), representing mixing between large and small pores caused by variations in mean water flow velocity. It is estimated from the pore water velocity ($v = q/\theta\ mm/d$) and the longitudinal dispersivity (α_L), which in LEACHM is generally limited to a range proportional to depth.
  - D_{OG} is the effective gaseous diffusion coefficient in soil air (mm^2/d), obtained from the diffusion coefficient in free air corrected by a tortuosity factor (T) that accounts for air-filled porosity. Gas-phase diffusion is linked to aqueous concentration gradients via Henry's law constant K_H^*.

Gas-phase convection can significantly enhance the mobility of volatile compounds in soils. Variations in soil water content, barometric pressure, and temperature can induce air flow through the pore space. LEACHM accounts for these effects by allowing a gas diffusion coefficient enhancement term to be specified in the input file. Field observations indicate that fluctuations in barometric pressure and water table levels can substantially increase the effective gas-phase diffusion coefficient. After corrections for tortuosity and air-filled porosity, this enhancement may become the dominant contribution to gas-phase transport (Hutson, 2003).

- It should be noted that the term in the equation "$-qC_{eq}$" represents the advective process. In fact, together with the mechanical dispersion coefficient $D_M(q)$, it is used to calculate the convective transport of the solute through the porous medium.

5.4 Input parameters

Accurate modelling requires reliable input parameters. In this section, the parameters required for the operation of the model simulating PFAS leaching are presented. In LEACHM, many of the parameters needed for the water flow equation (Richards' equation) and the solute transport equation (Convection-Dispersion Equation CDE) are not entered directly. Instead, they are calculated or adjusted internally by the model from more fundamental input data (Hutson, 2003).

5.4.1 Parameters required for the Richards' equation

Water flow is computed by the subroutine `WATFLO` in LEACHM, using the relationships between hydraulic conductivity (K), volumetric water content (θ) and matric potential (h). The following parameters must be provided:

- **Soil water retention and hydraulic conductivity functions:** These can be specified directly by entering the parameters of either the Campbell model, as modified by Hutson and Cass (constants a, b and pore parameter p), or the van Genuchten model (α, n, and residual water content θ_r). As Campbell parameters have been used in this project, this method has been examined in greater detail in APPENDIX C in order to better understand each parameter and its influence on PFAS leaching.
- **Alternatively**, LEACHM can estimate these functions from *pedotransfer functions*, in which case the following must be provided:
  - Soil texture: clay (%), silt (%), and sand (%).
  - Bulk density (ρ_b).
  - Organic carbon (OC) content (%) or organic matter (OM) content, noting that OM can be calculated from OC.
  - Particle density (ρ_s), used to compute soil porosity.
- Saturated hydraulic conductivity (K_s).
- A conductivity matching factor: a value of K at a given water content or matric potential, used to refine $K(h)$ estimation in the unsaturated range.

5.4.2 Parameters required for the Convection-Dispersion Equation (CDE)

Solute transport is computed by the subroutines `SOLN`, `SOLP`, and `SOLC` in LEACHM. The main groups of parameters are as follows (Hutson, 2003):

Partitioning processes

- **Solid-water interface partitioning:** The solid-water partition coefficient (K_d) is calculated from the organic carbon-water partition coefficient K_{oc} (L/kg) of the compound and from the organic carbon fraction f_{oc} for each soil layer.

- **Air-water partitioning:** For sorption at the air-water interface (AWI), LEACHM requires the parameters a and b from the K_{aw} relationship (see SECTION 4.3.2). These are compound-specific fitting parameters.
- **Gas-phase partitioning:** Although K_H^* can be calculated from the saturated vapour density c_G^* and aqueous solubility c_L^* (both in mass/volume units).

Dispersion and diffusion coefficients

- Aqueous-phase molecular diffusion coefficient (D_{OL}) used to calculated $D_p(\theta)$, which is internally adjusted for tortuosity and water content.
- Longitudinal dispersivity (α_L), which together with pore water velocity (v) (calculated by the model determines the mechanical dispersion coefficient $D_M(q)$.
- Gas-phase molecular diffusion coefficient in air (D_{OG}), also corrected internally for air-filled porosity and tortuosity. This linked with the dimensionless Henry's law constant (K_H^*) already discussed.
- Barometric enhancement term to simulate gas-phase convection effects due to fluctuations in barometric pressure or water table level.

Advection term

- There is no direct input parameter for advection; instead, it is determined internally from:
  - the water flux q (computed from the Richards' equation using the hydraulic parameters and boundary conditions provided by the user),
  - the equilibrium aqueous concentration C_{eq} (calculated from the total solute concentration and the partitioning coefficients input by the user).

5.5 Model-specific limitations for PFAS applications

In LEACHM, PFAS sorption is restricted to a linear, instantaneous equilibrium formulation for both solid-phase and air-water interface (AWI) adsorption, with no option for non-linear or kinetic (two-site) models. However, when AWI sorption is not required, contaminants can be simulated using the kinetic sorption option, in which a fraction of sites is in local equilibrium (instantaneous) while the remainder is governed by rate-limited sorption and desorption. This approach better represents cases where compounds adsorb rapidly but desorb slowly, as is often observed in real soils (Hutson, 2003). More advanced models such as continuous-distribution, multi-rate models that incorporate a continuous distribution of domains also exist but are not available in LEACHM. They associated sorption/desorption rate coefficient and are also available in the literature (Guo et al., 2020)

The model does not account for surfactant-induced changes in flow properties (e.g., surfactant-driven flow), thereby neglecting potential feedbacks between PFAS chemistry and hydrodynamics. This may lead to overestimation of retention near saturation, producing overly conservative and potentially unrepresentative leaching predictions (Wallis et al., 2022).

Estimation of the air-water interfacial area (AWI) in LEACHM relies on particle size, bulk density, and particle density, a practical approach for field applications where detailed data are often scarce. However, the model developers acknowledge that direct measurements of soil surface area, such as through aqueous-phase interfacial partitioning tracer tests or X-ray microtomography, could yield more accurate AWI estimates. Incorporating such measurements would likely improve the precision of sorption-related parameters and, consequently, enhance the reliability of PFAS leaching simulations (Wallis et al., 2022).

Diffusion coefficients in LEACHM are defined globally for all substances, even though different compounds may have distinct transport properties. To avoid unrealistic behaviour, it is advisable to model substances with broadly similar diffusion characteristics.

As a one-dimensional model, LEACHM assumes homogeneous soil and cannot represent heterogeneity or preferential flow paths, which can be critical in structured or layered soils (Hutson, 2003; Wallis et al., 2022).

Furthermore, LEACHM is fully text-based, offers no integrated calibration or visualisation tools, and outputs results only for predefined macro-segments (.sum and .btc files), rather than at user-defined locations. This limits flexibility for high-resolution diagnostics and iterative sensitivity testing.

Despite these limitations, LEACHM remains well suited for data-scarce conditions and field-scale assessments (Wallis et al., 2022).

Chapter 6

Modelling of PFAS leaching under Mediterranean conditions

6.1 Conceptual model

The first step in reproducing the model of Wallis et al. (2022) is the development of a conceptual model that best represents and clarifies the physico-chemical processes and interactions of PFAS at the site described in the scientif paper. This is achieved by using all the information provided in the paper and making reasonable assumptions for parameters not explicitly documented.

6.1.1 Objectives of the model

The objectives of this Australian model are the same as Wallis et al. (2022) conceptual model:

1. Determine the mobility of perfluoroalkyl and polyfluoroalkylated substances (PFAS) through the unsaturated zone under realistic field conditions.
2. Better understand the historical fate of PFAS at a typical military site affected by fire-fighting foam applications (AFFF) for decades.
3. Predict future PFAS mass loading rates towards the saturated zone (groundwater).
4. Assist in the design of effective and economical remediation measures for PFAS contaminated sites.
5. Assess the relative importance of physical flow and transport processes compared to physico-chemical retention mechanisms on the global mobility of PFAS and mass loading rates
6. Provide a plausible explanation of the persistence of PFAS compounds in the first two meters of the unsaturated zone.

6.1.2 Description of the site

As stated in Wallis et al. (2022), "the selected study site is representative of many other, similarly PFAS-impacted sites. It is located on Australian Commonwealth land, where training with AFFF occurred over several decades." The authors also specify that such sites include military base, airport, and industrial locations where AFFF was periodically applied over decades during firefighting training exercises.

6.1.3 Scale

The model developed by Wallis et al. (2022) is applied at the field scale, representing a vertical profile typical of a contaminated site in Australia (see FIGURE 6.1). It is designed with the aim of simulating PFAS transport through the vadose zone under realistic conditions.

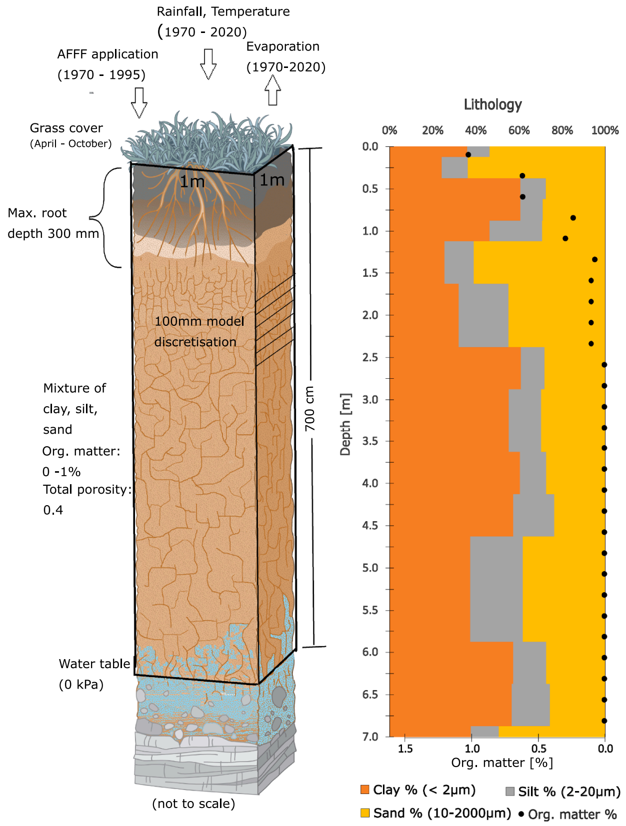

FIGURE 6.1: (a) Model Set-up; (b) Lithological profile of soil column from 0 to 7 m and organic matter content at field site based on analysis of drilling core. FIGURE modified after Selker and Or (2019).

6.1.4 Dimension

The model uses a one-dimensional vertical soil profile extending to 7 metres, representing the full depth of the unsaturated zone at the study site. One of its limitations is that it does not attempt to capture field-scale heterogeneity and assumes lateral homogeneity. As a result, it cannot represent potential preferential flow paths, which may have a significant impact on PFAS leaching.

6.1.5 Discretisation

In LEACHM, the soil profile is discretised into uniform horizontal segments to facilitate numerical simulations. For this study, the vertical soil profile was discretised over a total depth of 7 metres using segments of 100 mm thickness (see FIGURE 6.1), resulting in 70 segments. Each segment represents a uniform control volume, with its centre corresponding to a calculation node. In addition to these 70 internal nodes, two boundary nodes are included: one above the soil surface and one below the bottom of the profile. These are used to apply boundary conditions but are not listed in the model output files. Therefore, the model includes 72 nodes in total.

The choice of 100 mm segment thickness corresponds to common practice for field-scale simulations in LEACHM, where typical segment thicknesses range from 25 mm to 100 mm. This level of discretisation offers a reasonable compromise between simulation accuracy and computational efficiency, while also ensuring compatibility with dispersivity values typically used at this scale (Hutson, 2003).

6.1.6 Boundary condition for water flow and transport at the upper node

In LEACHM, the upper boundary condition governs how water enters or leaves the soil surface, and its behaviour at the surface node is determined by several factors including climatic inputs, soil hydraulic properties, and vegetation characteristics (Hutson, 2003).

For the model developed by Wallis et al. (2022), this boundary condition is controlled by daily climate data from the SILO database (Queensland Government, 2024), including rainfall, temperature, and potential evapotranspiration. According to Wallis et al. (2022), the studied site is located in a Mediterranean climate zone in Australia. Based on references to Australian Defence documents cited in their paper, it has been assumed that the climate data used in their model correspond to the one of RAAF Base Edinburgh in Adelaide. The dataset covers a 50-year period from 1970 to 2020.

The simulated site is covered with grass with a maximum rooting depth of 300 mm. Plant growth was programmed to start in April, peak in late June, and cease in October each year. According to Hutson (2003), vegetation influences water and solute movement in the vadose zone through processes such as root water uptake and evapotranspiration.

At the surface node, different flow scenarios are handled depending on the balance between atmospheric inputs and soil infiltration capacity (Hutson, 2003):

- **During infiltration without ponding**, water enters the soil as a flux-controlled process. The infiltration rate is limited by the hydraulic conductivity and matric potential gradient between the atmospheric node (node 1) and the surface node (node 2).
- **If ponding occurs**, the matric potential at the surface node is set to zero.
- **During evaporation**, water is extracted from the topsoil as long as hydraulic conditions allow.
- **When surface flux exceeds infiltration capacity**, the excess is treated as runoff.

Some surface runoff may occur on-site, as a slope of 0.5% and a water retention depth of up to 500 mm are considered. As not specified in Wallis et al. (2022) model, no surface crusting is assumed.

6.1.7 Boundary condition for water flow and transport at the lower node

The lower boundary condition is defined as a unit gradient (free drainage), allowing water to exit the bottom of the profile at a rate equal to the hydraulic conductivity at that depth. This condition was likely chosen by Wallis et al. (2022) given that the water table is relatively deep and varies depending on the site location. While the actual groundwater table at the field site ranges between approximately 4 and 10 metres, the model simulates a 7-metre deep vadose zone and applies a free drainage condition at its lower boundary to represent downward water flow towards a deeper, unspecified aquifer without explicitly fixing the water table depth within the model domain.

6.1.8 Boundary condition for solute transport at the upper node

Solute transport at the upper boundary is closely linked to water movement, but also depends on the chemical properties of the compounds and processes such as sorption and volatilisation (Hutson, 2003).

- **During infiltration events**, the solute concentration at the surface node (node 1) is set equal to that of the applied water (rainfall or irrigation), and diffusion is ignored at the surface.
- In contrast, **during evaporation**, the solute flux of non-volatile compounds like PFAS is set to zero, leading to evapoconcentration in the surface segment.
- LEACHM can estimate **runoff**, but without explicitly modelling chemical loss via surface water. Chemical loss is estimated through the use of indexes and hypothesis instead of a specific mechanical process.

Wallis et al. (2022) assumed that aqueous film-forming foams (AFFF) were released at the soil surface of the site between 1970 and 1995. To simulate this, a total PFAS concentration was introduced into the liquid phase via monthly irrigation events over this period. During each event, 10 mm of water per m^2 was applied to the surface, with the total PFAS concentration set at 8 mg/L. This input was added to natural precipitation, which was assumed to contain no PFAS, as was the initial background soil concentration. A conservative tracer (chloride) was also injected under conditions identical to those of PFAS (injection period, volume, and concentration) to compare water transport in the subsurface with that of PFAS.

6.1.9 Boundary condition for solute transport at the lower node

In the case of a unit hydraulic gradient, water is assumed to flow only downward, and the solute concentration at the bottom node does not affect the simulation. Water drains at a rate equal to the current hydraulic conductivity at the base of the model (Hutson, 2003).

6.1.10 Flow regime: transient

The model operates under transient conditions with daily rainfall and evapotranspiration inputs, simulating seasonal variations over several decades.

6.1.11 Parameters needed for the model

TABLE 6.1: Summary of the parameters used in the simulations.

Parameter	**Value**	**Unit**
Soil physical parameters		
Particle density (ρ_s)	2.67	kg/dm^3
Bulk density (ρ_b)	1.60	kg/dm^3
Soil hydraulic parameters		
Dispersivity (α_L)	100	mm
Aqueous diffusion coefficient (D_{OL})	44.93	mm^2/day
Molecular diffusion coefficient in air (D_{OG})	430,000	mm^2/day
Air diffusion enhancement factor	140,000	mm^2/day
Air-entry matric potential (a)	-0.9	kPa
Slope of retention curve (b)	8.5	(-)
Pore interaction parameter (p)	1	(-)
Saturated hydraulic conductivity (K_s)	700	mm/day
Field capacity	-20	kPa
Chemical properties - PFAS total		
Molecular weight	500	g/mol
Solubility	10,000	mg/L
K_{OC}	90	L/kg
K_{aw}: a constant	0.059	μmol/cm^3
K_{aw}: b constant	0.12	(-)
Chemical properties - Chloride		
Molecular weight	35	g/mol
Solubility	100,000	mg/L

Furthurmore, it should be noted that:

- For the soil physical properties,

  - The soil granulometry and the total organic carbon (TOC) of each node of the model have been fixed by relying on the FIGURE 6.1 from Wallis et al. (2022) study.
  - Matric potential: a two-year spin-up period prior to the start of the simulation, and driven by precipitation, was used to establish a realistic matric potential profile by 1970.

- For the water retention curve parameters and conductivity data, no information is provided regarding the method used to define the soil water retention curve in the model presented by Wallis et al. (2022).

  Since the parameters required for the water retention function are unknown, LEACHM can estimate them using pedotransfer functions. Each function proposed by LEACHM corresponds to a different empirical equation. These functions rely on easily measurable soil properties, such as particle size distribution, bulk density, and organic matter content. A pedotransfer function based on a model specifically developed for Australian soils was tested first. However, the results obtained with this initial approach were inconclusive. This could be explained by the fact that these regression models are subject to uncertainty and are region-specific (Hutson, 2003).

  The method of Campbell (1974), as modified by Hutson & Cass (1987), is therefore selected to better represent the water retention behaviour of the soil under study. This method is typically used when the constants a, b and p are already known from laboratory measurements or previous studies. However, since such information is not provided by Wallis et al. (2022), the model has been calibrated manually by adjusting the parameters within a plausible range for a soil mainly composed of silt and clay. This method is described in APPENDIX C to clarify the origin and meaning of the parameters used and their influence on the model.

- For the chemical properties, since the observed plume at the site studied by Wallis et al. (2022) was dominated by PFOS, the properties assigned to the simulated total PFAS primarily reflect those of this compound. Furthermore, no degradation or transformation of the total PFAS is assumed to occur on site.

6.2 Comparison with Wallis (2022) meteorological conditions

Based on the conceptual framework, a numerical model is implemented using LEACHM to generate results comparable to those of Wallis et al. (2022).

This section assesses whether the physical water-flow processes in the vadose zone of the reproduced model are representative of those in the model of Wallis et al. (2022). Because these processes are strongly climate-driven, the following metrics are compared between the two models: (i) infiltrating rainfall and surface runoff (FIGURE 6.2), (ii) soil-surface temperature and matric potential within the top 100 millimetres (FIGURE 6.3), and (iii) groundwater recharge (FIGURE 6.4). These metrics are first presented in three figures and then discussed.

6.2.1 Rainfall and runoff

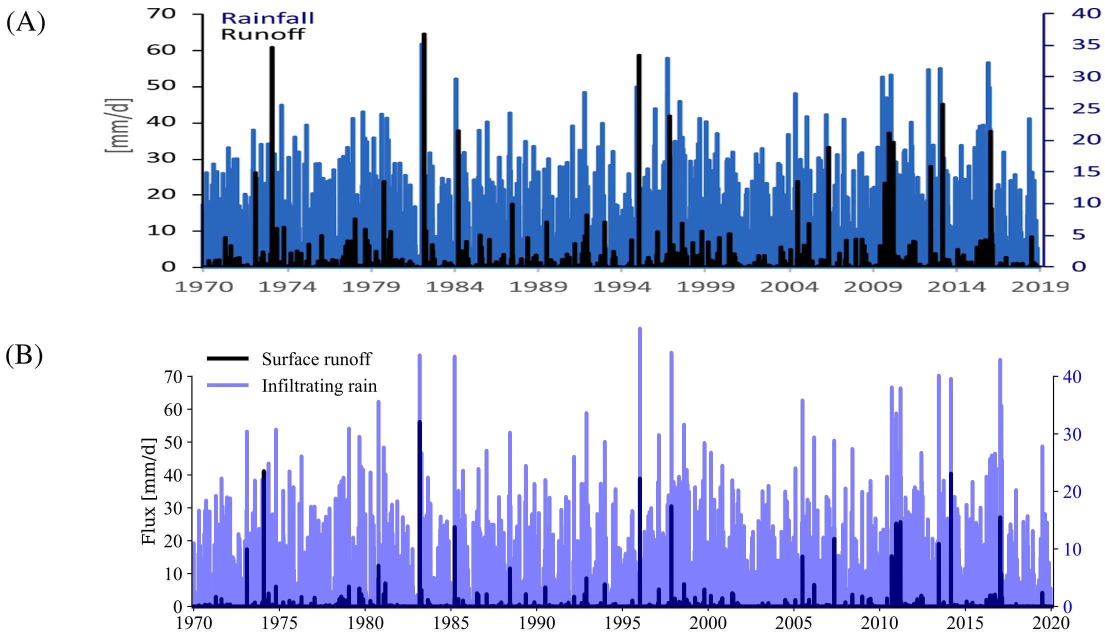

FIGURE 6.2: Daily infiltrating rainfall [mm/d] and surface runoff [mm/d] for (A) the Wallis et al. (2022) model and (B) for the reproduced model

6.2.2 Temperature and matric potential

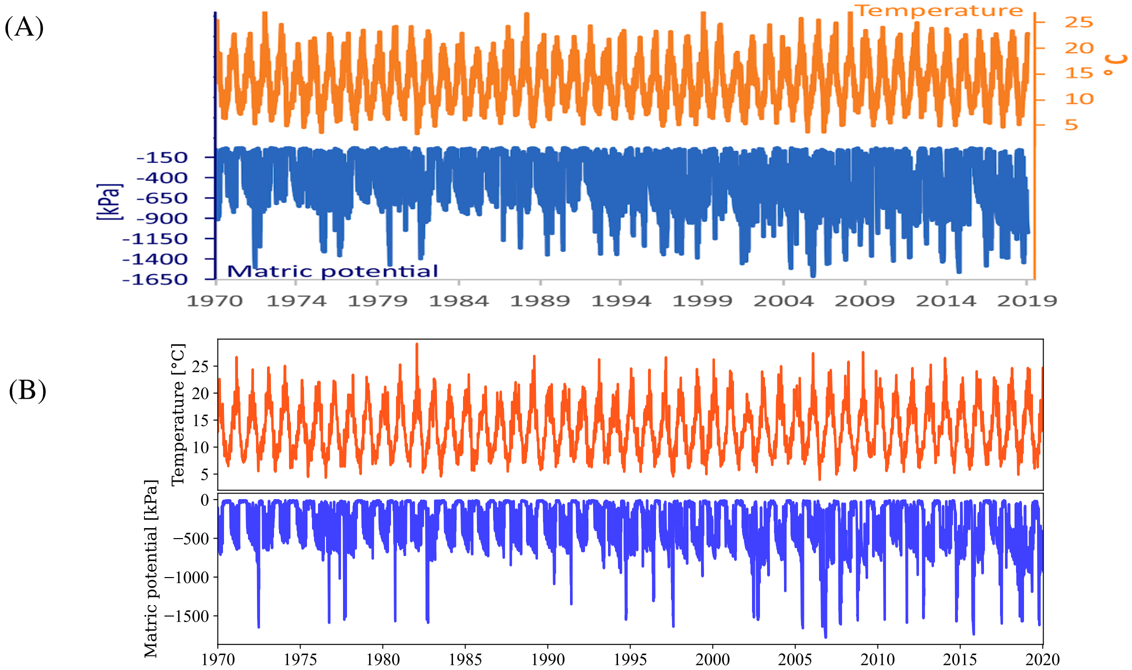

FIGURE 6.3: (A) Temperature [°C] from Wallis et al. (2022), used as a model input from the weather station located at the field site, and matric potential [kPa] at 50 mm depth as a model output. (B) Same parameters for the reproduced model, but with temperature measured at the RAAF Base Edinburgh in Adelaide.

6.2.3 Groundwater recharge

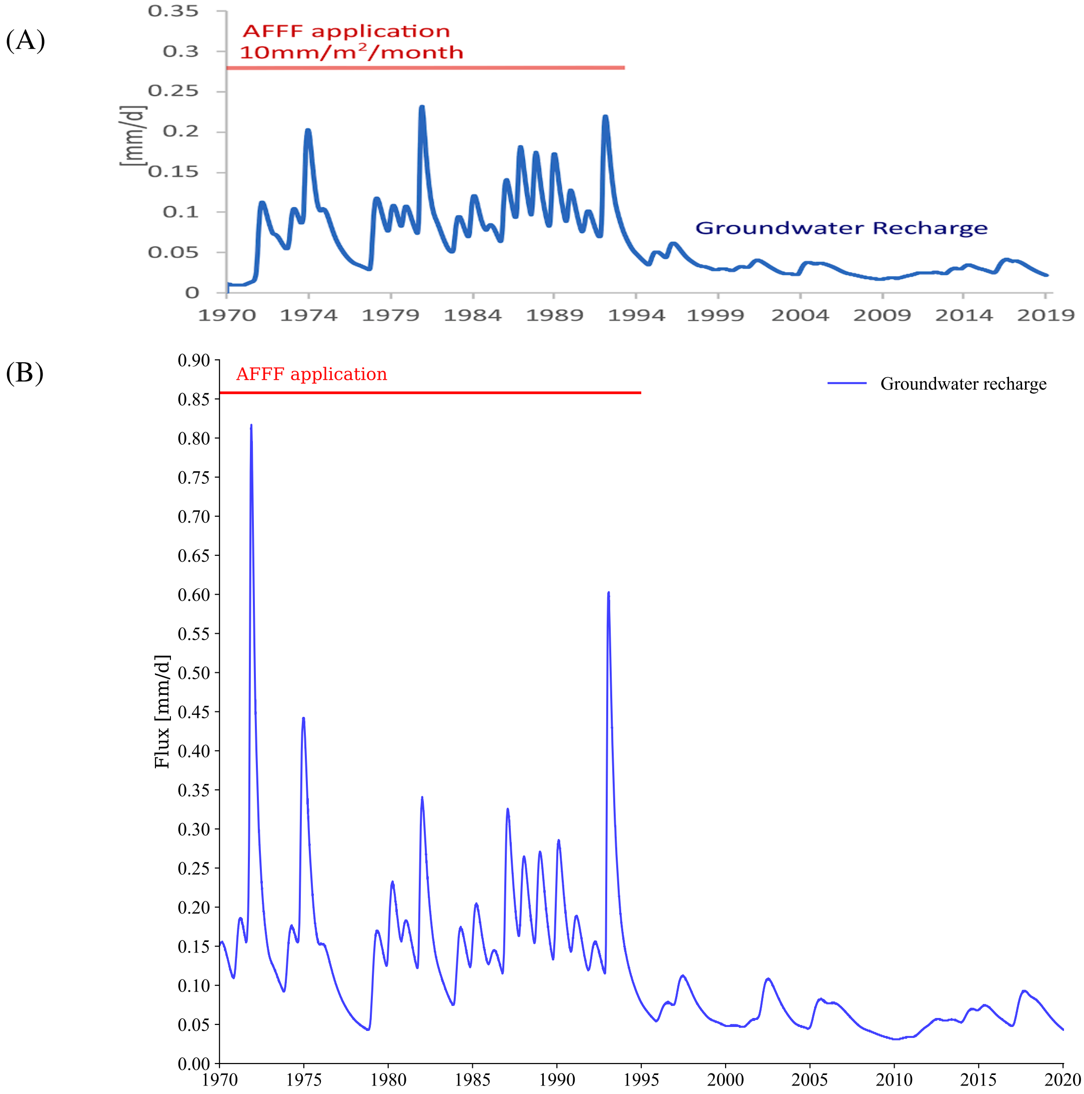

FIGURE 6.4: (A) Groundwater recharge [mm/d] from Wallis et al. (2022), as a model output. The long-term average groundwater recharge is 9.8 mm/y, representing $\sim$ 5% of the recorded rainfall during the simulation period, based on the weather data, soil characteristics, and plant cover. Recharge is slightly higher from 1970 to 1995, when fire-fighting training provided additional infiltration to the soil profile. (B) Reproduced model showing the same parameter, with a long-term average groundwater recharge of 46.08 mm/y, corresponding to $\sim$ 9% of the recorded rainfall during the simulation period.

6.2.4 Discussion

The FIGURES 6.2, 6.3 and 6.4 presented above indicate that the meteorological dataset used to reproduce the model of Wallis et al. (2022) is very similar, if not identical, to the one used in the original study. Indeed, when comparing the overall shape of each curve, variations occur at the same times, with maxima and minima observed during the same periods.

However, the water flux in the modelled subsurface does not appear to behave in the same way between the reproduced model and the original model of Wallis et al. (2022). As shown in FIGURE 6.2, the original model tends to exhibit runoff events more frequently and with higher magnitudes. For instance, the reproduced model shows only one instance where runoff exceeded 50 mm/d, whereas the original model presents three such events. Logically, this suggests that infiltration is greater in the reproduced model than in the original model of Wallis et al. (2022). Furthermore, FIGURE 6.4 clearly indicates that the amount of water leached to the groundwater is significantly higher in the reproduced model than in the original.

Regarding FIGURE 6.3, it is difficult to objectively compare the matric potential curves given their similarity. However, the lower matric potential values suggest that the top 5 centimetres of soil in the reproduced model indeed have a higher water content than in the original model. Concerning the evolution of surface soil temperature, as it is an input parameter, it is not influenced by water behaviour within the soil and only provides an indication of the similarity between the two meteorological datasets used. However, it is also difficult to be fully objective about temperature variations, although it can be confirmed that they fluctuate within the same range.

6.3 Comparison with Wallis (2022) PFAS leaching

This third section evaluates whether PFAS leaching in the reproduced model is consistent with the results reported by Wallis et al. (2022), and whether the same observations and conclusions can be drawn. First, PFAS concentration profiles are compared in relation to the site lithology (FIGURE 6.5). Next, the influence of evapotranspiration on PFAS concentrations in the very shallow soil (top 100 mm) is examined (FIGURE 6.6). Wallis et al. (2022) study showed that under Australian climatic conditions, evaporation causes the soil to act as a reservoir; this feature is likewise verified here (FIGURE 6.7). Finally, potential reasons for any discrepancies between the reproduced results and those reported in Wallis et al. (2022) are discussed.

6.3.1 PFAS concentration profile

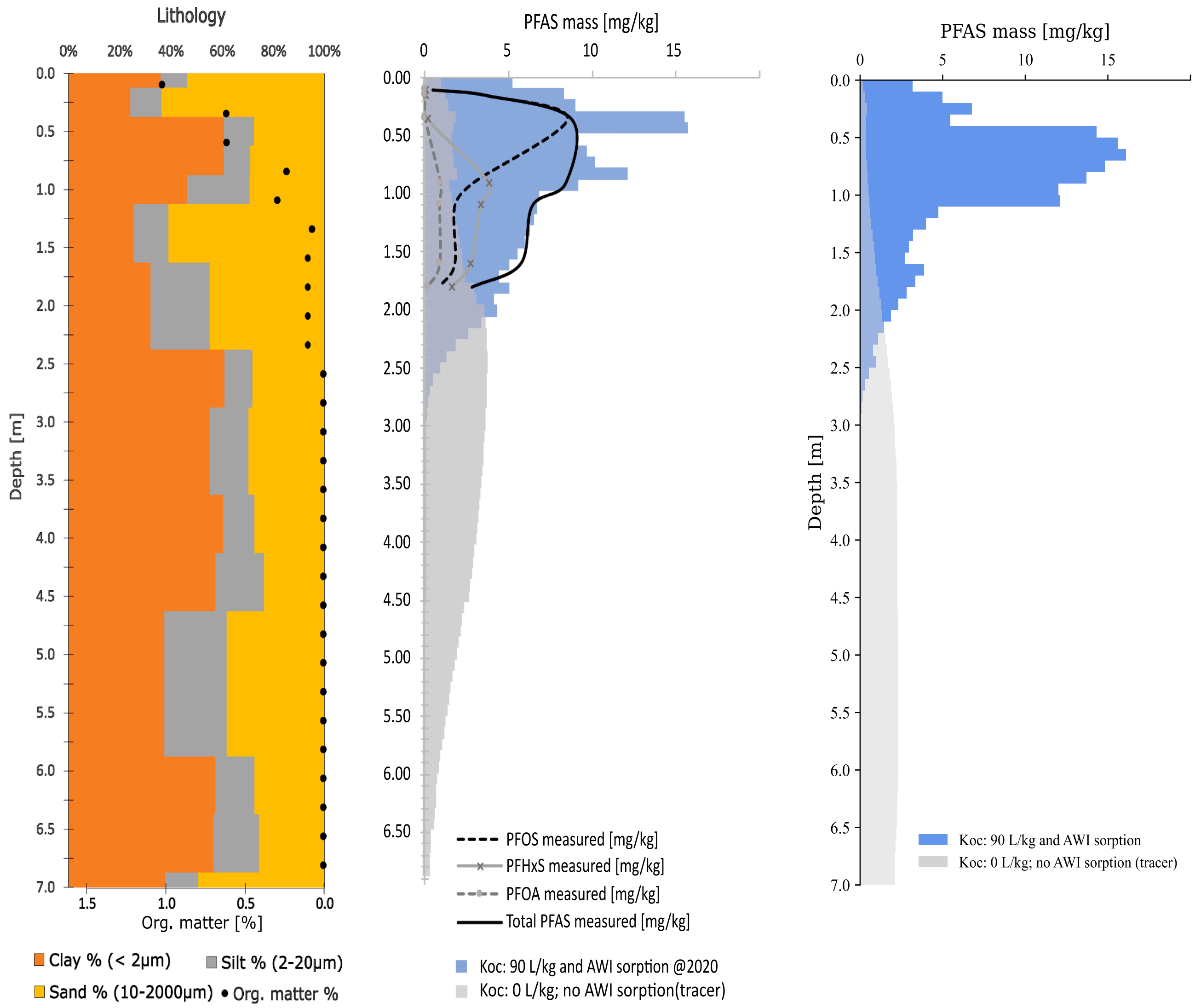

FIGURE 6.5: (Left) Profiles from Wallis et al. (2022): (1)soil lithology and organic-matter content, and (2) measured PFOS, PFHxS, and total PFAS [mg/kg], as well as simulated and calibrated total PFAS (blue bars) at 31/12/2019 [mg/kg]. For comparison, the theoretical distribution of a simulated tracer is also shown (grey bars). (Right) Simulated and calibrated total PFAS (blue bars) at 31/12/2019 [mg/kg] from the reproduced model. For comparison, the theoretical distribution of a simulated tracer is also shown (grey bars).

6.3.2 Evapo-concentration: key process for retaining PFAS mass in shallow horizons

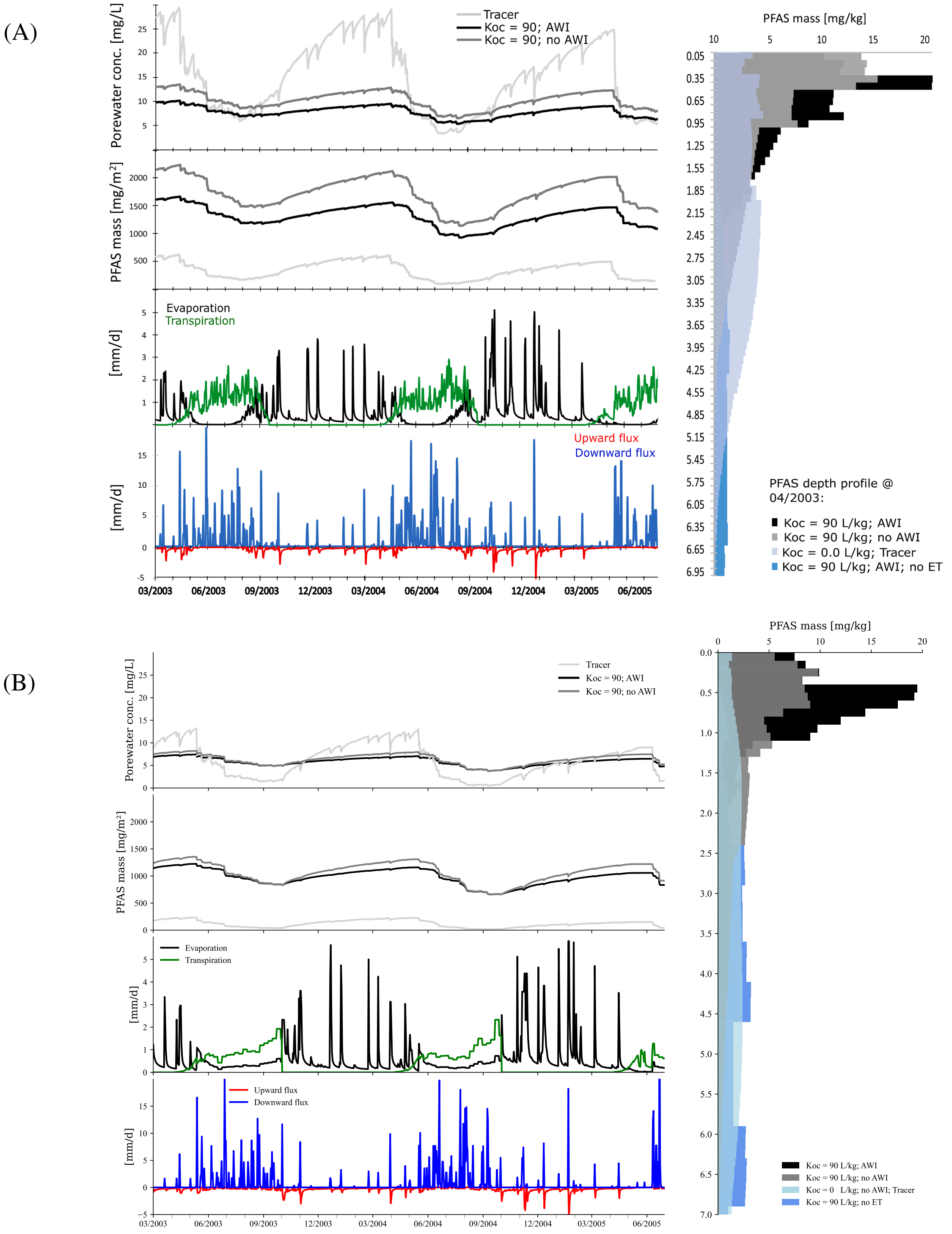

FIGURE 6.6: (A) From Wallis et al. (2022), porewater concentrations [mg/L] and mass [mg/m²] from 0 to 100 mm depth for a tracer (Koc = 0; light grey) and total PFAS. The latter is simulated with sorption (black line) and without sorption (grey line) to the air-water interface (AWI) to illustrate its effect. A selected PFAS depth profile for April 2003 (start of simulation period) is shown for the calibrated model (sediment and AWI sorption; black bars), for a model scenario with sediment sorption but without AWI retention (dark grey bars), for a tracer (light blue bars), and against a theoretical depth profile if evapotranspiration was not considered (sediment and AWI sorption; no ET; blue bars). (B) Reproduced model showing the same parameters.

6.3.3 Time-integrated field scale PFAS retardation

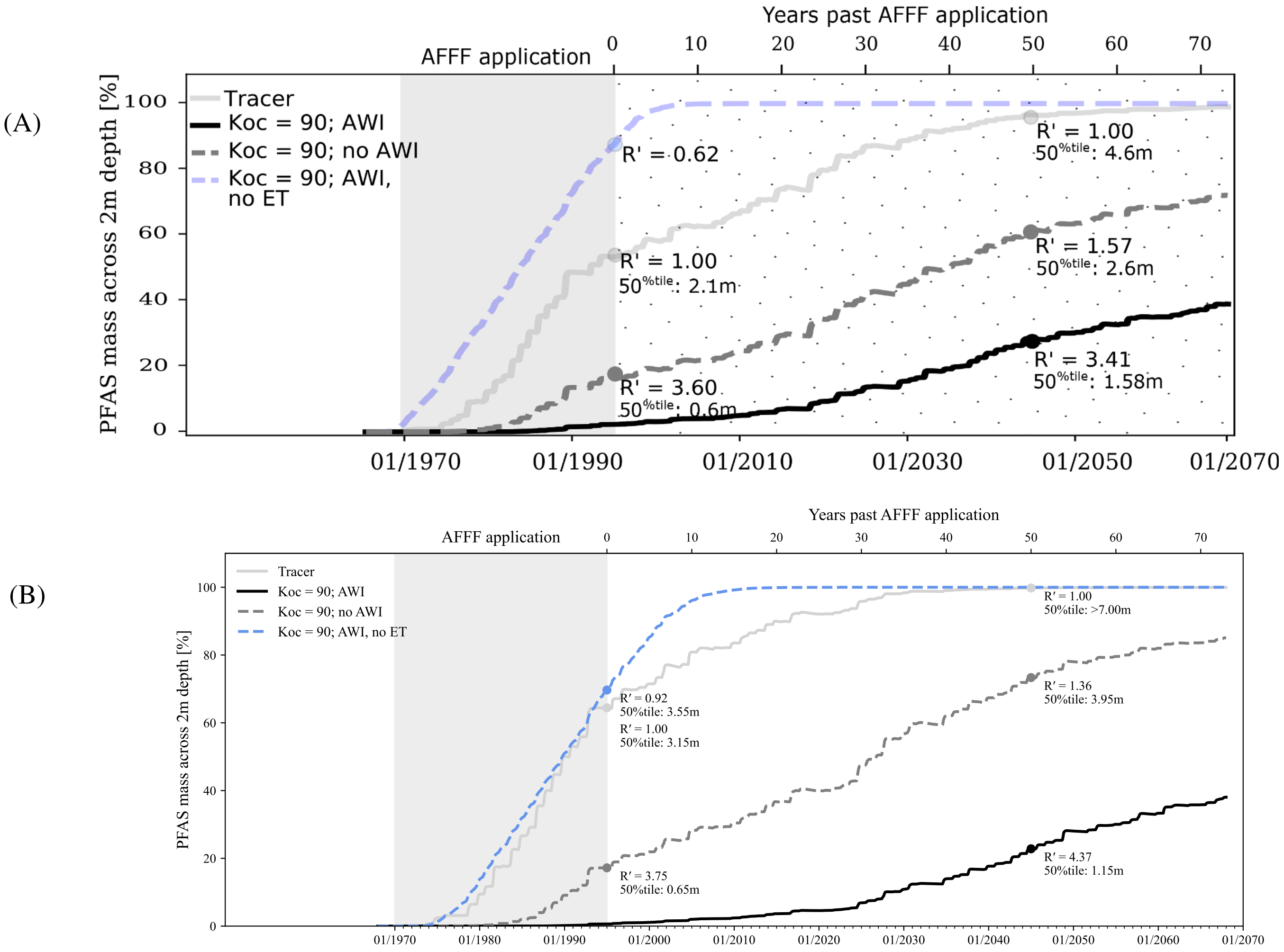

FIGURE 6.7: (A) From Wallis et al. (2022), cumulative flux of PFAS mass moving beyond the shallow soil horizon (across 2 m depth) as a % of total applied PFAS. Model scenarios are compared to the mass over time of a tracer, moving at the rate of the infiltrating water (R = 1, light grey line). Time-integrated retardation coefficients are calculated on the basis of the differing mass between PFAS and tracer (R'= $\text{mass}_{\text{tracer}}/\text{mass}_{\text{PFAS}}$). These are plotted at the end of the 3M Light Water$^{\text{TM}}$ application period (1995) and 50 years thereafter (2045), together with the depth of the 50% tile of PFAS mass. (B) Reproduced model showing the same parameters. In this simulation, the model run time was extended to 100 years by duplicating the climatic record and applying it from 01/01/2024 to 31/12/2067.

6.3.4 Discussion

FIGURE 6.5 shows that the total PFAS concentration profile 50 years after the first AFFF application in the reproduced model is relatively similar to that of the model by Wallis et al. (2022), as the parameters of the water retention curve were calibrated to match the profile illustrated in their study. However, PFAS concentrations appear lower within the top 100 millimetres of soil but higher between 0.5 and 1 metre in the subsurface, coinciding with the presence of a significant clay layer.

In contrast, FIGURE 6.6 provides several insights:

1. It shows clear similarities in the variations and the occurrence of maxima and minima across the curves, even though the illustrated period is much shorter ($\sim$ 2 years). This is particularly visible in the evaporation and transpiration curves at the soil surface, as well as the upward and downward fluxes within the top 100 millimetres, confirming that the meteorological datasets are highly similar.
2. Water fluxes (light grey tracer curve) in the top 100 mm differ between the models, with the reproduced one showing lower tracer concentrations in both porewater and total mass. Based on FIGURE 6.3 (matric potential), this suggests that water is less retained and more readily drained in the upper metres. Considering FIGURE 6.4 (groundwater recharge) and the tracer depth profiles in this figure (2003) and in FIGURE 6.5 (2020), this pattern likely applies to the entire profile.
3. The curves of total PFAS mass and porewater PFAS concentration, with or without AWI, also show lower values than in the original model, indicating greater leaching in the reproduced one within the top 100 mm. However, it is not possible to conclude that PFAS leaching is faster in the reproduced model, given the similar pattern observed in the depth profile 50 years after the first AFFF application (2020).
4. PFAS and tracer concentrations 33 years after the first AFFF releases (2003) show, as in Wallis et al. (2022), that PFAS retention in surface soil is primarily driven by evapotranspiration.
5. Overall, this graph helps assess whether the observations and hypotheses in Wallis et al. (2022) apply to the reproduced model. Although porewater and total PFAS concentrations are lower due to greater leaching, the effects of evapotranspiration and sorption on PFAS retention over time and with depth remain evident. As in Wallis et al. (2022), decreases in PFAS concentration and mass coincide with rain events and downward flux, while evapotranspiration allows prolonged upward flow and PFAS retention in shallow horizons.

FIGURE 6.7 also compares the validity of the reproduced model with the original. Water mass (light grey tracer curve) is leached more rapidly from the top 2 metres of soil in the reproduced model: in 1995 (25 years after the first AFFF and tracer releases), the median tracer mass depth was 3.15 m compared with 2.1 m in Wallis et al. (2022), and by 2045, 99.8% of the tracer mass had left the first 2 metres compared with 95% in the Wallis model.

Despite faster water leaching, total PFAS mass is more strongly retained in the reproduced model. In 2045, 50% of PFAS mass was predicted at 1.15 m depth versus 1.58 m in the Wallis model, raising the question of which factor increases retention.

- Evapotranspiration is not the cause: even without it, PFAS retention in the top 2 metres is higher in the reproduced model (36% retained by 1995) than in the Wallis et al. (2022) model (25%).
- Without AWI, PFAS leaching is greater in the reproduced model, with deeper median PFAS mass depths in both 1995 and 2045. This indicates stronger AWI-related retention in the reproduced model, likely due to differences between the two models (SECTION 6.3.5).

The time-integrated retardation factors in FIGURE 6.7 cannot be compared because the tracer reference curves differ between the 2 models.

6.3.5 Potential sources of model discrepancies

The potential reasons for (i) differences in infiltration, (ii) altered water fluxes with enhanced drainage in the vadose zone, (iii) increased PFAS leaching in the upper centimetres of soil, and (iv) greater PFAS retention at depth are set out below:

1. Weather:
   As mentioned earlier, the information available regarding the site studied by Wallis et al. (2022) is limited. It is therefore not certain that the site corresponds precisely to the RAAF Base Edinburgh in Adelaide, and it is possible that the meteorological dataset used differs slightly.

2. Soil granulometry and TOC
   The soil granulometry and total organic carbon (TOC) at each node in the model were defined based on FIGURE 6.1 from the study by Wallis et al. (2022), and therefore do not correspond to exact measurements.

3. Water retention curve:
   Manually calibrating five parameters influencing the soil water retention curve is a complex task, especially given the difficulty in understanding their individual effects on the curve. The calibration effort was considered sufficient for the purposes of this study, although a more accurate estimation of these parameters would certainly have been possible. The lack of specific information regarding these parameters likely represents the greatest source of uncertainty in the reproduced model, and has a significant influence on the results obtained.

4. Surface crust:
   The presence of a potential surface crust limiting the conductivity at the soil surface could potentially explain the differences observed in infiltration and runoff between the two models. This would be plausible given that the modelled soil profile is representative of that of an airport. However, this was not implemented in the reproduced model, as no information on this aspect is provided in the paper by Wallis et al. (2022).

6.4 Conclusion of the chapter

Although some differences remain, the reproduced model successfully captures the principal trends reported by Wallis et al. (2022). Consequently, PFAS transport under Australian climatic conditions is well represented and internally consistent.

Chapter 7

Study of PFAS leaching in temperate conditions

7.1 Climatic Adjustment for Belgian Conditions

In order to represent a typical Belgian climate, a meteorological dataset from the website Royal Meteorological Institute of Belgium (RMI) (2025) is used. The gridded observational dataset published by the Royal Meteorological Institute of Belgium (RMI) provides spatially interpolated meteorological data over the entire Belgian territory. The dataset is constructed using measurements from a network of meteorological stations, which are then processed to estimate values on a regular 5 km × 5 km grid covering the country.

This interpolation ensures that meteorological variables are available even in areas without direct instrumentation. Each variable is provided at various temporal resolutions (daily, monthly, seasonal, annual), and long-term climatological averages are also available. The database begins in 1961 for most variables and is updated daily, with quality control applied as soon as new observations are ingested.

Australian weather inputs in the model (precipitation, temperature, and potential evapotranspiration) were replaced with long-term daily climate data representative of Belgian conditions. This substitution enables the simulation of identical soil and contamination scenarios under a wetter regime, characterised by increased rainfall and reduced evaporative demand.

Since the site investigated in Wallis et al. (2022) is probably an airport, the estimated meteorological data for the 5 × 5 km grid cell centred on Bierset Airport, west of Liège, were used (see APPENDIX D). In addition, the geology at this site is relatively similar to that of the study site, as soils in the Hesbaye region consist mainly of silt in the upper horizons.

The only missing variable in the Belgian dataset was the reference evapotranspiration (EV_0) before 1984. Fortunately, LEACHM is able to estimate this value using the Linacre equation (Hutson, 2003), a simplified empirical method based on temperature, altitude, and latitude.

In addition, vegetation type and root water uptake can significantly influence the soil moisture regime and may also retain PFAS through bioaccumulation. Consequently, vegetation can have a non-negligible impact on PFAS leaching in the topsoil. As the seasons are the opposite between Belgium and Australia, the growth period of vegetation would, in principle, need to be seasonally shifted in the model. However, in practice, the timing of grass growth appears to be similar in both regions. In southern Australia, Wallis et al. (2022) specifies that grass cover growth starts in April, peaks at the end of June, and ceases in October. This matches the typical growth pattern of temperate grass in Belgium, which begins in March or April, reaches maximum cover around

June or July, and ends in October when temperatures drop. Therefore, despite the hemispheric difference, the vegetation growth parameters from the Australian context can be retained without modification. However, some vegetation parameters are, of course, different, as the climate in Belgium is generally wetter. These differences are not considered in the present modelling. For example, the size and density of the grass cover are likely to be more developed in Belgium, which would have an influence on evapotranspiration and root water uptake.

7.2 Comparison between Australian and Belgian conditions

This section compares the influence of climate adjustment on physical water-flow processes. Since these processes are strongly climate-driven, three aspects are examined across the two models: (i) infiltrating rainfall and surface runoff (FIGURE 7.1), (ii) soil-surface temperature and matric potential within the top 100 millimetres (FIGURE 7.2), and (iii) groundwater recharge (FIGURE 7.3). These results are first presented through three figures and then discussed in detail.

7.2.1 Rainfall and runoff

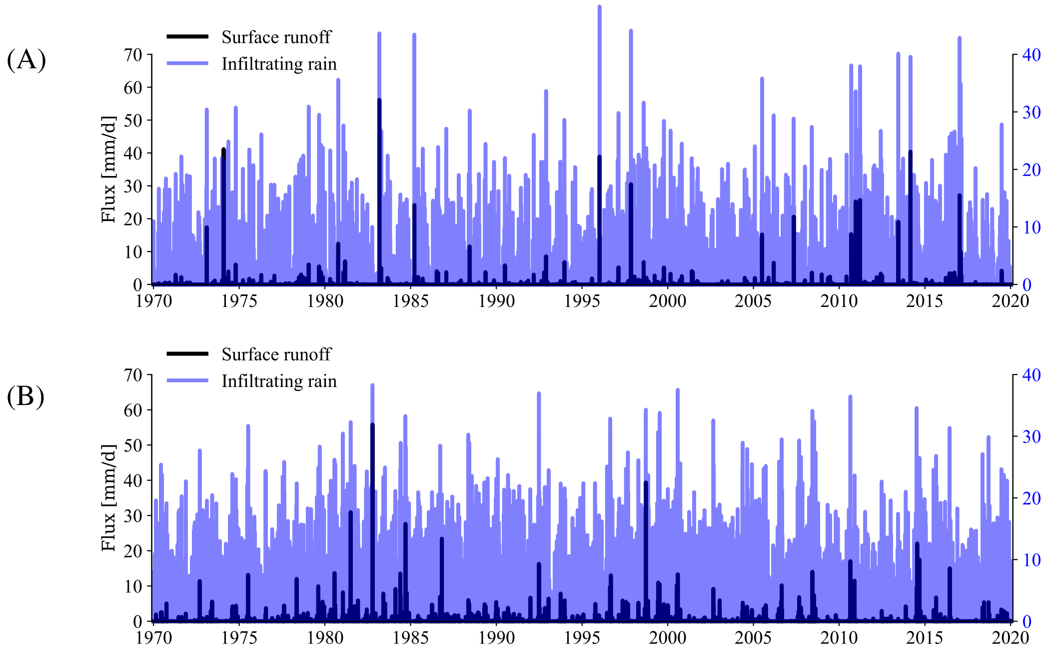

FIGURE 7.1: Daily infiltrating rainfall and surface runoff [mm/d] in the reproduced model under Australian (A) and Belgian (B) weather conditions. The long-term average infiltrating rainfall is 415.0 mm/y in Australia and 780.2 mm/y in Belgium, with corresponding long-term average runoff values of 18.07 mm/y and 30.12 mm/y, respectively.

7.2.2 Temperature and matric potential

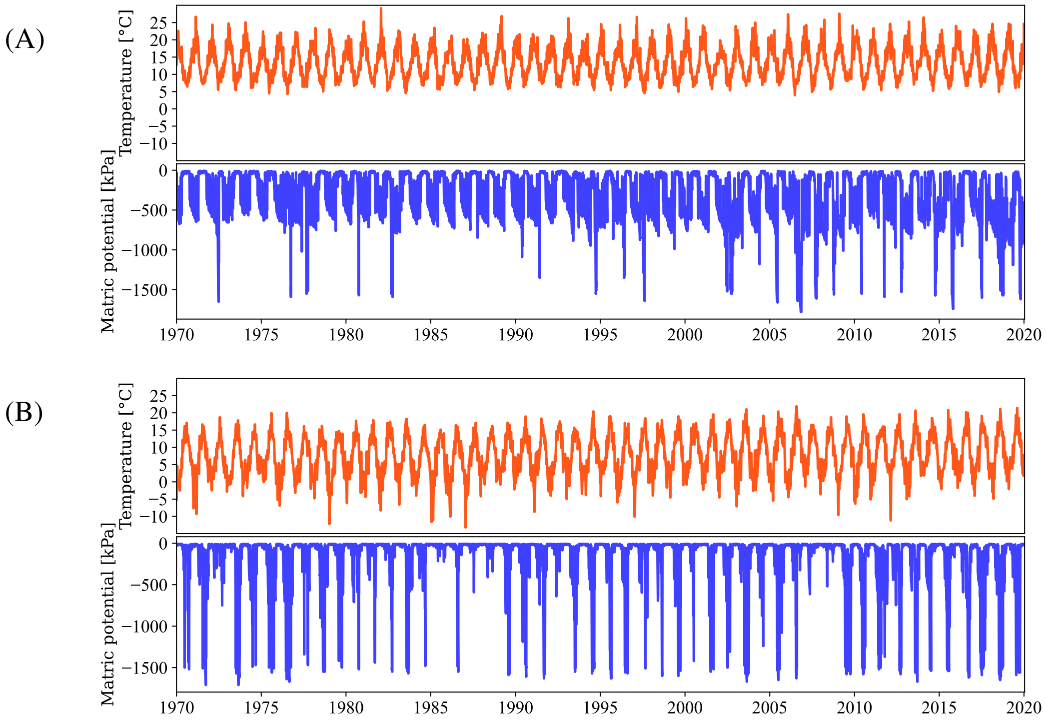

FIGURE 7.2: Temperatures used as model inputs from the weather stations located at RAAF Base Edinburgh in Adelaide (A) and at Bierset Airport in Liège (B). The matric potentials [kPa] are simulated for the top 50 mm of the soil profile, with average matric potential values of -376 kPa in Australia and -184 kPa in Belgium.

7.2.3 Groundwater recharge

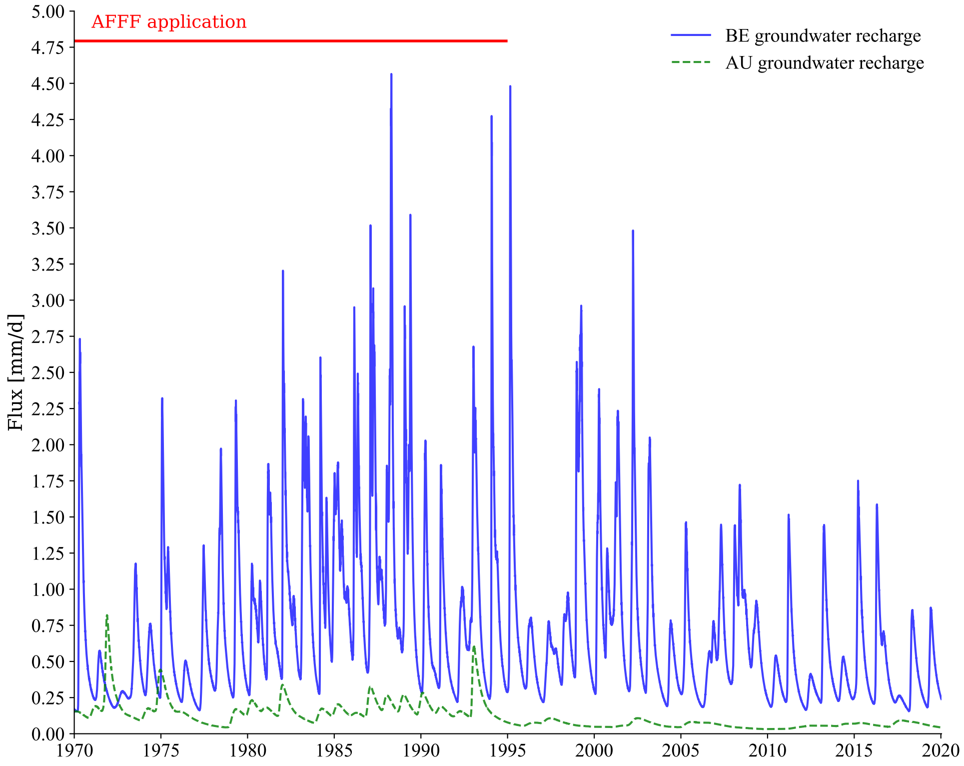

FIGURE 7.3: Groundwater recharge [mm/d] as model output from the reproduced simulation. The green curve represents the model run under Australian weather conditions, with a long-term average groundwater recharge of 46.08 mm/y, corresponding to only $\sim$ 9% of the recorded rainfall during the simulation period. The blue curve corresponds to the simulation using Belgian weather data, with a long-term average of 264.93 mm/y, representing $\sim$ 30% of the recorded rainfall. Recharge is fractionally higher from 1970 to 1995, when fire-fighting training provided additional infiltration to the soil profile.

7.2.4 Discussion

FIGURES 7.1, 7.2 and 7.3 compare the two meteorological datasets, showing a transition from Mediterranean, hotter conditions to temperate, wetter conditions. FIGURE 7.1 highlights that Belgian rainfall is more regular, with annual infiltration almost twice that of Australia (780.2 mm/y vs 415.0 mm/y).

FIGURE 7.2 shows higher average temperatures in Australia, where evaporation accounts for 58% of rainfall losses compared to 37% in Belgium. Matric potential variability is greater in Belgium (0 to -1500 kPa), but Australia shows a lower average potential (-376 kPa in AU vs -184 kPa in BE), indicating stronger water retention in the top 50 mm of soil. However, plant transpiration losses are similar in both cases ($\sim 29\%$ of rainfall).

FIGURE 7.3 indicates that groundwater recharge is much higher in Belgium (264.93 mm/y, 30% of rainfall) than in Australia (46 mm/y, 9%), reflecting faster water transport in the Belgian profile.

Under Belgian meteorological conditions, water losses are relatively evenly distributed between drainage, evaporation, and transpiration. In contrast, in the Australian scenario they are dominated by evaporation, with a smaller contribution from transpiration. As a result, leaching through the vadose zone is much greater in Belgium, reaching almost six times the Australian value (264 mm/y vs 46 mm/y) and ultimately recharging the groundwater. In both cases, the remaining fraction of water loss is attributable to surface runoff.

7.3 Evaluation of changes in PFAS leaching

The adaptation of the model to Belgian meteorological conditions allows to evaluate the impact of local climatic conditions on the leaching potential of PFAS compounds in the vadose zone, as well as their influence on the retention-controlling parameters.

To evaluate how Belgian weather conditions influence PFAS leaching, the temporal evolution of concentration profiles for both PFAS and chloride is first compared (FIGURES 7.4 and 7.5). Then, to better identify where the main PFAS retention occurs in the soil, the cumulative mass in the two metres below ground level (bgl) and in the entire profile is examined (FIGURE 7.6). On the same graph, concentrations at the base of the soil profile are also shown, providing insight into how groundwater would be impacted under both conditions.

7.3.1 Evolution of tracer porewater concentration and masses in the soil profile

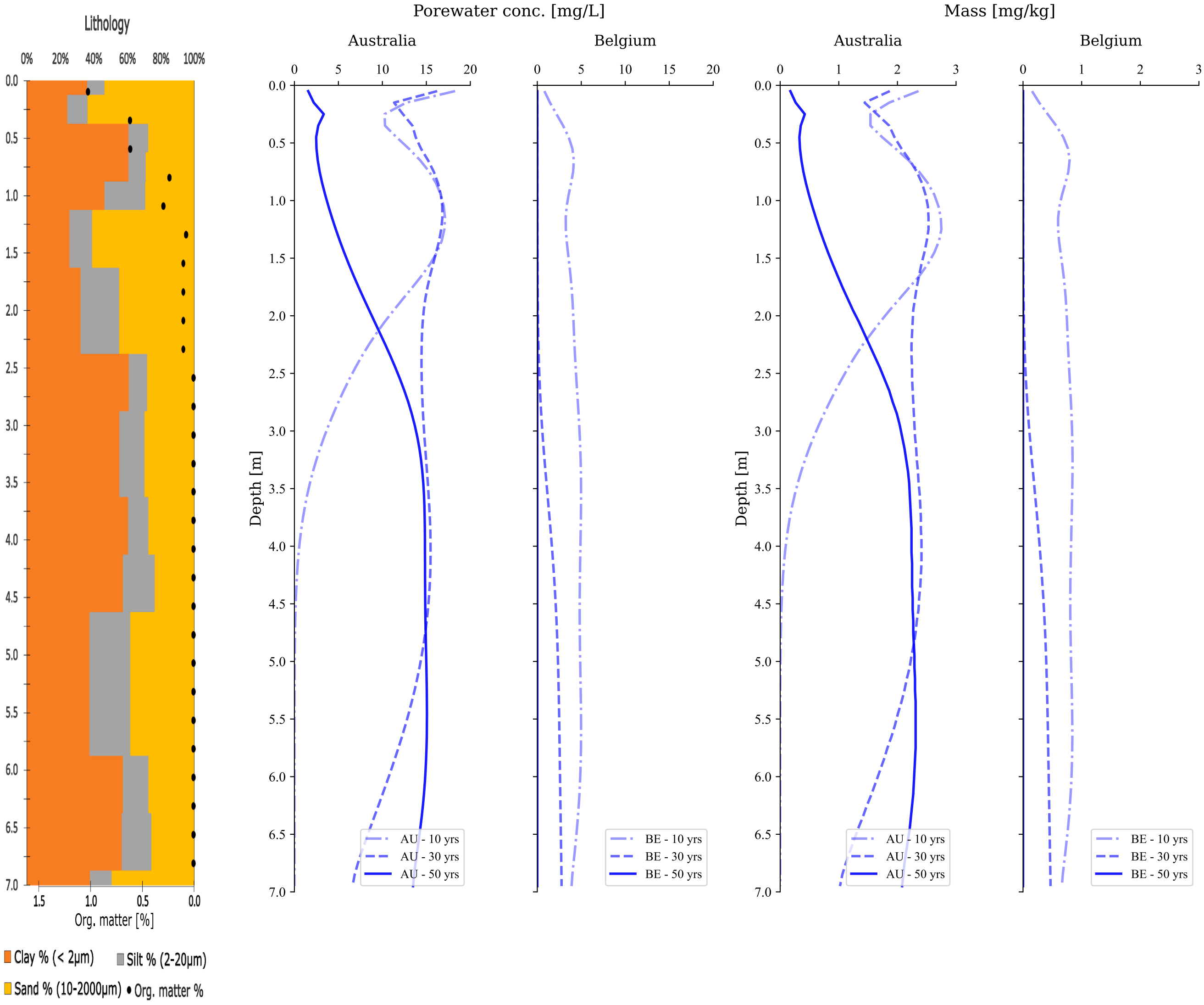

FIGURE 7.4: Soil lithology and organic-matter content profiles from Wallis et al. (2022), shown alongside simulated **tracer** (chloride) porewater concentrations and mass distributions with depth at three times (1980, 2000, 2020) from the reproduced model under Australian and Belgian weather conditions.

7.3.2 Evolution of PFAS porewater concentration and masses in the soil profile

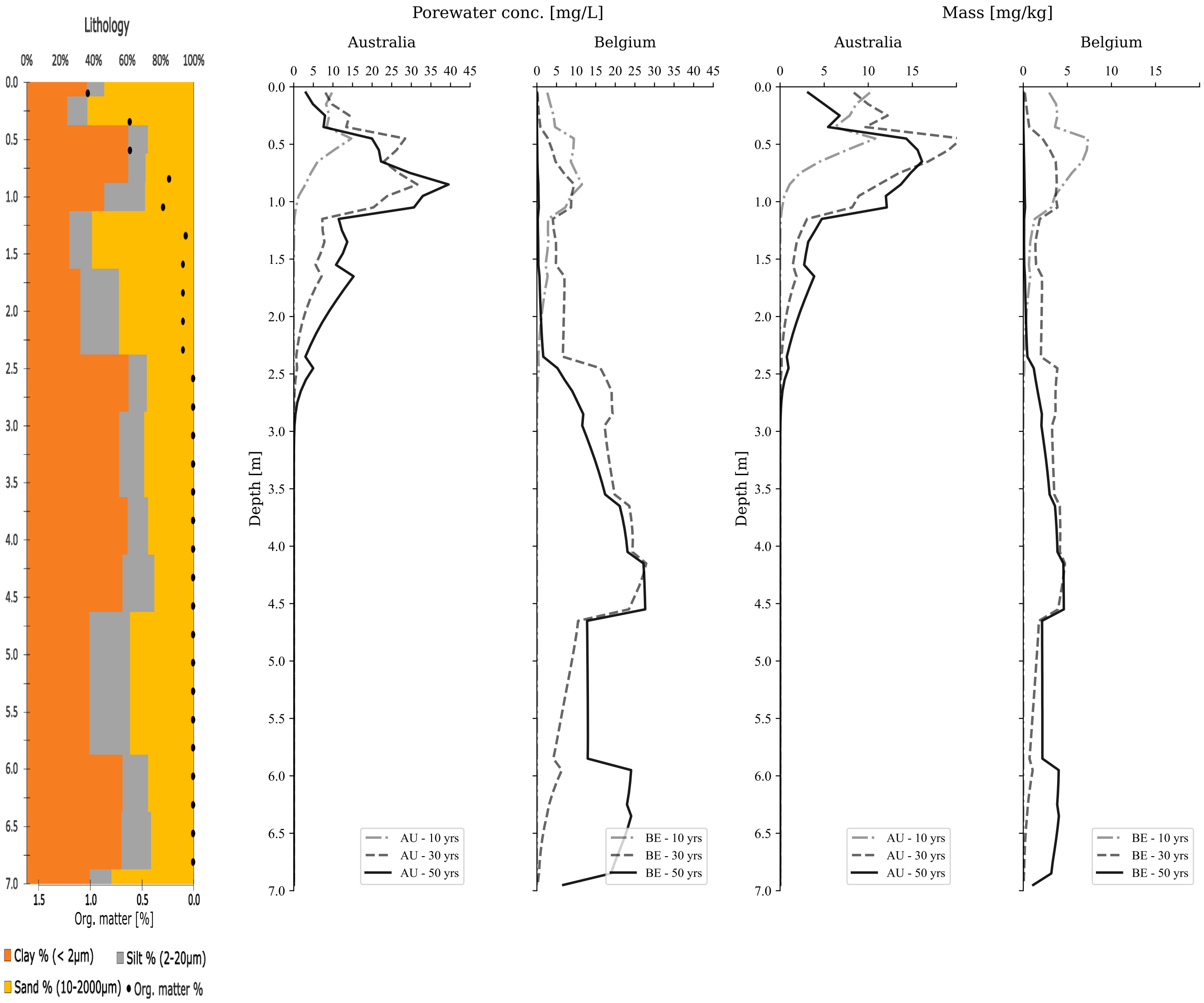

FIGURE 7.5: Soil lithology and organic-matter content profiles from Wallis et al. (2022), shown alongside simulated **PFAS** porewater concentrations and cumulative mass distributions with depth at three times (1980, 2000, 2020) from the reproduced model under Australian and Belgian weather conditions.

7.3.3 Cumulative mass in the top two metres and in the entire profile, and concentrations at the base of the soil profile

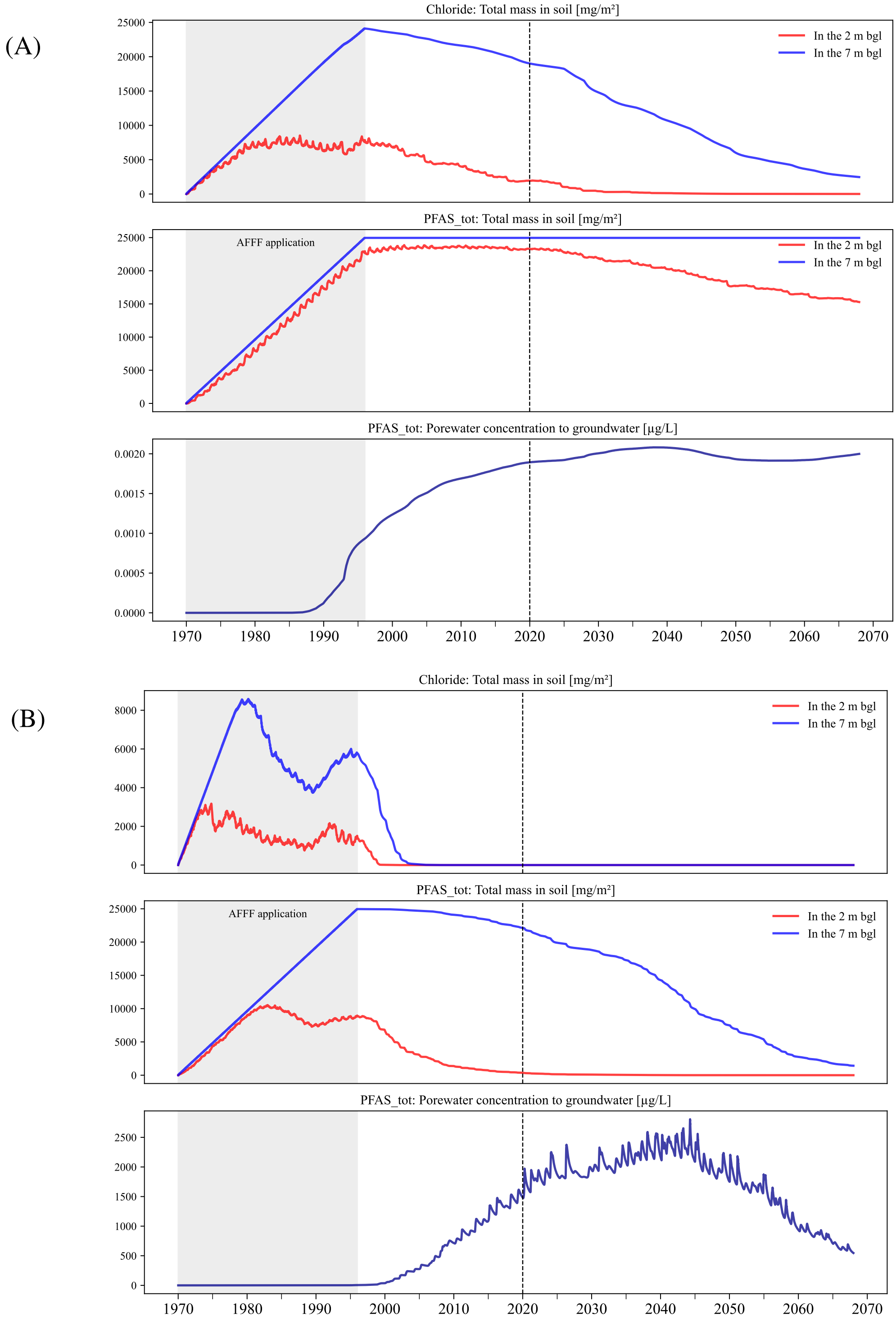

FIGURE 7.6: Simulated chloride and PFAS leaching following the first AFFF release at the soil surface. For each case, the temporal evolution is shown for the cumulative mass in the top two metres and in the entire profile (7 m), together with PFAS porewater concentrations at the base of the profile. The total amount of PFAS and chloride injected at the soil surface by the end of 1995 is 24.960 g/m^2. Results are presented for (A) Australian and (B) Belgian weather conditions. In this simulation, the model run time is extended to 100 years by duplicating the climatic record and applying it from 01/01/2024 to 31/12/2067.

7.3.4 Discussion

FIGURE 7.4 first shows that water in the profile subjected to Belgian meteorological conditions is leached much more rapidly than under Australian conditions. These figures also indicate that both the total tracer mass and its porewater concentration evolve with the same depth distribution over time, which is expected since the **chloride tracer is fully conservative** and does not sorb to the solid matrix.

FIGURE 7.5 further highlights that, under wetter climatic conditions, PFAS are leached more rapidly. In comparison with FIGURE 7.4, it also reveals that PFAS mass behaves differently from the PFAS concentration in porewater. This is because **PFAS can partition** both to the air-water interface (AWI) and the solid-water interface. Unlike the tracer, part of the PFAS mass is therefore not present in the dissolved phase. In addition, precipitation onto the solid phase and partitioning into the gas phase are negligible here, given the high solubility of PFAS and their low K_H.

Under Australian conditions, the top two metres of soil appear to **act as a reservoir**. Most of the PFAS mass seems to be retained within the more clay-rich layer of the first metre of soil. In contrast, under Belgian conditions, leaching is much stronger and there is no clear evidence of enhanced PFAS retention in the shallow soil layers. However, similarly to the Australian case, PFAS concentrations still tend to be locally higher in the more **clay-rich** soil lenses (FIGURE 7.5).

FIGURE 7.6 provides insight into the **leaching rates** of both the tracer and PFAS, showing how long the total mass is retained within the profile before it begins to decrease. Furthermore, it also highlights the **influence of evapotranspiration** on the mass retained in the first two metres: while initial increases could reflect AFFF inputs, later rises after the application period also indicate the influence of upward water fluxes returning PFAS to this zone.

Regarding **water** leaching velocity in FIGURE 7.6, it took more than 17 years for a cumulative mass of 1 mg/m^2 of tracer to reach the groundwater in Australia, whereas in Belgium the same threshold was reached in less than 8 years. In Belgium, around 1975, the tracer mass in the soil declined despite continued surface inputs at the same frequency. This indicates **interannual variability** in leaching rates, with intensity appearing to fluctuate on a roughly five-year cycle. As shown in FIGURE 7.3, a particularly strong leaching event occurred around 1997; followed by a decline in flux, even though AFFF application was still ongoing. This could reflects a 5-year period of above-average rainfall combined with reduced evapotranspiration.

FIGURE 7.6A shows that, under Australian conditions, no PFAS mass leaches beyond the 7 m soil profile even 98 years after the first injection. About 93% of the mass remains in the top two metres after 50 years, and around 61% after 100 years. The upper two metres therefore act as a **reservoir** that gradually releases PFAS under Australian climatic conditions. This behaviour is **favourable**, since the total PFAS concentration reaching groundwater never exceeds 0.1μg/L, in compliance with both Walloon and Australian standards, the latter being $0.07\mu g_{\text{PFOS+PFHxS}}/\text{L}$ (a relevant comparison, as the pollutant mass mainly reflects PFOS properties) (see SECTION B).

In contrast, under Belgian conditions, only about 2% of the injected mass remains in the top two metres after 50 years, while nearly 10% has already leached out of the profile. By 98 years after the first injection, around 94% of the mass has left the 7 m profile. PFAS are therefore leached much more rapidly. Furthermore, FIGURE 7.6B also shows variations in **PFAS** leaching rates associated with **interannual climatic fluctuations** during the period of AFFF application.

7.4 Influence of evapotranspiration and AWI on PFAS transport

This chapter analyses which processes exert the greatest influence on PFAS transport in the vadose zone, with particular emphasis on evapotranspiration (ET) and air-water interfacial (AWI) retention.

As in Wallis et al. (2022), the first step is to examine whether evapotranspiration affects PFAS leaching within the top 100 mm of soil. A time period between 1996 and 1998 is considered, as under Belgian conditions leaching is sufficiently rapid that, by 2003-2005 (five years after the cessation of AFFF application), almost no PFAS remain in the upper soil and comparison with the Australian case is no longer possible (FIGURE 7.7). In addition, PFAS concentration variations are compared with and without ET and AWI to evaluate their respective roles over time (FIGURE 7.8).

Subsequently, the influence of these two factors is assessed over the top two metres of the profile by tracking the temporal evolution of cumulative PFAS mass, normalised to the maximum injected mass in this zone, with and without ET and AWI (FIGURE 7.9).

Finally, their influence is evaluated across the entire profile by comparing the depth evolution of PFAS plumes at two different times, again with and without these processes accounted for (FIGURE 7.10).

7.4.1 Shallow soil retention under contrasting climates

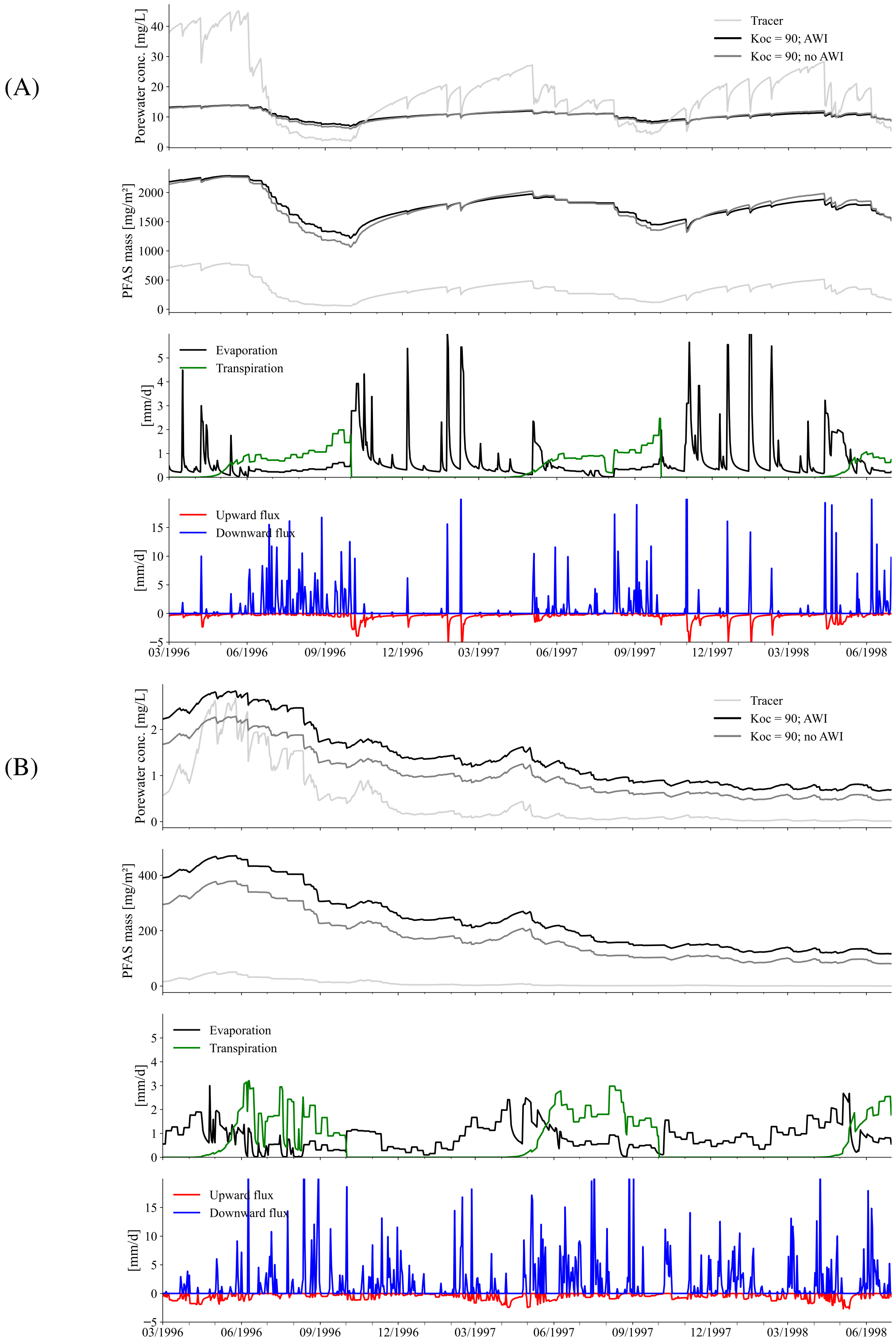

FIGURE 7.7: (A) Mass [mg/m²] from 0 to 100 mm depths for a tracer (Koc = 0; light grey) and total PFAS under Australian (A) and Belgian (B) weather conditions. The latter is simulated with sorption (black line) and without sorption (grey line) to the air-water-interface (AWI) to illustrate its effect. Periods of decreasing PFAS concentration and mass coincide with rain events and downward flux. Evapotranspiration allows for substantial periods of upward flow.

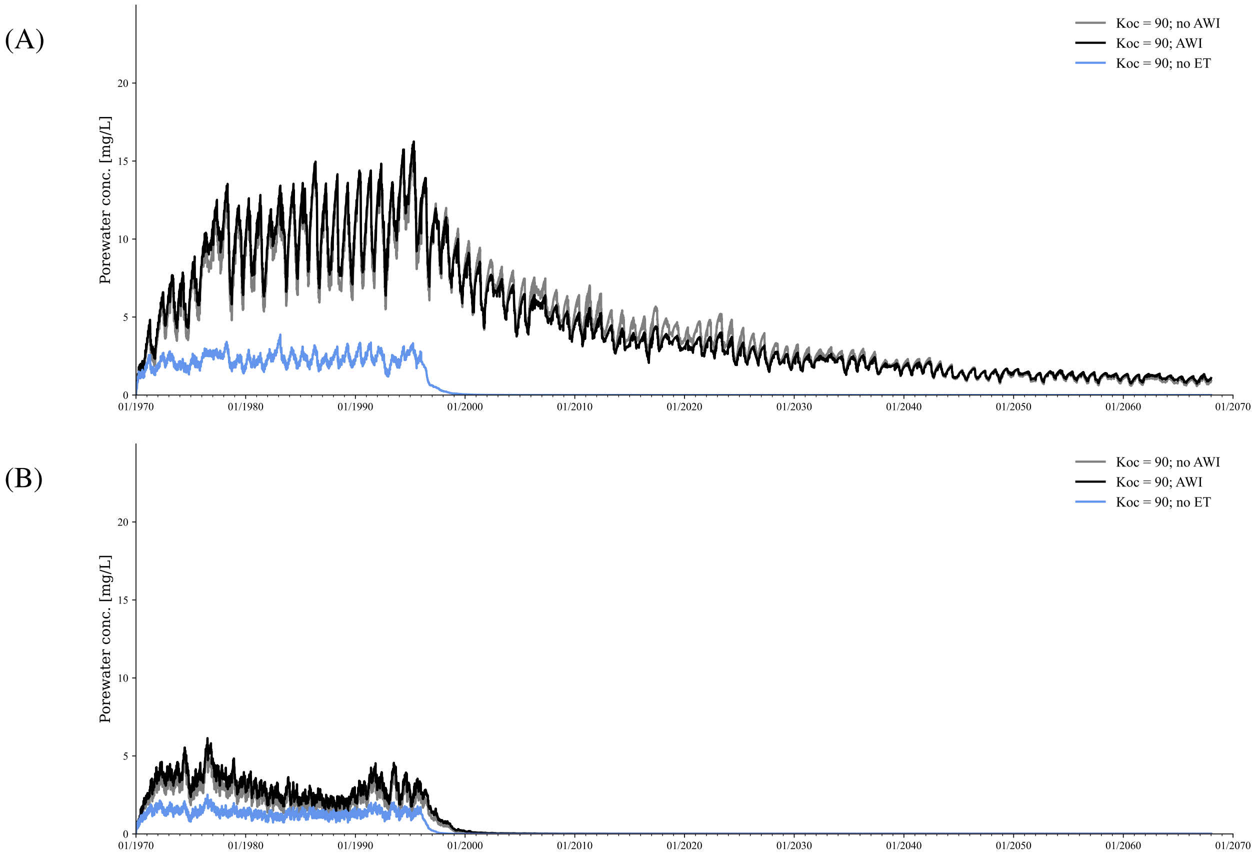

FIGURE 7.8: Simulated dissolved porewater concentrations of PFAS [mg/L] within the upper 100 mm of the soil profile under Australian (A) and Belgian (B) weather conditions. Concentrations are shown for the calibrated model (Koc = 90; AWI) (black line) as well as theoretical PFAS concentrations if air-water interface (AWI) sorption was negligible (grey line). For comparison, theoretical PFAS concentrations are also shown if evapotranspiration was negligible (light blue line). Rapid changes in concentration are caused by evapo-concentration during periods of ET > rain (summer), while dilution occurs during periods of rain > ET (winter). In this simulation, the model run time was extended to 100 years by duplicating the climatic record and applying it from 01/01/2024 to 31/12/2067.

7.4.2 PFAS retention within the top two metres of soil

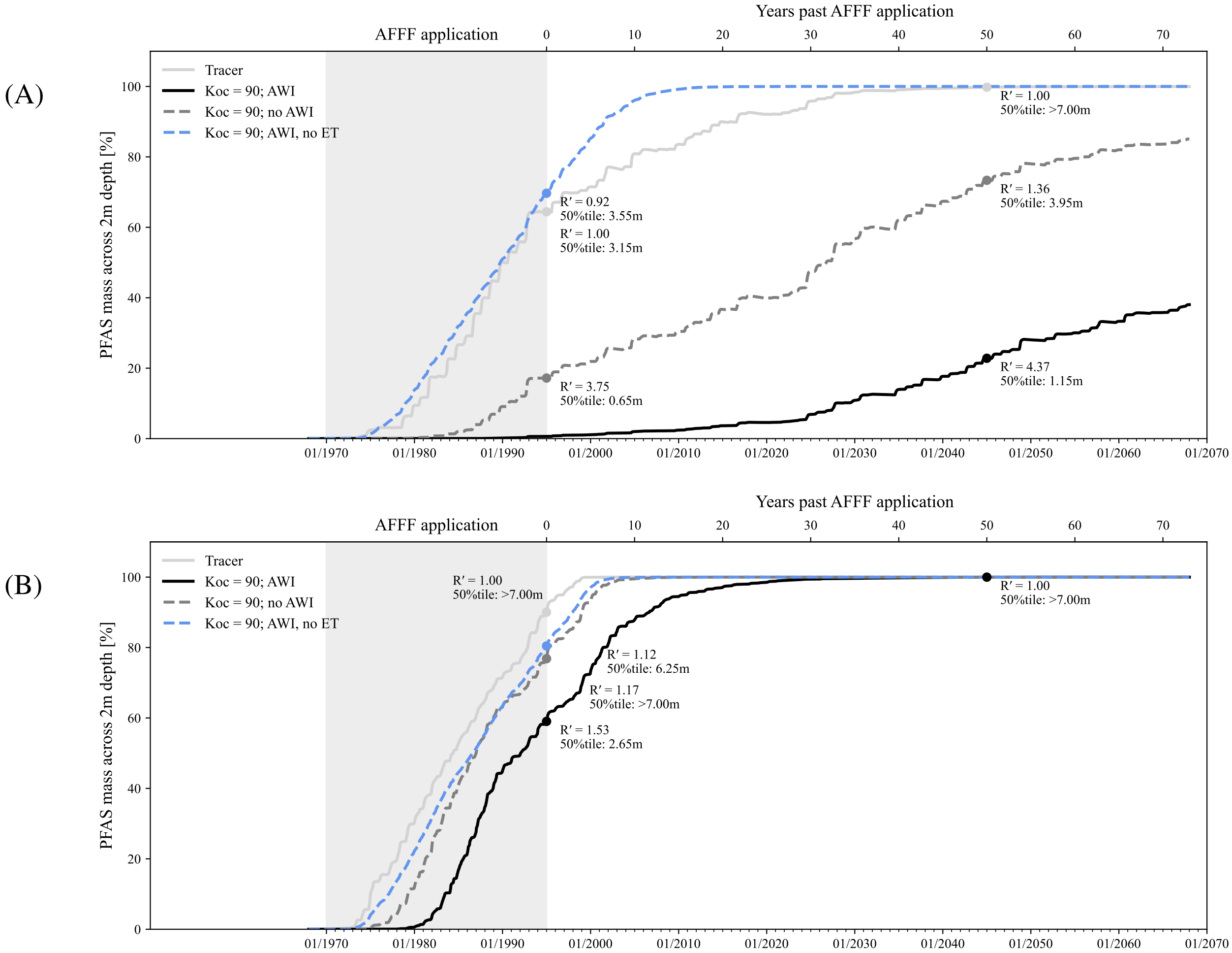

FIGURE 7.9: Cumulative flux of PFAS mass moving beyond the shallow soil horizon (across 2 m depth) as a % of total applied PFAS. Model scenarios are compared to the mass over time of a tracer, moving at the rate of the infiltrating water (R = 1, light grey line). Time-integrated retardation coefficients are calculated on the basis of the differing mass between PFAS and tracer (R'= $\mathrm{mass}_{\mathrm{tracer}}/\mathrm{mass}_{\mathrm{PFAS}}$). Plotted at the end of the 3M Light Water$^{\mathrm{TM}}$ thereafter (2045), together with the depth of the 50% tile of PFAS mass. The time-integrated retardation factors cannot be compared between the Australian (A) and Belgian conditions because the tracer reference curves differ between the 2 models.

7.4.3 PFAS distribution across the full soil profile

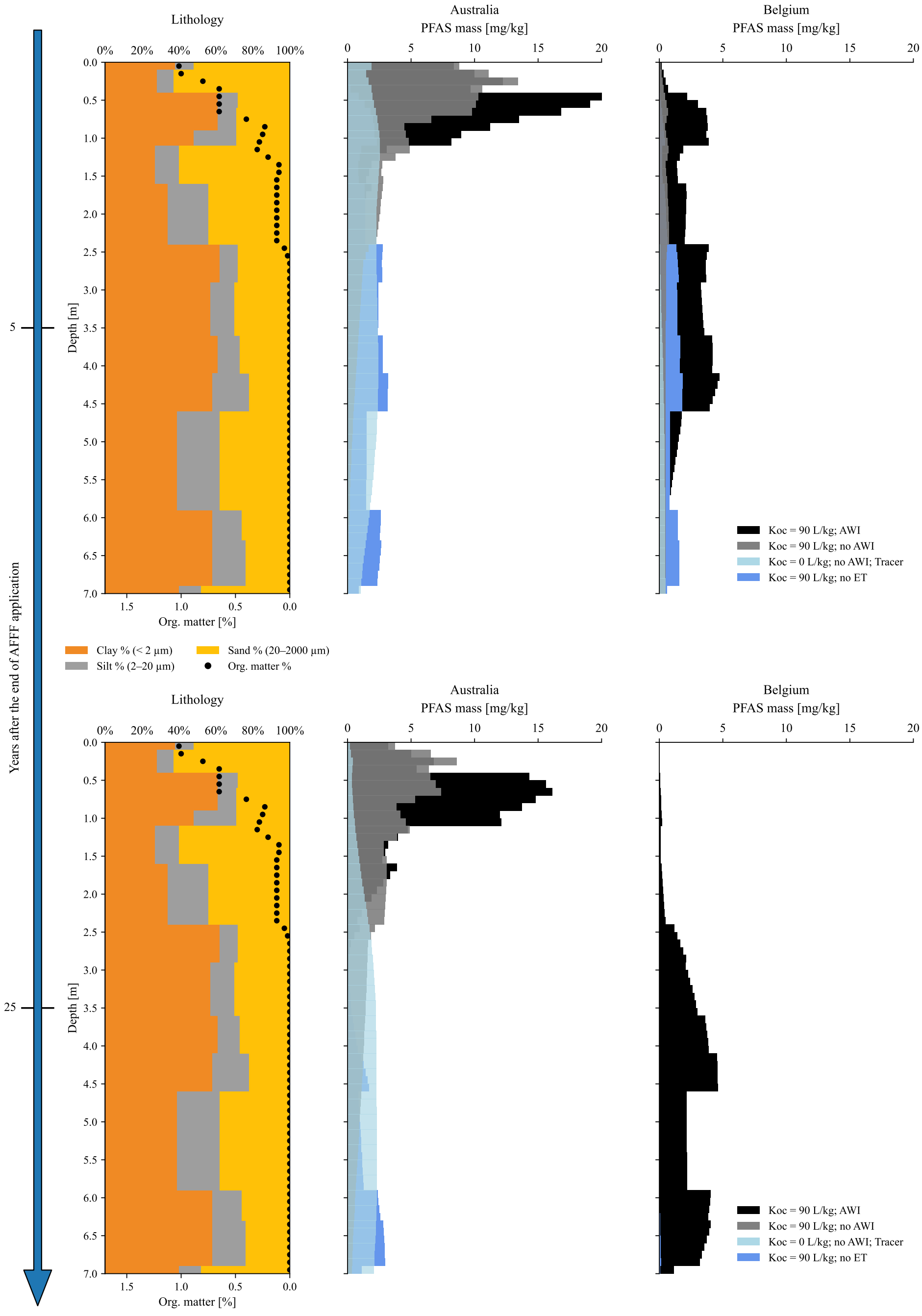

FIGURE 7.10: Simulation with AFFF foams applied from 1970 to 1995; profiles shown 5-25 years after cessation. Under ‘normal’ conditions (black), Belgium shows deeper, more dispersed PFAS mass than Australia, where mass remains largely near-surface. The tracer (light blue) penetrates faster in Belgium, indicating higher water infiltration. Removing evapotranspiration (blue) produces much deeper migration, especially in Australia. Removing AWI (grey) increases mobility in both settings, with the greatest deepening in Belgium.

7.4.4 Discussion

Overall, FIGURE 7.7 helps evaluate whether the observations and hypotheses of Wallis et al. (2022) also apply to the reproduced model under Belgian conditions, particularly regarding the effect of evapotranspiration on PFAS retention. As noted in Wallis et al. (2022), under Australian conditions decreases in PFAS concentrations and mass coincide with rainfall events and downward flux, while evapotranspiration sustains prolonged upward flow and retains PFAS in shallow horizons. Under these conditions, the total PFAS mass, whether dissolved or in porewater, fluctuates but remains broadly constant on average over the years. In a more humid environment, this trend can also be observed within the top 100 mm of soil, but upward fluxes are much weaker compared with downward fluxes. Consequently, PFAS concentrations in the surface layer clearly decline over the two years of simulation.

It can also be noted that in Australia, PFAS concentration fluctuates almost identically over the two years, whether or not air-water interfacial adsorption is taken into account (FIGURE 7.7). In Belgium, however, when AWI retention is not included, concentrations in the surface layer are noticeably lower, indicating that AWI processes exert a stronger influence under temperate conditions.

FIGURE 7.8 shows that the effects of evapotranspiration on PFAS retention in the first 100 mm of soil are far less significant under temperate conditions than under Mediterranean ones. In Belgium, porewater concentrations within this shallow layer appear almost identical with or without evapotranspiration. The changes linked to evapotranspiration exceeding rainfall are negligible compared with the Australian case. In Australia, by contrast, the absence of evapotranspiration produces concentrations in this layer that are very similar to those observed under Belgian conditions.

Considering PFAS retention within the first two metres of soil, FIGURE 7.9 shows that AWI retention and retention linked to upward fluxes from evapotranspiration have a comparable impact on the total mass in this zone. Throughout the simulation under Belgian conditions, the mass in this layer evolves in a similar way whether ET or AWI retention is considered, whereas under Australian conditions the role of ET in retaining PFAS in the top two metres is clearly more pronounced, as already highlighted in SECTION 7.3.

FIGURE 7.9 also reveals a difference in PFAS transport through the rest of the profile under Belgian conditions. In 1995, the median tracer mass without ET is located around 6.25 m deep, compared to more than 7 m when AWI retention is not considered. This suggests that, for the entire soil profile under Belgian conditions, AWI retention may play a greater role than evapotranspiration.

FIGURE 7.10 shows that removing evapotranspiration produces much deeper migration, particularly under Australian conditions. However, under both climatic scenarios with identical field settings, simulated PFAS leaching becomes really similar when evapotranspiration is excluded, confirming that this process is the main factor driving the differences between the two climates. The more pronounced PFAS leaching observed under Belgian conditions can therefore be attributed to the lower influence of evapotranspiration. Furthermore, when AWI retention is removed, PFAS mobility increases in both cases, with the greatest difference in leached mass observed in Belgium. This is consistent with the fact that in Australia retention is primarily controlled by evapotranspiration, whereas in Belgium it depends more strongly on AWI processes.

Although PFAS appear to migrate at a similar rate within the first two metres of soil regardless of whether AWI or ET is neglected (see FIGURE 7.9), AWI retention subsequently exerts the greatest control on migration, as shown in FIGURE 7.10. While other processes such as solid-phase sorption, precipitation, or partitioning to the gas phase are also represented in the model, under the more humid Belgian conditions PFAS retention appears to be dominated by AWI interactions with the soil lithology.

7.5 Conclusion of the chapter

Results show that physical processes such as precipitation and evapotranspiration exert strong control on water fluxes and PFAS migration through soils. In Australia, most water loss occurs through evaporation, which reduces the amount of water available for leaching and strongly influences PFAS transport. Under Mediterranean conditions, evapotranspiration therefore has a much stronger effect in the shallow part of the soil profile than under temperate conditions. It retains most of the PFAS mass within the first two metres for decades.

This chapter also shows that evapotranspiration is the main driver of the contrasting leaching patterns observed between the two climates. Indeed, when this process is removed from the model, PFAS distributions under Mediterranean conditions become comparable to those under a temperate climate, despite lower infiltration.

The climatic impact on PFAS leaching is also visible in the variability of leaching rates. In Belgium, interannual changes in rainfall and evapotranspiration significantly affect PFAS transport.

Finally, neglecting AWI retention has less influence under Mediterranean conditions, where evapotranspiration dominates transport. In contrast, under Belgian conditions, in clay- and silt-rich soils such as this one, PFAS retention appears to be mainly controlled by air-water interfacial adsorption on clay lenses.

These findings should nonetheless be interpreted with caution, as they are site-specific. Only one soil type was considered, and Wallis et al. (2022) showed that clay provides a particularly large air-water interfacial surface.

Part III

Conclusion and perspectives

Chapter 8

Conclusion and perspectives

8.1 Conclusion

This work set out to clarify how per- and polyfluoroalkyl substances (PFAS) move through the vadose zone. This topic is crucial today, as the transport of these persistent and mobile substances in the environment remains poorly understood. PFAS are found widely across environmental compartments, making it important to understand their behaviour in order to remediate contaminated sites.

The literature review conducted at the start of the study highlighted that PFAS constitute a very large family of contaminants with diverse properties. However, they share a property that is uncommon among other pollutants: a marked tendency to adsorb at interfaces and surfaces between phases, owing to their surfactant nature. Understanding the importance of this property for PFAS transport is therefore essential. In addition, the state-of-the-art highlights that PFAS transport is mainly governed by solid-phase sorption, air-water interfacial adsorption (AWI), climate-driven physical processes, and the degradation of precursor PFAAs.

In this context, the study emphasised climate-driven processes. After spending two months in Australia and studying site PFAS transport there, it was of interest to compare with conditions representative of a more temperate climate. In addition, AWI sorption was selected as a parameter of interest because this subsurface retention process is still poorly understood in Belgium and is not yet represented in conventional tools used to estimate pollutant transport in the vadose zone.

To carry this project through, the transport mechanisms governing PFAS leaching were analysed using a one-dimensional model implemented in the LEACHM software. LEACHM takes as input a climatic time series (temperature, rainfall, and evapotranspiration) and solves Richards' equation to reproduce water fluxes through the soil profile. Solute transport is simulated under transient conditions with the convection-dispersion equation (CDE). The findings presented here therefore derive directly from the outcomes of the model simulations.

The study initially aimed to reproduce the model developed by Wallis et al. (2022) for a silty clay soil under Mediterranean-type conditions in Adelaide, Australia. The meteorological dataset was then adapted to Belgian temperate conditions. The results show that weather is an essential, non-negligible control on PFAS leaching in the vadose zone. Because of evapotranspiration and rainfall regimes, the dominant transport processes differ markedly between Australia and Belgium. Evapotranspiration, initially identified as the main driver that retains PFAS within the upper two metres under Australian conditions, proved much less influential under more humid conditions. However, for this silty-clayey site, the role of the air-water interface is comparatively more significant under Belgian conditions than under Australian ones. Indeed, even without this process, PFAS retention under Australian conditions showed limited differences because evapotranspiration exerted the dominant control, an effect that is not observed in Belgium. When evapotranspiration is excluded, the differences between climates largely disappear, confirming its central role. In both conditions, PFAS retention seems to occur mainly in clay-and silt-rich soils, likely due to a larger air-water interfacial area. Finally, interannual climatic variability has a marked impact on PFAS leaching rates, underscoring the need for a climate record that is representative of the site when modelling PFAS behaviour from the source zone to groundwater. These conclusions remain, however, site-specific, as only one soil type was assessed.

8.2 Perspectives

In this study, the modelling framework was only adapted to Belgian conditions to assess their influence on PFAS leaching. Several parameters could be further refined to better represent local conditions. For example, site-specific water retention curves would improve the representation of subsurface water fluxes and PFAS transport. Pedological factors such as organic carbon content, soil texture, and lithology greatly affect PFAS sorption, while vegetation characteristics, likely more significant in temperate conditions, would affect evapotranspiration and root water uptake. Adjusting these parameters to better reflect temperate European environments would yield more realistic predictions.

Although the seasonal and interannual variability of the weather was taken into account, its influence on the groundwater table was not considered, as free drainage was assumed. However, accounting for water table fluctuations would provide a more realistic representation of changes in soil saturation and the resulting variation in PFAS concentrations, and thus PFAS leaching, in the vadose zone.

Another improvement would be to move beyond treating PFAS as a single group with generalised properties. Indeed, the model applied in this study primarily reflects the behaviour of PFOS. Investigating specific compounds individually, by prioritising those most relevant to the study site, such as those occurring at the highest concentrations or posing the greatest hazards, would provide more site-specific insights. Examining molecules that differ in chain length and functional group would allow a better representation of the diversity in sorption affinity at both the air-water interface and the solid phase, as well as differences in solubility and capacity to alter surface tension. In addition, considering the transformation of certain PFAS precursors into terminal PFAS would provide a more realistic representation, given their distinct properties. These improvements could reveal markedly different mobility patterns under contrasting hydrological conditions. Such an approach would help to identify the compounds of greatest environmental concern and support the development of targeted mitigation strategies.

Furthermore, using LEACHM to evaluate the effectiveness of soil remediation techniques for PFAS-contaminated sites represents a promising approach. Based on the dataset of distribution coefficients ($\mathrm{K_D}$) established during my internship for different PFAS-additive combinations (see APPENDIX E), the modelling of chemical stabilisation and solidification could help quantify how specific amendments influence PFAS retention and transport processes. By incorporating K_d values representative of particular treatments, it would be possible to assess remediation efficiency under both Mediterranean and temperate climatic conditions. Such simulations would need to be validated against laboratory or field-scale experiments to ensure representativeness, but this work could support the selection and optimisation of remediation strategies. The version of LEACHM used in this project required manual adaptation of soil parameters to reflect the treatments. However, an extended PFAS-oriented version released this year integrates binder applications for soil remediation and could prove highly valuable. Ultimately, coupling remediation modelling with site-specific data would improve risk assessments and contribute to more effective management of legacy PFAS contamination.

Using Hydrus or other modelling tools in addition to LEACHM would allow for a comparison of results, help to assess the significance of LEACHM's limitations relative to other approaches, and, more importantly, provide different perspectives on the parameters governing PFAS leaching.

Appendix A

History of PFAS

A.1 Evolution of PFAS Manufacturing Processes

According to ITRC (2023), the production of most PFAS found in the environment began after the Second World War. Before that, only a few fluoropolymers, such as polytetrafluoroethylene (PTFE), were used (TABLE A.1). PFAS production began to expand when 3M licenced Simons' electrochemical fluorination (ECF) process in 1945 and started commercial production in 1951. Historically, the ECF process was primarily used to produce perfluorooctane sulfonyl fluoride (POSF), which served as a precursor to PFOS-based substances. It was also used to synthesise perfluorooctane carbonyl fluoride that could then be used in the production of PFOA and related compounds. As shown in TABLE A.1, ECF was the dominant method for producing PFAS compounds between 1947 and 2002 (ITRC, 2023; Buck et al., 2011).

TABLE A.1: Discovery and manufacturing history of select PFAS (ITRC, 2023).

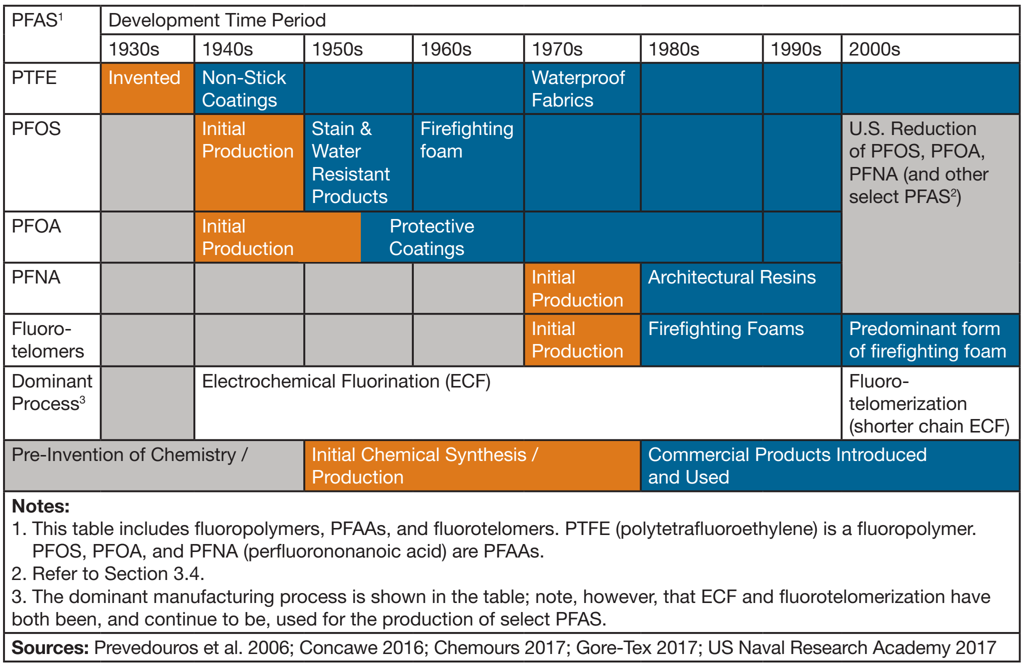

PFAS[1]	Development Time Period						
	1930s	1940s	1950s	1960s	1970s	1980s	1990s	2000s
PTFE	Invented	Non-Stick Coatings			Waterproof Fabrics			
PFOS		Initial Production	Stain & Water Resistant Products	Firefighting foam				U.S. Reduction of PFOS, PFOA, PFNA (and other select PFAS[2])
PFOA		Initial Production	Protective Coatings					
PFNA					Initial Production	Architectural Resins		
Fluoro-telomers					Initial Production	Firefighting Foams		Predominant form of firefighting foam
Dominant Process[3]		Electrochemical Fluorination (ECF)						Fluoro-telomerization (shorter chain ECF)
Pre-Invention of Chemistry /		Initial Chemical Synthesis / Production			Commercial Products Introduced and Used			

Notes:
1. This table includes fluoropolymers, PFAAs, and fluorotelomers. PTFE (polytetrafluoroethylene) is a fluoropolymer. PFOS, PFOA, and PFNA (perfluorononanoic acid) are PFAAs.
2. Refer to Section 3.4.
3. The dominant manufacturing process is shown in the table; note, however, that ECF and fluorotelomerization have both been, and continue to be, used for the production of select PFAS.

Sources: Prevedouros et al. 2006; Concawe 2016; Chemours 2017; Gore-Tex 2017; US Naval Research Academy 2017

The second main manufacturing process for PFAS, fluoro-telomerisation, was developed in the 1970s, initially by the company DuPont (Ineris, 2024). This process became increasingly important, particularly after the major global historic manufacturer using the ECF process, 3M Company, announced in 2002 that it would phase out the production of PFOS, PFOA, and other 6-, 8-, and 10-carbon perfluoroalkane sulfonyl derivatives (ITRC, 2023; Buck et al., 2011). Following this decision, 3M retained the ECF process but adapted it to use perfluorobutane chemistry, introducing alternative products based on perfluorobutane sulfonyl derivatives. This marked a shift within the ECF process from C8 to C4 sulfonyl substances (Buck et al., 2011). These shorter-chain substances, such as PFBS, were selected because of their reduced bioaccumulation potential and more rapid elimination in tested organisms. A significant increase in PFBS levels has since been reported in environmental waters (Buck et al., 2011). In parallel, telomer-based technologies were developed to produce shorter-chain perfluoroalkyl or polyfluorinated substances, including fluorotelomer alcohols (FTOHs) such as 6:2 FTOH and 8:2 FTOH. These compounds became predominant in aqueous film-forming foam (AFFF) formulations following the phase-out of long-chain ECF-based PFAS (Lyu et al., 2022; Rasmusson & Fagerlund, 2024). Telomer-derived compounds such as 6:2 fluorotelomer sulfonic acid (6:2 FTSA) are now widely used in fire-fighting foams (Rasmusson and Fagerlund, 2024). As shown in TABLE A.1, telomerisation is now the dominant production method for many PFAS, particularly fluorinated surfactants and side-chain fluorinated polymers (Buck et al., 2011; ITRC, 2023; Rasmusson and Fagerlund, 2024).

A.2 Evolution of PFAS detection and scientific awareness

The study of the environmental and human health impacts of PFAS is still a relatively recent field. The first scientific reports that brought PFAS to the attention of the wider research community were published in 2001. Giesy and Kannan (2001) demonstrated the global occurrence of PFOS in wildlife, while Hansen et al. (2001) reported the frequent detection of PFAS in human blood. Since then, growing awareness of PFAS has led to both research and speculation about the use and occurrence of PFAS, and whether such occurrences may constitute a risk to human health and the environment (ITRC, 2023). The scientific literature on the environmental and toxicological aspects of PFAS burgeoned rapidly, and the rate of publication even exceeded 400 articles per year in 2011 (Buck et al., 2011).

The two most prominent classes of PFAA, namely PFCAs and PFSAs, have received considerable scientific and regulatory attention. Unsurprisingly, the order in which PFAS have been studied closely reflects their environmental impact. It is therefore logical that PFOS and PFOA are the two PFAS for which the scientific literature is most abundant. As illustrated by FIGURE A.1, research has gradually expanded over the years to include other PFAS, following their relevance and emergence in environmental monitoring. In contrast, other subclasses of PFAAs (cfr SECTION 2.1) have remained largely underexplored by the scientific community (ITRC, 2023; Lyu et al., 2022).

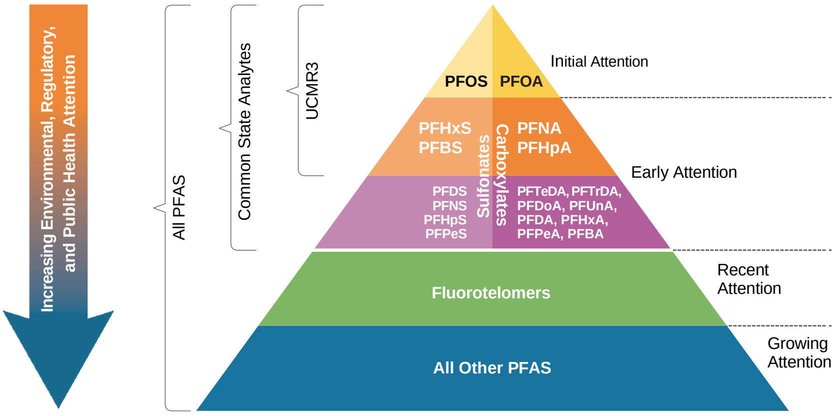

Thematic and not proportional. Bottom of triangle indicates additional number of compounds; not a greater quantity by mass, concentration, or frequency of detection.

Note: UCMR3 (Unregulated Contaminant Monitoring Rule 3) is an initiative by the U.S. Environmental Protection Agency (USEPA), in 2012, aimed at monitoring substances suspected to occur in drinking water but for which no regulatory standards yet existed. It included the monitoring of six PFAS, namely PFOS, PFOA, PFNA, PFHxS, PFHpA and PFBS (ITRC,2023).

FIGURE A.1: Emerging awareness and emphasis on PFAS occurrence in the environment (from J. Hale, Kleinfelder and modified from ITRC,2023).

PFAS have relatively recently attracted the attention of researchers and especially the public largely because until the early 2000s, analytical methods to detect low levels of PFAS in the environment were only available at a few selected research institutions. It was only in the early 2010s that these methods to detect a limited number of PFAS became widely available and that the detection limits in water were sufficiently low to be proportional to the levels of potential effects on human health. Toxicological studies have raised concerns regarding the bioaccumulative nature and potential health concerns of some PFAS. As a result, our understanding of PFAS and the risks they may pose is rapidly evolving (ITRC, 2023).

Appendix B

Regulatory thresholds for PFAS in Belgium and Australia

B.1 Current PFAS thresholds in groundwater, soil and surface water in Wallonia, Belgium

In Wallonia, the applicable regulatory thresholds for PFAS contamination are in accordance with the Walloon guidelines for soil decree studies issued by SPW ARNE[1], with input from SPAQuE[2] and ISSeP[3]. These thresholds are used to identify the presence of pollution and to determine whether further risk assessment studies should be conducted.

Thresholds for per- and polyfluoroalkyl substances (PFAS) in groundwater are based on the limits for drinking water quality established by the European Drinking Water Directive (2020/2184). While not formal groundwater limit values under the soil decree, these concentrations are used as interpretative benchmarks in soil decree studies to assess potential contamination (SPW ARNE, 2025). Two cumulative indicators are used:

- The sum of 20 priority PFAS compounds[4]: **0.1 µg/L**
- The sum of all quantifiable PFAS compounds using accredited methods: **0.5 µg/L**

All compounds with concentrations above the laboratory's reporting limit (LR)[5] must be included in the sum.

For trifluoroacetic acid (TFA), a signal value of 2.2 µg/L currently applies to groundwater. As for soils, no provisional threshold value has been defined yet. If the concentration of TFA in a soil sample exceeds the laboratory's reporting limit (LR), the expert is advised to contact the competent authority for further guidance.

For soils, no European standard has been defined, nor is any currently under development. Similarly, Wallonia has not established any threshold value for the sum of PFAS in soil to date. Instead, values are assessed compound by compound. The applicable threshold, referred to as $\mathrm{VL}_{\mathrm{sol}}$ (soil limit value), is defined as the lower of:

$$\mathrm{VL}_{\mathrm{sol}} = \min(\mathrm{VL}_{\mathrm{H}}, \mathrm{VL}_{\mathrm{N}})$$

---

[1] SPW ARNE = Walloon administration responsible for natural resource management, biodiversity conservation, groundwater protection, and the implementation of sustainable agricultural and environmental policies.

[2] SPAQuE = Walloon public agency in charge of soil remediation.

[3] ISSeP = Regional scientific institute for environmental monitoring and risk assessment.

[4] Shown in TABLE 2.1 of SECTION 2.1.

[5] LR = Minimum concentration for which a laboratory is required to report a quantitative result. It may be higher than the limit of quantification due to practical considerations, such as sample dilution.

where VL_H and VL_N respectively refer to the threshold value in soil for protecting human health, and for protecting groundwater from contamination via leaching. VL_N is often more restrictive than VL_H for PFAS compounds, except in the case of agricultural soils (type II). Since this study focusses on an airport site, the applicable thresholds for a selection of PFAS compounds in industrial soils (type V) are presented in TABLE B.1. In fact, VL_N values are derived from indicative groundwater thresholds (VL_{nappe}), which themselves are based on international drinking water standards (SPW ARNE, 2025). The corresponding individual groundwater thresholds currently used in Wallonia can be found at the end of this SECTION.

For compounds without defined thresholds, a default $VL_{sol} = 2 \times LR$ is applied. The standard LR for quantifiable substances is 0.5 µg/kg dry matter (DM).

TABLE B.1: PFAS soil threshold values for industrial use (Type V), from SPW ARNE (2025).

Compound	VLH (µg/kg DM)	VLN (µg/kg DM)	VLsol (µg/kg DM)
PFOA	2163	0.5	0.5
PFOS	2964	1.0	1.0
PFNA	1818	0.6	0.6
PFDA	244.3	0.1	0.5[†]
PFHxS	1903	0.4	0.5[†]
PFHxA	630[*]	3.3	3.3
PFBA	4800[*]	99	99

These seven PFAS were selected because they are among the few for which soil threshold values (VL_{sol}) have been defined in the Walloon guidelines. For the first five compounds, VL_H values are differentiated by soil use type and were derived using the S-Risk software. The last two compounds are part of a group of 15 additional PFAS for which single VL_H and VL_N values are proposed, based on a risk assessment carried out by the State of Hawaii (USA) in December 2023.

[†] If the calculated value of VL_{sol} falls below the reporting limit, then VL_{sol} is set equal to the LR.

[*] No VL_H defined for Type V; value from unrestricted use applied.

Note: For more detailed information on the thresholds defined for each PFAS compound, it is recommended to consult the publication by SPW ARNE (2025). These threshold values may evolve over time; experts are therefore advised to refer to the latest official version available on the SPW ARNE website.

Regarding surface waters, the European Union is currently developing a dedicated PFAS standard. In the meantime, specific recommendations have been issued for environmental assessments. Analytical investigations should cover at least the 24 PFAS compounds expected to be included in the upcoming European directive (referred to as PFAS(24)). Most accredited laboratories offer an extended PFAS(28) package, combining the PFAS(24) for surface waters and the 20 PFAS regulated in groundwater. These lists of PFAS are presented in TABLE 2.1 of SECTION 2.1.

A reference threshold of 0.1 μg/L is proposed for the total concentration of PFAS(24) in surface waters. However, no fixed discharge limit is set for industrial effluents; thresholds are instead determined case-by-case by the Surface Water Directorate.

NB: Since this study is based on an Australian model, an overview of the current regulatory guidelines for PFAS in Australia is provided in APPENDIX B.2 for reference.

Groundwater Belgian thresholds for PFAS

TABLE B.2 provides indicative groundwater threshold values (VL_{nappe}) for selected PFAS. These values are not directly used for the derivation of regulatory threshold values for groundwater, which are strictly based on the European directive. However, they are used for the calculation of the composite groundwater threshold value

(VL_N), and may also support the "detergents" strategy as reference limits for anionic surfactants (SPW ARNE, 2025).

TABLE B.2: PFAS groundwater thresholds (VL_{nappe}) used for VL_N calculation in Wallonia (SPW ARNE, 2025).

PFAS	**VL_{nappe} retained (µg/L)**	**Source of the value**
PFOA	0.018	WHO calculation (2020)
PFOS	0.012	WHO calculation (2020)
PFNA	0.01	US EPA (2024)
PFDA	0.00042	WHO calculation (2023)
PFHxS	0.004	US EPA (2024)

B.2 Groundwater, soil and surface water current PFAS thresholds in Australia

In Australia, national guidance on per- and polyfluoroalkyl substances (PFAS) is provided by the *PFAS National Environmental Management Plan (NEMP) Version 3.0* (HEPA, 2025), jointly endorsed by Australian and New Zealand jurisdictions. The threshold values set out in this document are intended as indicative levels or triggers for further investigation, rather than as clean-up criteria or authorisations to pollute up to those levels. Unlike in Belgium, exceedance of these values does not in itself imply that contamination is present or that harm has occurred. Instead, the primary objective is to minimise exposure and to protect human health and the environment.

In Australia, if groundwater is used for drinking purposes, drinking water quality guidelines apply. Unlike in Europe, where cumulative thresholds are defined for groups of PFAS, the Australian guidelines specify individual values for selected compounds:

- Sum of PFOS and PFHxS: **0.07 µg/L**
- PFOA: **0.56 µg/L**

These values are based on sources such as the National Health and Medical Research Council (NHMRC, 2011) and the New Zealand Department of Internal Affairs (2022).

For both surface and groundwater quality, ecological guideline values for PFOS and PFOA are defined for freshwater and marine environments based on species protection levels. These indicative values are drawn from the 2023 ANZG (Australian and New Zealand Guidelines for Fresh and Marine Water Quality) and correspond to specific protection levels for aquatic species. For example, for 99% species protection (high conservation value systems) in surface waters:

- PFOS: **0.00023 µg/L**
- PFOA: **19 µg/L**

Additional indicative values are provided for 95%, 90%, and 80% species protection in the document of HEPA (2025).

As in Wallonia (Belgium), no standardised thresholds have been established for PFAS concentrations in industrial discharges to surface waters. Instead, discharge limits are typically set on a site-specific basis by the competent surface water authority, in accordance with environmental objectives and relevant jurisdictional legislation (HEPA, 2025).

In soils, *Health Investigation Levels* (HILs) are defined for various land use scenarios and represent concentrations at which a human health risk assessment should be considered. For industrial or commercial land use (HIL D), the following indicative values apply:

- Sum of PFOS and PFHxS: **20 mg/kg**
- PFOA: **50 mg/kg**

Appendix C

Water retention curve: Campbell, Hutson-Cass function

According to Hutson (2003), the soil water retention behaviour in the vadose zone can be represented using the method of Campbell (1974), as modified by Hutson and Cass (1987). This approach expresses the matric potential h (pressure head) as a continuous function of volumetric water content θ by combining an exponential branch for low potentials with a parabolic branch for high potentials:

$$h(\theta) = \frac{a(1-\theta/\theta_s)^{\frac{1}{2}}\,(\theta_c/\theta_s)^{-b}}{(1-\theta_c/\theta_s)^{\frac{1}{2}}}$$

where:

- θ_s [-] is the saturated volumetric water content,
- a [kPa] and b [-] are curve-fitting parameters,
- θ_c [-] is the water content at the junction point between the exponential and parabolic sections.

This sigmoidal curve is smooth in both value and slope, giving a realistic description from saturation to near desiccation.

Applying a capillary model to the retention function yields the corresponding unsaturated hydraulic conductivity:

$$K(\theta) \;=\; K_s \left(\frac{\theta}{\theta_s}\right)^{2b+2+p}$$

with:

- $K(\theta)$ [mm/d] : hydraulic conductivity at water content θ,
- K_s [mm/d] : saturated hydraulic conductivity,
- p [-]: pore-interaction parameter.

Together, these expressions provide a concise description of both water retention and unsaturated conductivity, well suited to layered or non-homogeneous soil profiles (Hutson, 2003).

Furthermore, here is some complementary information found in the literature concerning the different parameters introduced above. The values used to reproduce the model of Wallis et al. (2022) in CHAPTER 6 were estimated through an iterative trial-and-error process. The parameters were manually adjusted based on successive simulations until satisfactory results were achieved in terms of runoff quantity, PFAS concentrations within the profile, matric potential in the upper 50 mm of the soil and leaching to groundwater. Additionally, the default initial values provided in the LeachM software correspond to a sandy loam soil, which helped define a plausible range for the parameters used to model the sandy clay soil in Wallis et al. (2022).

- The parameter **a** is a curve-fitting parameter, but it can also be interpreted as the air-entry matric potential, which is the suction at which air first enters the pores of a saturated soil sample (Hutson, 2003; Desa and Scott, 2018). Initially, the value was set to $a = -1$ kPa. According to Desa and Scott (2018), $a = -0.4$ kPa for a clay loam soil. The value used in the present model is -0.9 kPa.
- The parameter **b** is also a curve-fitting parameter. It controls the steepness of the soil water retention curve (Hutson, 2003): the higher the value of b, the greater the water retention at low suction. Based on the initial value provided in LeachM and the findings of Pittaki-Chrysodonta et al. (2018):
  - the parameter b typically ranges from 3 to 5 for sandy soils,
  - and is approximately 11 for loamy soils.

  The value $b = 8.5$ is used for the present model.
- The parameter **p** is a pore interaction parameter. It is commonly fixed by default at $p = 1$ in the LEACHM code (Hutson, 2003).
- A saturated hydraulic conductivity (K_s) ranging from 0.1 to 3000 mm/d was measured on-site by Wallis et al. (2022). This wide range may be explained by the presence of fissures or macropores, or by a heterogeneous or disturbed soil profile creating preferential flow paths. For comparison, Abkenar et al. (2019) reported K_s values of 130 mm/d for clay loam, 865 mm/d for loam, and approximately 1240 mm/d for loamy sand. The value used in the present model is 700 mm/d.
- The **field capacity** is the water content remaining in the soil after gravitational drainage (Hutson, 2003). The value used in the present model is -20 kPa.

Appendix D

RMI: Gridded observational data

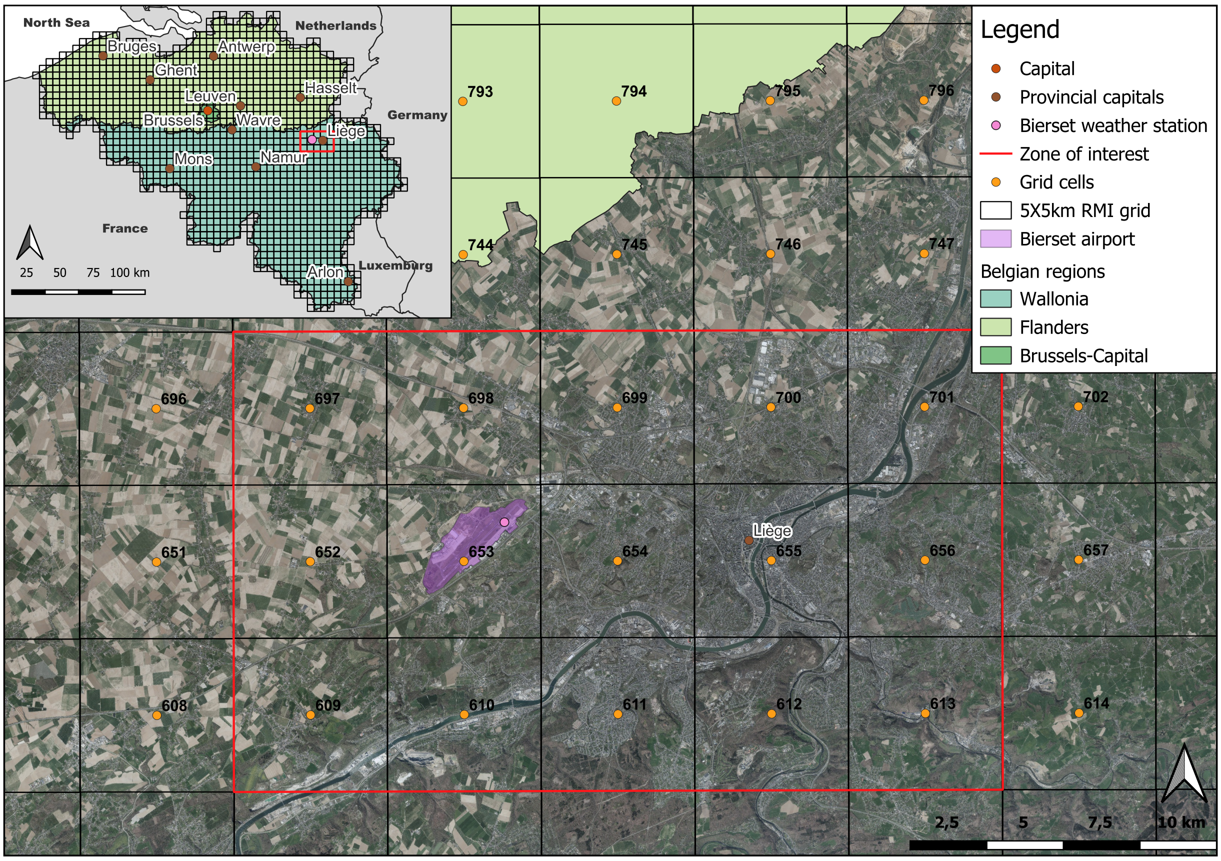

FIGURE D.1: Map showing the 5x5 km observational data grid of the RMI and the Bierset airport location.

Appendix E

K_D dataset

The Excel file was organised so that each article read and included in the dataset is represented by a specific colour, based on its font style, as illustrated in the figure below. Articles that were not used are shown in black font on a red background. These articles are still kept because they contain valuable information.

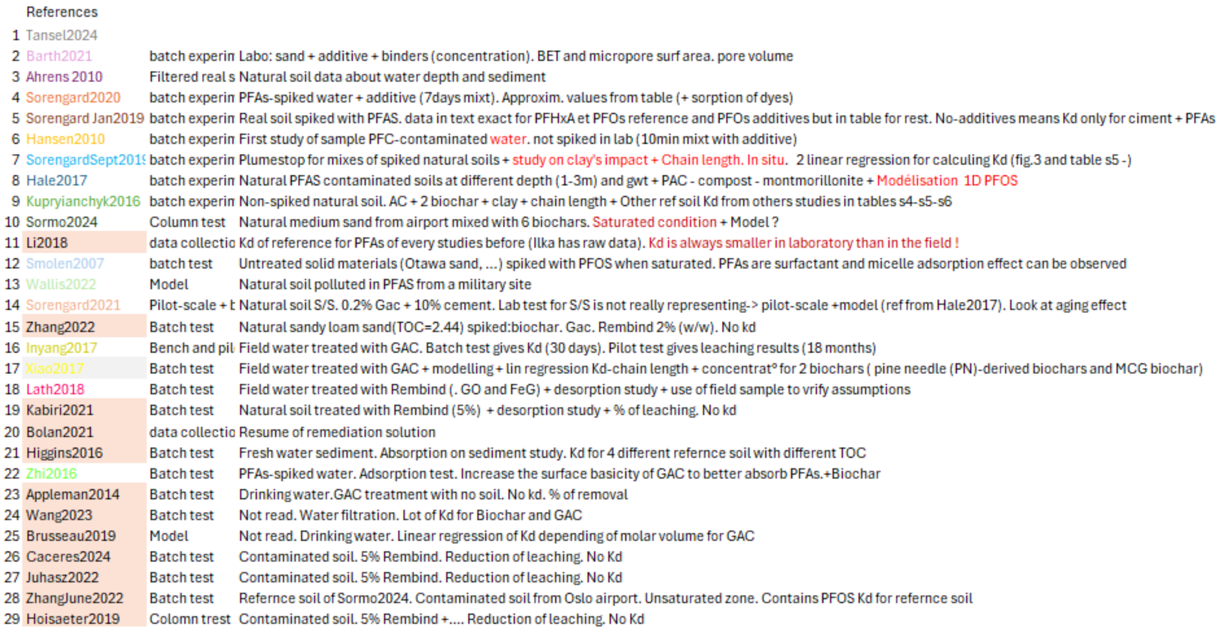

	References		
1	Tansel2024		
2	Barth2021	batch experin	Labo: sand + additive + binders (concentration). BET and micropore surf area. pore volume
3	Ahrens 2010	Filtered real s	Natural soil data about water depth and sediment
4	Sorengard2020	batch experin	PFAs-spiked water + additive (7days mixt). Approxim. values from table (+ sorption of dyes)
5	Sorengard Jan2019	batch experin	Real soil spiked with PFAS. data in text exact for PFHxA et PFOs reference and PFOs additives but in table for rest. No-additives means Kd only for ciment + PFAs
6	Hansen2010	batch experin	First study of sample PFC-contaminated water. not spiked in lab (10min mixt with additive)
7	SorengardSept201	batch experin	Plumestop for mixes of spiked natural soils + study on clay's impact + Chain length. In situ. 2 linear regression for calculing Kd (fig.3 and table s5 -)
8	Hale2017	batch experin	Natural PFAS contaminated soils at different depth (1-3m) and gwt + PAC - compost - montmorillonite + Modélisation 1D PFOS
9	Kupryianchyk2016	batch experin	Non-spiked natural soil. AC + 2 biochar + clay + chain length + Other ref soil Kd from others studies in tables s4-s5-s6
10	Sormo2024	Column test	Natural medium sand from airport mixed with 6 biochars. Saturated condition + Model ?
11	Li2018	data collectio	Kd of reference for PFAs of every studies before (Ilka has raw data). Kd is always smaller in laboratory than in the field !
12	Smolen2007	batch test	Untreated solid materials (Otawa sand, ...) spiked with PFOS when saturated. PFAs are surfactant and micelle adsorption effect can be observed
13	Wallis2022	Model	Natural soil polluted in PFAS from a military site
14	Sorengard2021	Pilot-scale + t	Natural soil S/S. 0.2% Gac + 10% cement. Lab test for S/S is not really representing-> pilot-scale +model (ref from Hale2017). Look at aging effect
15	Zhang2022	Batch test	Natural sandy loam sand(TOC=2.44) spiked:biochar. Gac. Rembind 2% (w/w). No kd
16	Inyang2017	Bench and pil	Field water treated with GAC. Batch test gives Kd (30 days). Pilot test gives leaching results (18 months)
17	Xiao2017	Batch test	Field water treated with GAC + modelling + lin regression Kd-chain length + concentrat° for 2 biochars (pine needle (PN)-derived biochars and MCG biochar)
18	Lath2018	Batch test	Field water treated with Rembind (. GO and FeG) + desorption study + use of field sample to vrify assumptions
19	Kabiri2021	Batch test	Natural soil treated with Rembind (5%) + desorption study + % of leaching. No kd
20	Bolan2021	data collectio	Resume of remediation solution
21	Higgins2016	Batch test	Fresh water sediment. Absorption on sediment study. Kd for 4 different refernce soil with different TOC
22	Zhi2016	Batch test	PFAs-spiked water. Adsorption test. Increase the surface basicity of GAC to better absorb PFAs.+Biochar
23	Appleman2014	Batch test	Drinking water.GAC treatment with no soil. No kd. % of removal
24	Wang2023	Batch test	Not read. Water filtration. Lot of Kd for Biochar and GAC
25	Brusseau2019	Model	Not read. Drinking water. Linear regression of Kd depending of molar volume for GAC
26	Caceres2024	Batch test	Contaminated soil. 5% Rembind. Reduction of leaching. No Kd
27	Juhasz2022	Batch test	Contaminated soil. 5% Rembind. Reduction of leaching. No Kd
28	ZhangJune2022	Batch test	Refernce soil of Sormo2024. Contaminated soil from Oslo airport. Unsaturated zone. Contains PFOS Kd for refernce soil
29	Hoisaeter2019	Colomn trest	Contaminated soil. 5% Rembind +.... Reduction of leaching. No Kd

FIGURE E.1: Bibliography used to create the dataset

The Excel file is organised with, first of all, all the K_D values for the untreated soils, referred to as reference soils. These are displayed with a grey background and serve as a comparison point to evaluate the evolution of K_D values. Each soil treated with a specific additive is highlighted in a different colour, with each colour representing the chemical stabilisation remediation technique. Only the yellow colour is used to indicate K_D values for soils treated by solidification.

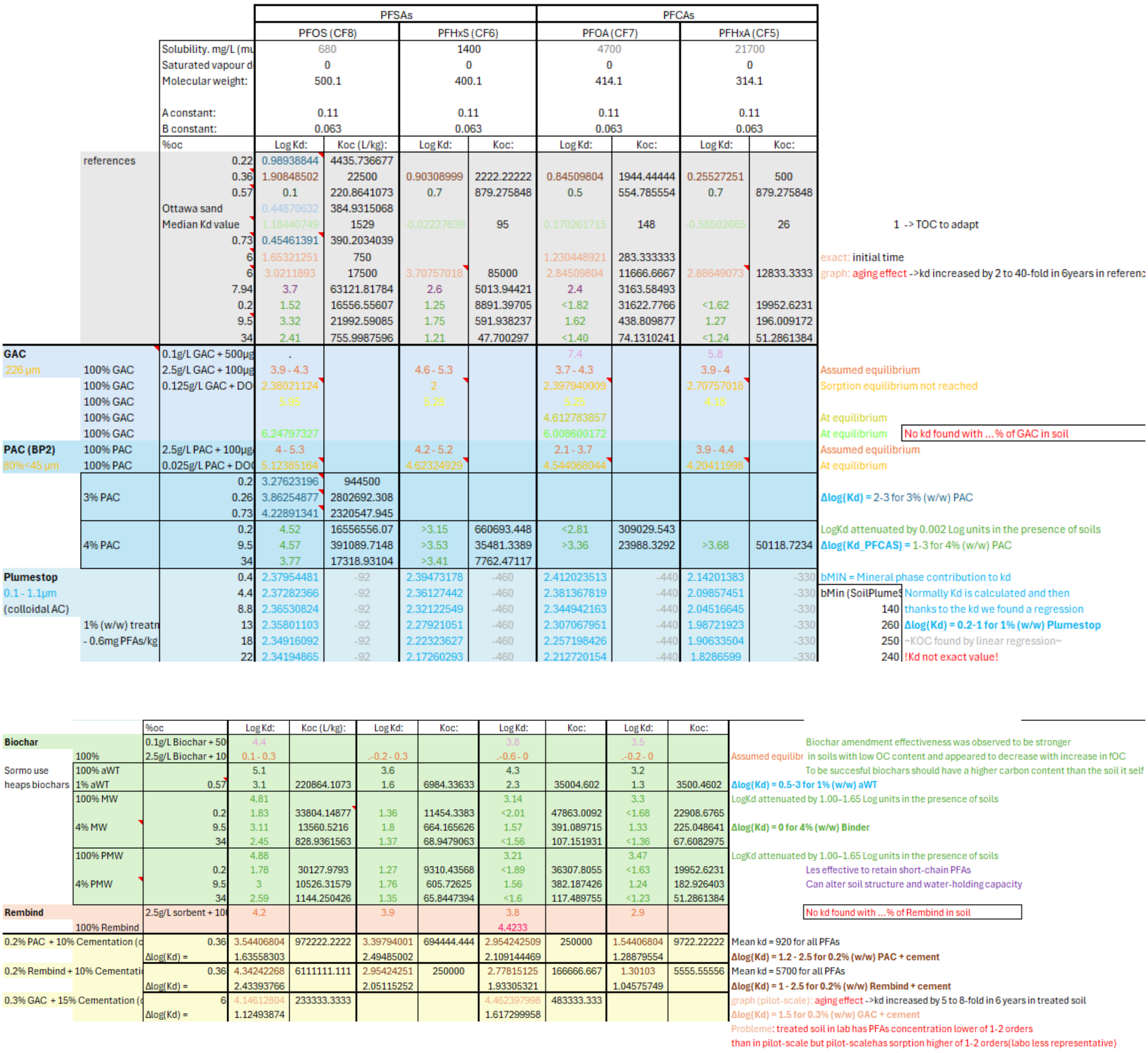

			PFSAs				PFCAs					
			PFOS (CF8)		PFHxS (CF6)		PFOA (CF7)		PFHxA (CF5)			
		Solubility. mg/L (mu	680		1400		4700		21700			
		Saturated vapour d	0		0		0		0			
		Molecular weight:	500.1		400.1		414.1		314.1			
		A constant:	0.11		0.11		0.11		0.11			
		B constant:	0.063		0.063		0.063		0.063			
		%oc	Log Kd:	Koc (L/kg):	Log Kd:	Koc:	Log Kd:	Koc:	Log Kd:	Koc:		
	references	0.22	0.98938844	4435.736677								
		0.36	1.90848502	22500	0.90308999	2222.22222	0.84509804	1944.44444	0.25527251	500		
		0.57	0.1	220.8641073	0.7	879.275848	0.5	554.785554	0.7	879.275848		
		Ottawa sand	0.44870632	384.9315068								
		Median Kd value	1.18440749	1529	-0.02227639	95	0.170261715	148	-0.58502665	26	1 -> TOC to adapt	
		0.73	0.45461391	390.2034039								
		6	1.65321251	750			1.230448921	283.333333			exact: initial time	
		6	3.0211893	17500	3.70757018	85000	2.84509804	11666.6667	2.88649073	12833.3333	graph: aging effect ->kd increased by 2 to 40-fold in 6years in referen	
		7.94	3.7	63121.81784	2.6	5013.94421	2.4	3163.58493				
		0.2	1.52	16556.55607	1.25	8891.39705	<1.82	31622.7766	<1.62	19952.6231		
		9.5	3.32	21992.59085	1.75	591.938237	1.62	438.809877	1.27	196.009172		
		34	2.41	755.9987596	1.21	47.700297	<1.40	74.1310241	<1.24	51.2861384		
GAC		0.1g/L GAC + 500µg	.				7.4		5.8			
226 µm	100% GAC	2.5g/L GAC + 100µg	3.9 - 4.3		4.6 - 5.3		3.7 - 4.3		3.9 - 4		Assumed equilibrium	
	100% GAC	0.125g/L GAC + DO	2.38021124		2		2.397940009		2.70757018		Sorption equilibrium not reached	
	100% GAC		5.95		5.28		5.25		4.18			
	100% GAC						4.612783857				At equilibrium	
	100% GAC		6.24797327				6.008600172				At equilibrium	No kd found with ...% of GAC in soil
PAC (BP2)	100% PAC	2.5g/L PAC + 100µg	4 - 5.3		4.2 - 5.2		2.1 - 3.7		3.9 - 4.4		Assumed equilibrium	
80%<45 µm	100% PAC	0.025g/L PAC + DO	5.12385164		4.62324929		4.544068044		4.20411998		At equilibrium	
		0.2	3.27623196	944500								
	3% PAC	0.26	3.86254877	2802692.308							**Δlog(Kd)** = 2-3 for 3% (w/w) PAC	
		0.73	4.22891341	2320547.945								
		0.2	4.52	16556556.07	>3.15	660693.448	<2.81	309029.543			LogKd attenuated by 0.002 Log units in the presence of soils	
	4% PAC	9.5	4.57	391089.7148	>3.53	35481.3389	>3.36	23988.3292	>3.68	50118.7234	**Δlog(Kd_PFCAS) =** 1-3 for 4% (w/w) PAC	
		34	3.77	17318.93104	>3.41	7762.47117						
Plumestop		0.4	2.37954481	-92	2.39473178	-460	2.412023513	-440	2.14201383	-330	bMIN = Mineral phase contribution to kd	
0.1 - 1.1µm		4.4	2.37282366	-92	2.36127442	-460	2.381367819	-440	2.09857451	-330	bMin (SoilPlumeS	Normally Kd is calculated and then
(colloidal AC)		8.8	2.36530824	-92	2.32122549	-460	2.344942163	-440	2.04516645	-330	140	thanks to the kd we found a regression
	1% (w/w) treatn	13	2.35801103	-92	2.27921051	-460	2.307067951	-440	1.98721923	-330	260	**Δlog(Kd) = 0.2-1 for 1% (w/w) Plumestop**
	- 0.6mg PFAs/kg	18	2.34916092	-92	2.22323627	-460	2.257198426	-440	1.90633504	-330	250	~KOC found by linear regression~
		22	2.34194865	-92	2.17260293	-460	2.212720154	-440	1.8286599	-330	240	!Kd not exact value!

		%oc	Log Kd:	Koc (L/kg):	Log Kd:	Koc:	Log Kd:	Koc:	Log Kd:	Koc:		
Biochar		0.1g/L Biochar + 50	4.4				3.8		3.5			Biochar amendment effectiveness was observed to be stronger
	100%	2.5g/L Biochar + 10	0.1 - 0.3		.-0.2 - 0.3		.-0.6 - 0		.-0.2 - 0		Assumed equilibr	in soils with low OC content and appeared to decrease with increase in fOC
Sormo use	100% aWT		5.1		3.6		4.3		3.2			To be succesful biochars should have a higher carbon content than the soil it self
heaps biochars	1% aWT	0.57	3.1	220864.1073	1.6	6984.33633	2.3	35004.602	1.3	3500.4602	**Δlog(Kd) = 0.5-3 for 1% (w/w) aWT**	
	100% MW		4.81				3.14		3.3		LogKd attenuated by 1.00–1.65 Log units in the presence of soils	
		0.2	1.83	33804.14877	1.36	11454.3383	<2.01	47863.0092	<1.68	22908.6765		
	4% MW	9.5	3.11	13560.5216	1.8	664.165626	1.57	391.089715	1.33	225.048641	**Δlog(Kd) = 0 for 4% (w/w) Binder**	
		34	2.45	828.9361563	1.37	68.9479063	<1.56	107.151931	<1.36	67.6082975		
	100% PMW		4.88				3.21		3.47		LogKd attenuated by 1.00–1.65 Log units in the presence of soils	
		0.2	1.78	30127.9793	1.27	9310.43568	<1.89	36307.8055	<1.63	19952.6231		Les effective to retain short-chain PFAs
	4% PMW	9.5	3	10526.31579	1.76	605.72625	1.56	382.187426	1.24	182.926403		Can alter soil structure and water-holding capacity
		34	2.59	1144.250426	1.35	65.8447394	<1.6	117.489755	<1.23	51.2861384		
Rembind		2.5g/L sorbent + 10	4.2		3.9		3.8		2.9			No kd found with ...% of Rembind in soil
	100% Rembind						4.4233					
0.2% PAC + 10% Cementation (c		0.36	3.54406804	972222.2222	3.39794001	694444.444	2.954242509	250000	1.54406804	9722.22222	Mean kd = 920 for all PFAs	
		Δlog(Kd) =	1.63558303		2.49485002		2.109144469		1.28879554		**Δlog(Kd) = 1.2 - 2.5 for 0.2% (w/w) PAC + cement**	
0.2% Rembind + 10% Cementati		0.36	4.34242268	6111111.111	2.95424251	250000	2.77815125	166666.667	1.30103	5555.55556	Mean kd = 5700 for all PFAs	
		Δlog(Kd) =	2.43393766		2.05115252		1.93305321		1.04575749		**Δlog(Kd) = 1 - 2.5 for 0.2% (w/w) Rembind + cement**	
0.3% GAC + 15% Cementation (c		6	4.14612804	233333.3333			4.462397998	483333.333			graph (pilot-scale): aging effect ->kd increased by 5 to 8-fold in 6 years in treated soil	
		Δlog(Kd) =	1.12493874				1.617299958				**Δlog(Kd) = 1.5 for 0.3% (w/w) GAC + cement**	
											Probleme: treated soil in lab has PFAs concentration lower of 1-2 orders	
											than in pilot-scale but pilot-scalehas sorption higher of 1-2 orders(labo less representative)	

FIGURE E.2: Dataset containing the K_D values of reference soils and soils treated using remediation techniques

Bibliography

Abkenar, F. Z., Rasoulzadeh, A., & Asghari, A. (2019). Performance evaluation of different soil water retention functions for modeling of water flow under transient condition. *Bragantia*, *78*(1), 119–130. https://doi.org/10.1590/1678-4499.2017406

Ahrens, L., Taniyasu, S., Yeung, L. W., Yamashita, N., Lam, P. K., & Ebinghaus, R. (2010). Distribution of polyfluoroalkyl compounds in water, suspended particulate matter and sediment from tokyo bay, japan. *Chemosphere*, *79*(3), 266–272. https://doi.org/https://doi.org/10.1016/j.chemosphere.2010.01.045

Appleman, T. D., Higgins, C. P., Quiñones, O., Vanderford, B. J., Kolstad, C., Zeigler-Holady, J. C., & Dickenson, E. R. (2014). Treatment of poly- and perfluoroalkyl substances in u.s. full-scale water treatment systems. *Water Research*, *51*, 246–255. https://doi.org/https://doi.org/10.1016/j.watres.2013.10.067

Brusseau, M. L. (2018). Assessing the potential contributions of additional retention processes to pfas retardation in the subsurface. *Science of The Total Environment*, *613-614*, 176–185. https://doi.org/https://doi.org/10.1016/j.scitotenv.2017.09.065

Brusseau, M. L. (2020). Simulating pfas transport influenced by rate-limited multi-process retention. *Water Research*. https://doi.org/https://doi.org/10.1016/j.watres.2019.115179

Brusseau, M. L., & Van Glubt, S. (2019). The influence of surfactant and solution composition on pfas adsorption at fluid-fluid interfaces. *Water Research*, *161*, 17–26. https://doi.org/https://doi.org/10.1016/j.watres.2019.05.095

Buck, R. C., Franklin, J., Berger, U., Conder, J. M., Cousins, I. T., de Voogt, P., Jensen, A. A., Kannan, K., Mabury, S. A., & van Leeuwen, S. P. (2011). Perfluoroalkyl and polyfluoroalkyl substances in the environment: Terminology, classification, and origins. *Integrated Environmental Assessment and Management*, *7*(4), 513–541. https://doi.org/10.1002/ieam.258

Campos-Pereira, H., Kleja, D. B., Ahrens, L., Enell, A., Kikuchi, J., Pettersson, M., & Gustafsson, J. P. (2023). Effect of ph, surface charge and soil properties on the solid-solution partitioning of perfluoroalkyl substances (pfass) in a wide range of temperate soils. *Chemosphere*, *321*, 138133. https://doi.org/https://doi.org/10.1016/j.chemosphere.2023.138133

Chemical Abstracts Service. (n.d.). *Cas registry - the authoritative source for chemical substance information*. American Chemical Society. Retrieved July 24, 2025, from https://www.cas.org/cas-data/cas-registry

Dalahmeh, S., Tirgani, S., Komakech, A. J., Niwagaba, C. B., & Ahrens, L. (2018). Per- and polyfluoroalkyl substances (pfass) in water, soil and plants in wetlands and agricultural areas in kampala, uganda. *Science of The Total Environment*, *631-632*, 660–667. https://doi.org/https://doi.org/10.1016/j.scitotenv.2018.03.024

Defence. (2017, December). *Environmental investigation and environmental site assessment report*. Army Aviation Centre Oakey document archive. Department of Defence, Australian Government. Retrieved May 27, 2025, from https://www.defence.gov.au/sites/default/files/2025-02/SwartzBarracksDocumentArchive.pdf

Defence. (2019, July). *Community walk-in session pfas investigation and management program. acknowledgment of country*. Army Aviation Centre Oakey document archive. Department of Defence, Australian

Government. Retrieved May 27, 2025, from https://web.archive.org.au/awa/20230427190307mp_/https://defence.gov.au/Environment/PFAS/docs/Oakey/Presentations/201907.AACO.Presentation.PMAP.pdf

Desa, S., & Scott, B. (2018). Inferring soil water characteristics for adelaide clay using fractal theory. *Australian Geomechanics Journal*, *53*, 127–135.

European Parliament and Council. (2020, December). *Directive (eu) 2020/2184 of the european parliament and of the council of 16 december 2020 on the quality of water intended for human consumption (recast) (text with eea relevance)* [Official Journal of the European Union, L 435, 23.12.2020, p. 1-62]. European Union. Retrieved July 24, 2025, from http://data.europa.eu/eli/dir/2020/2184/oj

Fabregat-Palau, J., Zweigle, J., Renner, D., Zwiener, C., & Grathwohl, P. (2025). Assessment of pfas contamination in agricultural soils: Non-target identification of precursors, fluorine mass balance and microcosm studies. *Journal of Hazardous Materials*, *490*, 137798. https://doi.org/https://doi.org/10.1016/j.jhazmat.2025.137798

Giesy, J. P., & Kannan, K. (2001). Global distribution of perfluorooctane sulfonate in wildlife. *Environmental Science & Technology*, *35*(7), 1339–1342. https://doi.org/10.1021/es001834k

Glüge, J., Scheringer, M., Cousins, I. T., DeWitt, J. C., Goldenman, G., Herzke, D., Lohmann, R., Ng, C. A., Trier, X., & Wang, Z. (2020). An overview of the uses of per- and polyfluoroalkyl substances (pfas). *Environ. Sci.: Processes Impacts*, *22*, 2345–2373. https://doi.org/10.1039/D0EM00291G

Guo, B., Zeng, J., & Brusseau, M. L. (2020). A mathematical model for the release, transport, and retention of per- and polyfluoroalkyl substances (pfas) in the vadose zone. *Water Resources Research*, *56*(2), e2019WR026667. https://doi.org/https://doi.org/10.1029/2019WR026667

Hansen, K. J., Clemen, L. A., Ellefson, M. E., & Johnson, H. O. (2001). Compound-specific, quantitative characterization of organic fluorochemicals in biological matrices. *Environmental Science & Technology*, *35*(4), 766–770. https://doi.org/10.1021/es001489z

Hatton, J., Holton, C., & DiGuiseppi, B. (2018). Occurrence and behavior of per- and polyfluoroalkyl substances from aqueous film-forming foam in groundwater systems. *Remediation Journal*, *28*(2), 89–99. https://doi.org/https://doi.org/10.1002/rem.21552

Heads of EPA Australia and New Zealand (HEPA). (2025). PFAS National Environmental Management Plan, Version 3.0. *Australian Government - Department of Climate Change, Energy, the EnvironmentWater*. Retrieved July 24, 2025, from https://www.dcceew.gov.au/environment/protection/publications/pfas-nemp-3

Hellsing, M. S., Josefsson, S., Hughes, A. V., & Ahrens, L. (2016). Sorption of perfluoroalkyl substances to two types of minerals. *Chemosphere*, *159*, 385–391. https://doi.org/https://doi.org/10.1016/j.chemosphere.2016.06.016

Higgins, C. P., & Luthy, R. G. (2006). Sorption of perfluorinated surfactants on sediments. *Environmental Science & Technology*, *40*(23), 7251–7256. https://doi.org/10.1021/es061000n

Hutson, J. (2003, March). *Leachm (leaching estimation and chemistry model): A process-based model of water and solute movement, transformations, plant uptake and chemical reactions in the unsaturated zone. version 4* [Research Series No. R03-1, Department of Crop and Soil Sciences, Cornell University, Ithaca, New York].

Institut national de l'environnement industriel et des risques (INERIS). (2024, January). *Comportement des substances per- et polyfluoroalkylées (pfas) dans les sols et les eaux souterraines - synthèse bibliographique* [Verneuil-en-Halatte : Ineris, 213870_2789035-v1.0, 30/01/2024]. Ineris. Retrieved August 2, 2025, from https://www.ineris.fr/fr/comportement-substances-polyfluoroalkylees-pfas-sols-eaux-souterraines-synthese-bibliographique

Interstate Technology & Regulatory Council (ITRC). (2023). *Pfas technical and regulatory guidance document and fact sheets pfas-1*. Washington, D.C.: Interstate Technology & Regulatory Council, PFAS Team. Retrieved May 26, 2025, from https://pfas-1.itrcweb.org/

Jambhekar, V., Helmig, R., Schröder, N., & Shokri, N. (2015). Free-flow-porous-media coupling for evaporation-driven transport and precipitation of salt in soil. *Transport in Porous Media*, *110*, 251–280. https://doi.org/10.1007/s11242-015-0516-7

Li, H., Dong, Q., Zhang, M., Gong, T., Zan, R., & Wang, W. (2023). Transport behavior difference and transport model of long- and short-chain per- and polyfluoroalkyl substances in underground environmental media: A review. *Environmental Pollution*, *327*, 121579. https://doi.org/https://doi.org/10.1016/j.envpol.2023.121579

Li, Y., Oliver, D. P., & Kookana, R. S. (2018). A critical analysis of published data to discern the role of soil and sediment properties in determining sorption of per and polyfluoroalkyl substances (pfass). *Science of The Total Environment*, *628-629*, 110–120. https://doi.org/https://doi.org/10.1016/j.scitotenv.2018.01.167

Li, Y., Fletcher, T., Mucs, D., Scott, K., Lindh, C. H., Tallving, P., & Jakobsson, K. (2018). Half-lives of pfos, pfhxs and pfoa after end of exposure to contaminated drinking water. *Occupational and Environmental Medicine*, *75*(1), 46–51. https://doi.org/10.1136/oemed-2017-104651

Li, Y., Niu, Z., & Zhang, Y. (2022). Occurrence of legacy and emerging poly- and perfluoroalkyl substances in water: A case study in tianjin (china). *Chemosphere*, *287*, 132409. https://doi.org/https://doi.org/10.1016/j.chemosphere.2021.132409

Lyu, X., Xiao, F., Shen, C., Chen, J., Park, C. M., Sun, Y., Flury, M., & Wang, D. (2022). Per- and polyfluoroalkyl substances (pfas) in subsurface environments: Occurrence, fate, transport, and research prospect. *Reviews of Geophysics*, *60*(3), e2021RG000765. https://doi.org/https://doi.org/10.1029/2021RG000765

Milinovic, J., Lacorte, S., Vidal, M., & Rigol, A. (2015). Sorption behaviour of perfluoroalkyl substances in soils. *Science of the Total Environment*, *511*, 63–71. https://doi.org/10.1016/j.scitotenv.2014.12.017

Newell, C., & Connor, J. (1998). Characteristics of dissolved petroleum hydrocarbon plumes, results from four studies. *American Petroleum Institute*. Retrieved May 27, 2025, from https://www.api.org/~/media/files/ehs/clean_water/bulletins/08_bull.pdf

Nguyen, T. M. H., Bräunig, J., Thompson, K., Thompson, J., Kabiri, S., Navarro, D. A., Kookana, R. S., Grimison, C., Barnes, C. M., Higgins, C. P., McLaughlin, M. J., & Mueller, J. F. (2020). Influences of chemical properties, soil properties, and solution ph on soil-water partitioning coefficients of per- and polyfluoroalkyl substances (pfass). *Environmental Science & Technology*, *54*(24), 15883–15892. https://doi.org/10.1021/acs.est.0c05705

OECD. (2021). *Reconciling terminology of the universe of per- and polyfluoroalkyl substances: Recommendations and practical guidance* [OECD Series on Risk Management, 61]. OECD Publishing. Retrieved May 26, 2025, from https://www.oecd.org/chemicalsafety/risk-management/reconciling-terminology-of-the-universe-of-per-and-polyfluoroalkyl-substances.pdf

Pittaki-Chrysodonta, Z., Moldrup, P., Knadel, M., Iversen, B. V., Hermansen, C., Greve, M. H., & de Jonge, L. W. (2018). Predicting the campbell soil water retention function: Comparing visible-near-infrared spectroscopy with classical pedotransfer function. *Vadose Zone Journal*, *17*(1), 170169. https://doi.org/https://doi.org/10.2136/vzj2017.09.0169

Queensland Government - Long Paddock. (2024, August). *Silo - australian climate data from 1889 to yesterday*. Queensland Government, Climate Projections and Services (Treasury). Retrieved June 10, 2025, from https://www.longpaddock.qld.gov.au/silo

Rasmusson, K., & Fagerlund, F. (2024). Per- and polyfluoroalkyl substances (pfas) as contaminants in groundwater resources - a comprehensive review of subsurface transport processes. *Chemosphere*, *362*, 142663. https://doi.org/https://doi.org/10.1016/j.chemosphere.2024.142663

Royal Meteorological Institute of Belgium (RMI). (2025, October). *Gridded observational data — rmi geonetwork catalogue* [Dataset provides gridded observational meteorological data (5 km spatial resolution) across Belgium since 1961; last revised 2024-10-01]. Royal Meteorological Institute of Belgium. Retrieved July 4, 2025, from https://opendata.meteo.be/download

Sauleda, M. L., Hsieh, T.-L., Xu, W., Tilton, R. D., & Garoff, S. (2022). Surfactant spreading on a deep subphase: Coupling of marangoni flow and capillary waves. *Journal of Colloid and Interface Science*, *614*, 511–521. https://doi.org/https://doi.org/10.1016/j.jcis.2022.01.142

Silva, J. A., Martin, W. A., Johnson, J. L., & McCray, J. E. (2019). Evaluating air-water and napl-water interfacial adsorption and retention of perfluorocarboxylic acids within the vadose zone. *Journal of Contaminant Hydrology*, *223*, 103472. https://doi.org/https://doi.org/10.1016/j.jconhyd.2019.03.004

SPW ARNE. (2025, February). *Lignes directrices pour les PFAS pour les études décret sols* (tech. rep.) (Version 2.0, Daté du 25 février 2025). Service Public de Wallonie (SPW), Agriculture, Ressources naturelles et Environnement(ARNE)). Retrieved July 24, 2025, from https://environnement.wallonie.be

USEPA. (2015). *Risk-screening environmental indicators (rsei) model version 2.3.4. technical appendix b physicochemical properties for tri chemicals and chemical categories*. USEPA. Retrieved May 26, 2025, from https://www.epa.gov/rsei/risk-screening-environmental-indicators-rsei-model-reference-document-history

USEPA. (2022, August). *Pfas|epa: Pfas structures in dsstoxs (version 5) - pfasstructv5* [CompTox Chemicals Dashboard. Last updated August 2022]. USEPA. Retrieved June 10, 2025, from https://comptox.epa.gov/dashboard/chemical-lists/PFASSTRUCTV5

Wallis, I., Hutson, J., Davis, G., Kookana, R., Rayner, J., & Prommer, H. (2022). Model-based identification of vadose zone controls on pfas mobility under semi-arid climate conditions. *Water Research*, *225*, 119096. https://doi.org/10.1016/j.watres.2022.119096

We, A. C. E., Zamyadi, A., Stickland, A., Clarke, B., & Freguia, S. (2023). A review of foam fractionation for the removal of per- and polyfluoroalkyl substances (pfas) from aqueous matrices. *Journal of Hazardous Materials*, *465*, 133182. https://doi.org/10.1016/j.jhazmat.2023.133182

Xiong, Y. (2014). Flow of water in porous media with saturation overshoot: A review. *Journal of Hydrology*, *510*, 353–362. https://doi.org/https://doi.org/10.1016/j.jhydrol.2013.12.043